SUBSURFACE THERMAL COAGULATION OF TISSUES USING NEAR INFRARED LASERS

by

Chun-Hung Jack Chang

A dissertation submitted to the faculty of
The University of North Carolina at Charlotte
in partial fulfillment of the requirements
for the degree of Doctor of Philosophy in
Optical Science and Engineering

Charlotte

2017

Approved by:

_____
Dr. Nathaniel M. Fried

_____
Dr. Yuri E. Nesmelov

_____
Dr. Irina V. Nesmelova

_____
Dr. Shunji Egusa

_____
Dr. Mark G. Clemens

ABSTRACT

CHUN-HUNG JACK CHANG. Subsurface thermal coagulation of tissues using near infrared lasers. (Under the direction of DR. NATHANIEL M. FRIED)

Noninvasive laser therapy is currently limited primarily to cosmetic dermatological applications such as skin resurfacing, hair removal, tattoo removal and treatment of vascular birthmarks. In order to expand applications of noninvasive laser therapy, deeper optical penetration of laser radiation in tissue as well as more aggressive cooling of the tissue surface is necessary. The near-infrared laser wavelength of 1075 nm was found to be the optimal laser wavelength for creation of deep subsurface thermal lesions in liver tissue, *ex vivo,* with contact cooling, preserving a surface tissue layer of ~ 2 mm. Monte Carlo light transport, heat transfer, and Arrhenius integral thermal damage simulations were conducted at this wavelength, showing good agreement between experiment and simulations. Building on the initial results, our goal is to develop new noninvasive laser therapies for application in urology, specifically for treatment of female stress urinary incontinence (SUI). Various laser balloon probes including side-firing and diffusing fibers were designed and tested for both transvaginal and transurethral approaches to treatment. The transvaginal approach showed the highest feasibility. To further increase optical penetration depth, various types and concentrations of optical clearing agents were also explored. Three cadavers studies were performed to investigate and demonstrate the feasibility of laser treatment for SUI.

DEDICATION

This body of work is dedicated…

To my loving parents, whose words of encouragement and push for tenacity ring in my ears.

To Dr. Nathaniel Fried for his unwavering support and encouragement over the years.

To my Brother, my confidant,
who encouraged me to pursue my dreams wherever they may take me.

To all my friends who believed in me

It is through you all that I truly stand on the shoulders of giants.

"Meliora"

ACKNOWLEDGMENTS

I would like to thank Dr. Nathaniel Fried, my advisor, for his continued support and guidance throughout my research and academic studies. I appreciate the support of a Research Assistantship founded by National Institutes of Health, Award #1R15DK099774. I also appreciate the Graduate Assistant Support Plan (GASP) for tuition provided by the graduate school at UNC Charlotte and the travel funding provided by the Center for Biomedical Engineering and Science.

I would like to thank all of my fellow Biomedical Optics Laboratory members and members of other laboratories who have provided insight and assistance throughout my graduate career including, Luke Hardy, Tom Hutchens, Christopher Wilson, Joshua Kennedy, Yuanye Liu and Jonathan Babaie.

TABLE OF CONTENTS

LIST OF FIGURES

LIST OF TABLES

LIST OF ABBREVIATIONS

α	absorption coefficient
~	approximately
≈	approximately equal to
°C	degrees Celsius
Δ	change
dia	diameter
DOF	depth of field
ex vivo	Latin: (out of the living)
FC	fiber connector
FLIR	forward-looking infrared
FOV	field of view
Fr	French (1 mm = 3 Fr)
g	gram
in vitro	Latin: (within glass)
in vivo	Latin: (within the living)
ID	inner diameter
IR	infrared
J	joule
λ	wavelength
μ-	micro- (10^{-6})
m	meter
m-	milli- (10^{-3})

min	minute
N	number
n	index of refraction
n-	nano- (10^{-9})
NA	numerical aperture
OD	outer diameter
OPD	optical penetration depth
s *or* sec	second
SD	standard deviation
θ_i	incident angle
θ_r	refracted angle
3D	three dimensional
UV	ultraviolet
W	watt

CHAPTER 1: INTRODUCTION

Noninvasive laser therapy is currently limited primarily to cosmetic dermatological applications such as skin resurfacing, hair removal, tattoo removal and treatment of vascular birthmarks. Preservation of the surface tissue in these applications is superficial (skin layer of 200-400 micrometers [1]). The ability to preserve the tissue surface to a depth on the order of a few millimeters by more aggressive cooling of the tissue surface in combination with deeper laser heating of subsurface tissue structures may result in development of new noninvasive laser applications beyond the field of cosmetic surgery.

Previously, our laboratory demonstrated creation of deep subsurface thermal lesions in a variety of tissues using both non-contact and contact cooling techniques [2, 3] and also developed a noninvasive laser method of male sterilization [4]; building on this success, our next goal is to develop new noninvasive laser therapies for application in urology, specifically for treatment of female stress urinary incontinence (SUI). This study will not only test the feasibility of noninvasive laser treatment for female stress urinary incontinence but also open the possibility of thermal tissue remodeling for other medical applications as well.

In Chapter 2, the theory of laser tissue interactions will be defined in terms of the effects of wavelength and laser spot size on optical penetration depth in tissues. A brief description of various types of laser tissue interaction will be discussed.

In Chapter 3, laser wavelength comparison studies were performed. Porcine liver tissue was used to compare and find the optimal wavelength that provides the deepest optical penetration depth for non-invasive treatment. Surface tissue was not preserved at the 650 nm wavelength, and preserved tissue layers for the 808 and 980 nm wavelengths were superficial. Only the 1075 nm wavelength preserved a thick tissue surface layer of ~ 2 mm.

In Chapter 4, Monte Carlo methods were employed for photon transport in tissue, heat transfer models used, and an Arrhenius integral thermal damage model applied to calculate thermal damage. Those simulation parameters were based on data from previous publications. The near-infrared laser wavelength of 1075 nm provided deep subsurface thermal lesions in liver tissue while preserving up to 2 mm of the tissue surface from thermal damage, for potential noninvasive laser applications.

In Chapter 5, miniaturization of the laser probe was explored by modifying a standard dual balloon catheter. Transvaginal probe and transurethral probe methods were compared. Various delivery methods were tested during the probe development including side firing, diffusing, and radial firing. In summary, the radial delivery probe failed to produce thermal lesions due to limited optical penetration depth. The side-firing laser probe preserved 0.5 ± 0.1 mm tissue from thermal coagulation, while the diffusing laser probe preserved 0.8 ± 0.1 mm tissue from thermal coagulation. While these methods produced subsurface thermal lesions in tissue, higher cooling rates and less divergent laser beams are needed for deeper penetration and greater tissue surface preservation.

In Chapter 6, the specific application of noninvasive laser therapy for treating female stress urinary incontinence was explored and simulated. Female stress urinary

incontinence clinical background information was discussed in detail. Previous simulation results from chapter 4 and experimental data from chapter 3 and chapter 5 were compared. Computer simulations utilizing a transvaginal approach predicted that the majority of vaginal wall could be preserved from thermal damage, due to a combination of deeper light penetration and applied cooling of the vaginal wall. However, the transurethral probe simulations showed a high percentage of the urethral wall exposed to excessive temperatures producing irreversible thermal damage and tissue necrosis. It was concluded that laser SUI treatment should be performed with a transvaginal approach.

In Chapter 7, optical clearing agents were studied to further improve treatment depth of noninvasive laser therapies. Various OCA is were compared at 37 °C at 1075nm and the most effective OCA for porcine vaginal tissue was identified. Optical coherence tomography at 1300 nm was also used to study the change in transmission, with similar results as 1075 nm. Finally, the simulation technique from chapter 4 was applied along with the experimental data collected from OCA. The simulations demonstrated that use of an OCA may further improve treatment depth for thermal remodeling by approximately 0.5 mm. This should allow preservation of the entire (2.7-mm-thick) vaginal wall during subsurface laser targeting and thermal remodeling of the endopelvic fascia for minimally invasive treatment of female stress urinary incontinence.

In Chapter 8, three human cadaver studies were performed. The treatment zone and laser probe dimension for SUI treatment were investigated. Based on anatomical limitations, a 2.2 x 1.9 x 3.5 cm miniaturized 2nd generation laser contact cooling probe was designed and constructed, resulting in only 4% power lost and 2 °C colder probe. The effectiveness of glycerol as an OCA was tested and optimal treatment time was determined

to be 10 minutes. Subsurface lesions were made using a 1075 nm laser and preserved surface tissue measured 0.77 ± 0.09 to 1.1± 0.17 mm with 6.4 W and 4.6 W, respectively, for 30 seconds. The results demonstrated the feasibility of laser treatment for SUI and a solid foundation for future *in vivo* animal studies.

In Chapter 9, the main findings will be summarized.

PROJECT TREE

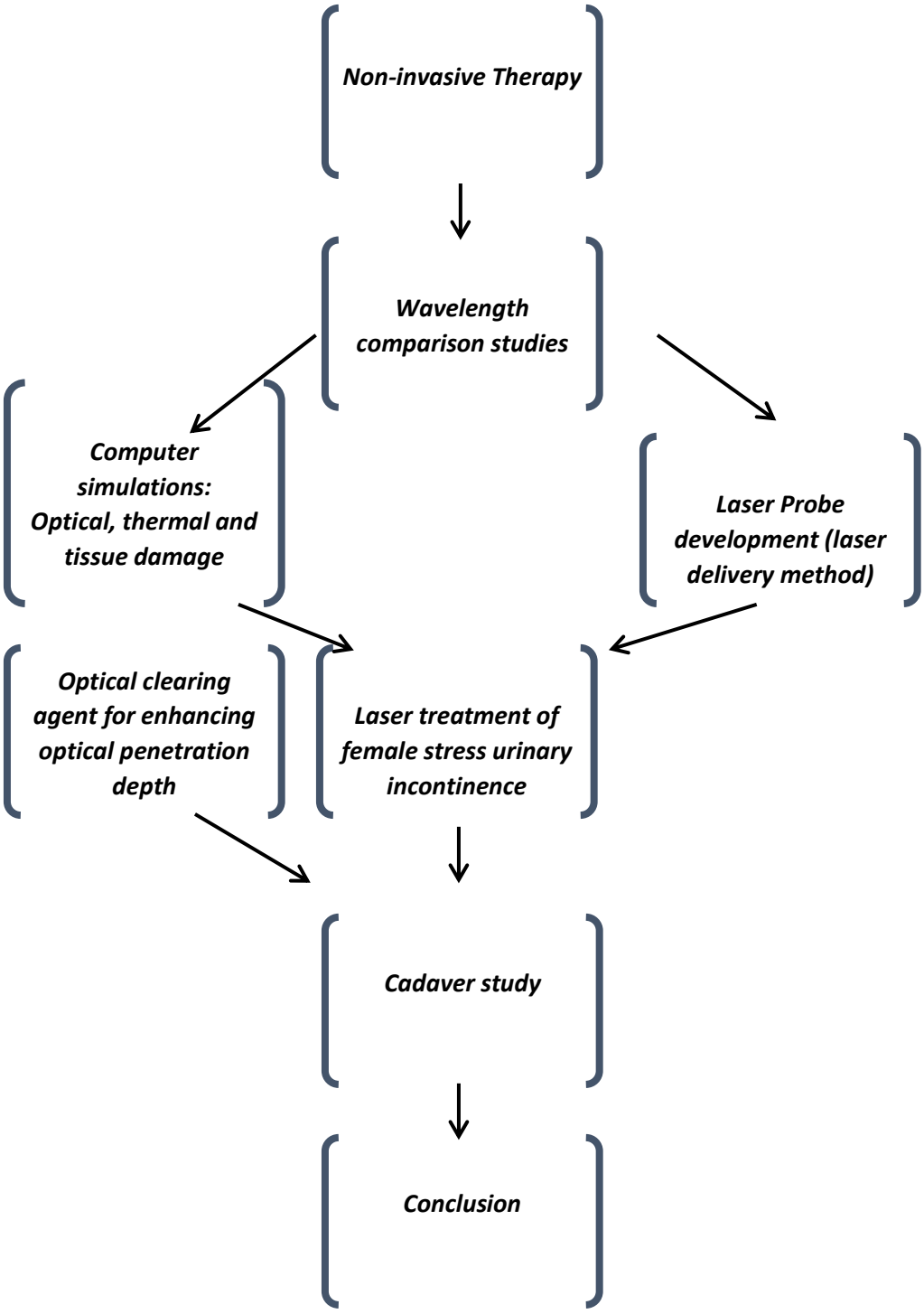

CHAPTER 2: Theory: Laser Tissue Interactions

2.1 Effect of laser wavelength and tissue optical properties on optical penetration depth

Optical Penetration Depth, δ, is defined for a collimated beam entering tissue with a reduction to 36.7% (1/e) of incident light intensity or $\delta=\frac{1}{u_{eff}}$, where u_{eff} is the effective attenuation coefficient. Biological tissues have a refractive index of ~ 1.34, similar to water at 1.33. When light is incident from air, Fresnel reflectance is approximately 2%. Therefore, most light entering the tissue is either absorbed or scattered (Figure 2.1). The absorption coefficient, u_a, determines the rate of absorption over distance; similarly the scattering coefficient, u_s, describes how light is scattered over distance. Together those two coefficients form the total attenuation coefficient, u_t, in a modified Beer's law (Eq.1), where T_c is the collimated & unscattered transmittance (I/I_0) and t is the tissue thickness. For non-scattering tissue, where $u_a \gg u_s$, it is sufficient to describe attenuation using the modified Beer's law (Eq.1.)

Eq.1 $$T_c = e^{-u_t t}$$

Eq.2 $$u_t = u_a + u_s$$

However, in the near-infrared spectrum, most biological tissues are highly scattering $u_s \gg u_a$. Beer's law is not sufficient to describe attenuation in such cases. Hence, more elaborate photon transport equations are employed to accurately describe scattering. Scattering Anisotropy, g, describes the directionality of the scattering, which can be

summarized by Henyey-Greenstein functions, where p (cos θ) is the scattering phase function (Eq.3) [5].

Eq.3
$$p(\cos\theta) = \frac{1 - g^2}{2(1 + g^2 - 2g\cos\theta)^{3/2}}$$

Once directionality has been taken into consideration, the reduced scattering coefficient, u_s', can then be represented from the relationship between the scattering coefficient, u_s and the anisotropy, g, in Eq.4.

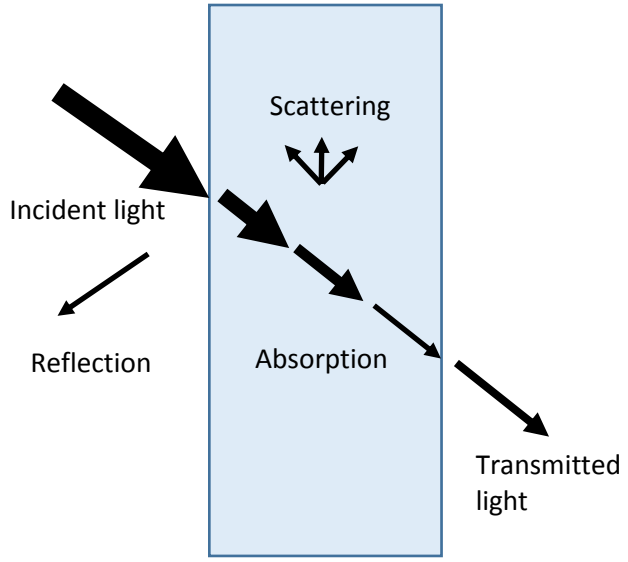

Figure 2.1. Geometry of reflection, refraction, absorption and scattering [6].

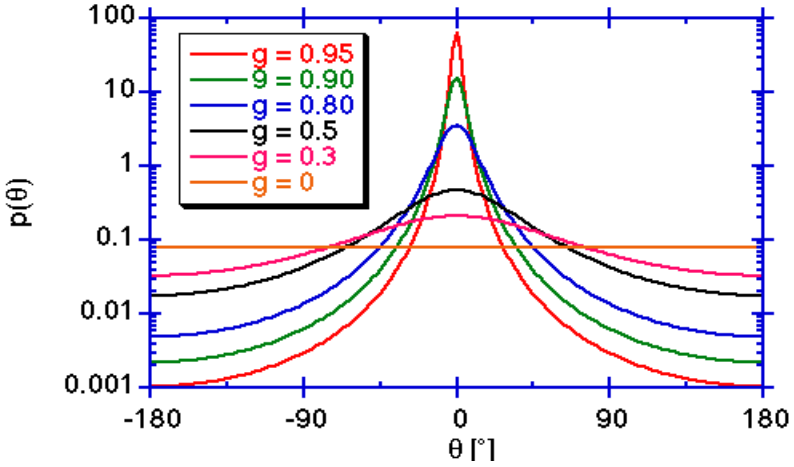

Figure 2.2. A series of Henyey-Greenstein functions, where forward scattering is 0° and backward scattering is 180° [5].

Eq.4	$u_s' = u_s(1-g)$	Reduced scattering coefficient (cm^{-1})
Eq.5	$u_t{}' = u_a + u_s{}'$	Transport interaction coefficient (cm^{-1})
Eq.6	$u_{eff} = \sqrt{3u_a u_t{}'}$	Effective attenuation coefficient (cm^{-1})
Eq.7	$\delta = \frac{1}{u_{eff}} = \frac{1}{\sqrt{3u_a(u_a + u_s(1-\mathrm{g}))}}$	Optical penetration depth (cm)

After the reduced scattering coefficient, u_s', is defined, it becomes clear that the transport interaction coefficient, $u_t{}'$, in Eq. 5 is similar to but modified from u_t, the total attenuation coefficient, from Beer's law in Eq. 2. In Eq. 6, the effective attenuation coefficient, u_{eff}, is defined. Finally, using Eq. 4 to Eq. 6, the definition of optical penetration depth reduces to a simple relationship incorporating absorption coefficient, scattering coefficient, and anisotropy in Eq. 7.

These coefficients vary across the electromagnetic spectrum depending on various tissue components such as the concentration of water, hemoglobin, and other tissue proteins. Typically, red and near infrared wavelengths penetrate most deeply, and span a "therapeutic window" from 600-1300 nm because of the lower scattering and absorption coefficients in this region (Figure 2.3). For example, in Figure 2.4, skin tissue displays a deep optical penetration depth in the region of the therapeutic window (near infrared) where both scattering and absorption tend to be lower in biological tissues.

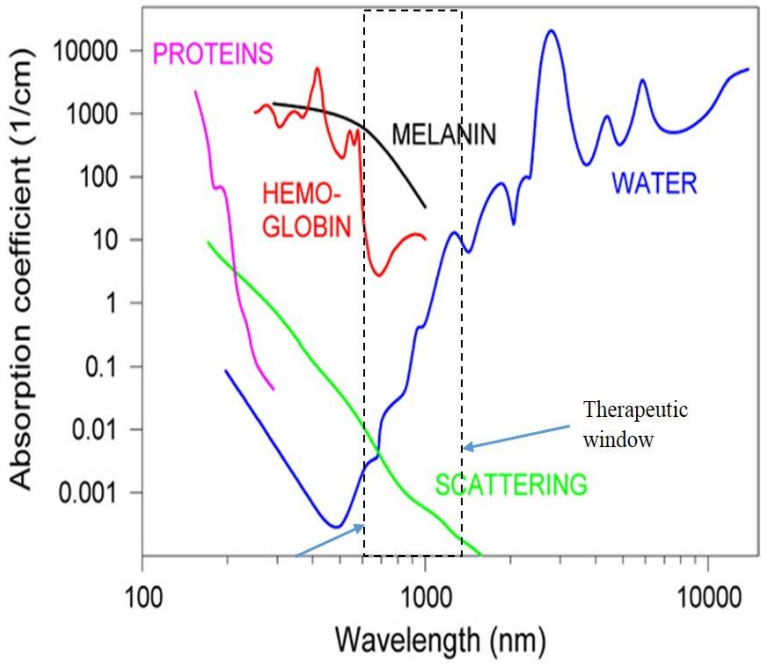

Figure 2.3. Absorption curves for protein, collagen, hemoglobin, melanin, and water. Therapeutic window is provided by dashed boundaries [7].

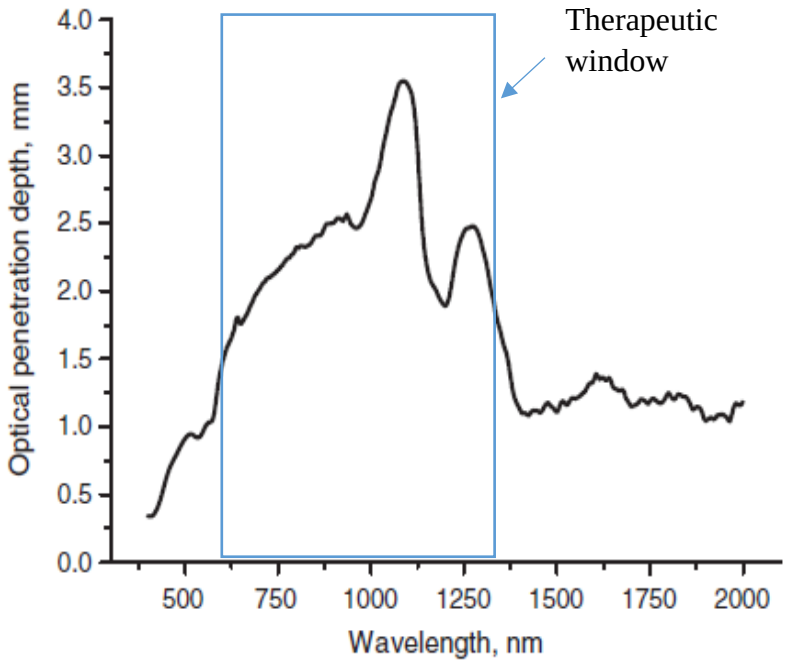

Figure 2.4. Optical penetration depth in skin [7]. Therapeutic window is provided by box.

2.2. Effect of laser spot size on optical penetration depth.

Optical penetration depth is primarily dependent on the optical properties of the tissue for a given laser wavelength. However, for highly scattering tissues, the laser spot size also plays an important role. The distribution of laser radiation in tissue can be more deeply and uniformly deposited by using a larger diameter laser spot (Figure 2.5). A larger laser beam diameter provides a smaller surface area to volume ratio, so that losses in beam intensity due to scattering at the beam's peripheral edges are reduced.

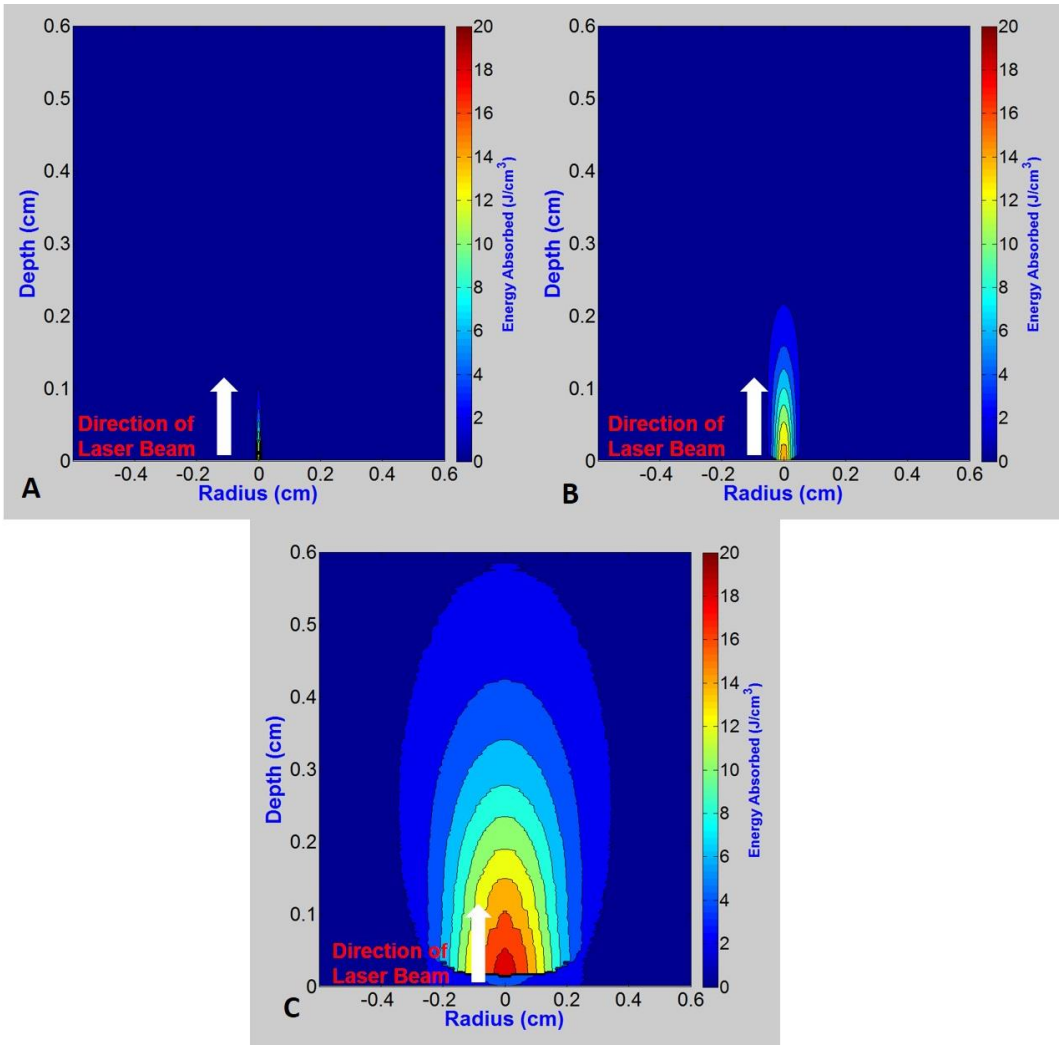

Figure 2.5. Distribution of photons using Monte Carlo simulations for 1075 nm laser beam with different diameters, but with the same power density of 36.7 W/cm^2. (a) 200 µm; (b) 1 mm; (c) 5 mm; The radiation penetrates deeper as laser beam diameter increases.

The above simulation is based on a Monte Carlo model, which will be further discussed in a later chapter. The simulation shows near-infrared, 1075 nm laser radiation interacting with liver tissue with the same power density of 36.7 W/cm^2 used throughout each sample, and only the laser beam diameter varied from 0.2, 1, and 5 mm. The simulation demostrates that the larger the beam diameter, the deeper the photons penetrate. For example, the photons of the 5 mm diameter beam propagate signifcally deeper in comparison with the 0.2 mm diameter laser beam. The simulations are conducted with the same power density and the values used in this simulation are provided in Table 4.1. This result also agrees with previous reports by Welch et al [9]. They used a 476 nm laser wavelength and a different tissue type, also demonstrating that a larger laser beam diameter provides a deeper optical penetration depth in highly scattering tissue.

2.3. Effect of laser power and time on tissue interaction.

A double-logarithmic map (Figure 2.6) displays five types of laser tissue interaction mechanisms based on a combination of time and power density. Laser therapies can be classified under these five different categories: photochemical, photothermal, photoablation, plasma induced ablation, and photodisruption. A photochemical interaction typically uses low laser power and long exposure time to trigger a chemical reaction by stimulating the chemical to an excited state. As example of a photochemical interaction is photodynamic therapy (PDT). During PDT, a specific chromophore is injected into the body and then selectively accumulates in a tumor and the treatment is triggered by absorption of light selective, localized, photochemical reaction.

A photothermal interaction requires higher power density than a photochemical interaction. A thermal interaction converts light absorption into heat in tissue, which may result in coagulation, vaporization, carbonization, and melting. Depending on the power and the duration of laser irradiation, tissues react differently to each setting. In general, around ~ 60 °C tissue and collagen denaturation start to occur that leads to coagulation; above 100 °C vaporization, and thermal decomposition occurs; and at higher temperatures, carbonization and melting may occur [10]. The studies described in this dissertation were all performed under thermal interaction mechanism at coagulation temperatures.

Photoablation is a direct breaking of cellular structure. It normally occurs when high energy UV radiation creates precise removal of tissue. For example, during LASIK surgery the precise removal of corneal tissue using an ArF excimer laser pulse is considered a photoablation mechanism.

The photodisruption mechanism is based on shockwave generation at high pulse intensity which causes fragmentation and cutting of the tissue by the mechanical force of a shockwave.

Plasma-induced ablation is induced by high-intensity short pulses leading to dielectric breakdown that creates ionized plasma which interacts with light to produce ablation.

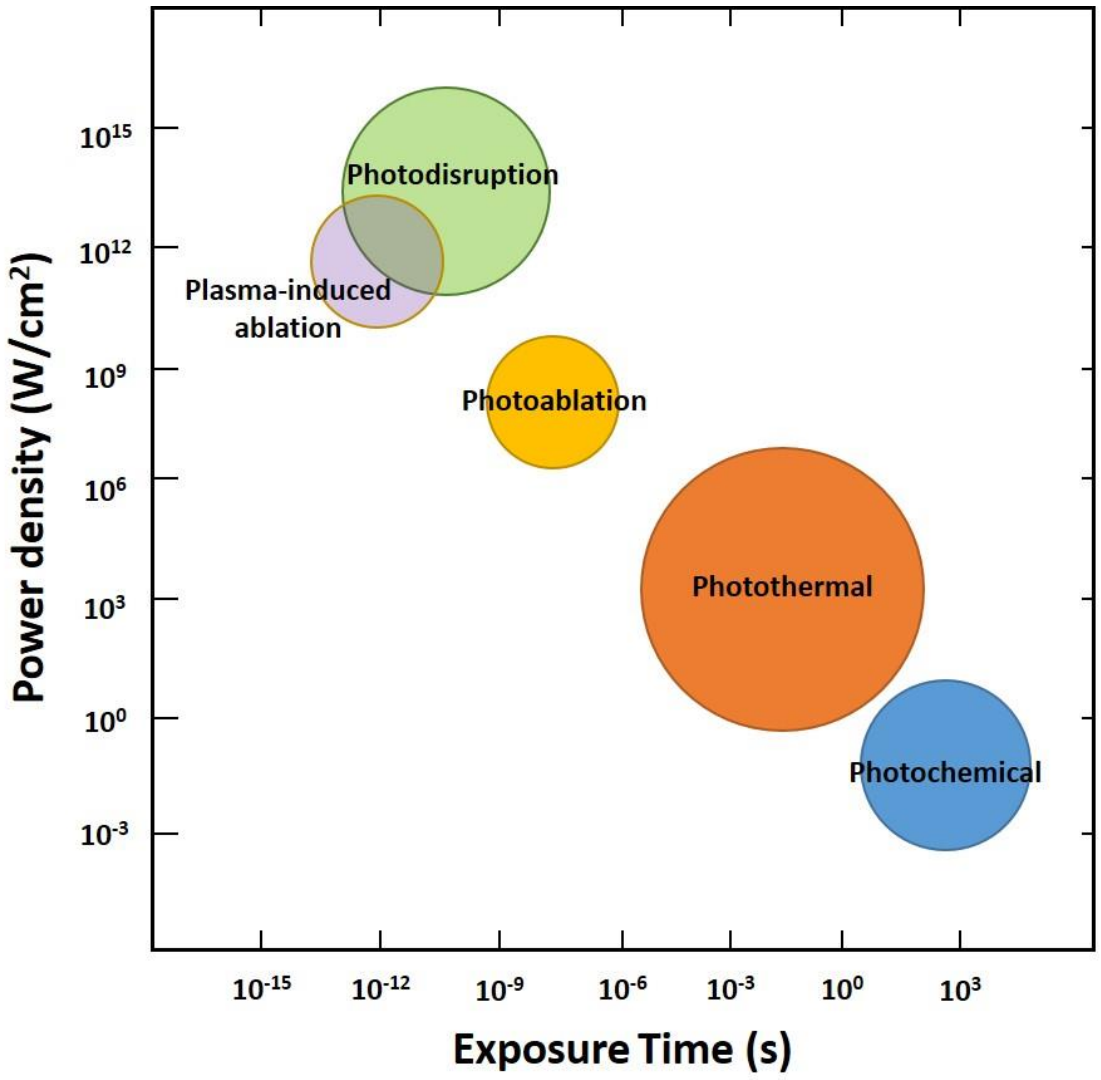

Figure 2.6 A double-logarithmic map displays five types of laser tissue interaction mechanisms based on a combination of time and power density.

CHAPTER 3: Comparison of Laser Wavelengths for Subsurface Thermal Tissue Coagulation

3.1 Introduction

The objective of this *ex vivo* tissue study was to identify the optimal laser wavelength for subsurface thermal tissue coagulation and remodeling. A contact cooling system was applied to preserve the tissue surface during creation of subsurface thermal lesions. Four lasers spanning the optical window in the visible to near IR spectrum (600-1300 nm) were explored.

3.2 Materials and Methods

3.2.1 Tissue Preparation

Porcine liver tissue was used as a model for the wavelength comparison study because it could easily be quantified by analyzing the gross appearance of thermal lesions. The liver tissue samples were obtained from a slaughterhouse (Animal Technologies, Tyler, TX). Upon arrival, the livers were frozen and stored separately. Before experimentation, the sealed liver tissue was thawed in cold water. Livers were cut into cylindrical samples by a stainless-steel cutting mold measuring 54 mm in diameter and 20 mm in height; and samples were then kept hydrated in a sealed container to avoid dehydration [10]. The tissue was then warmed up to about 34 °C in warm water over 30 minutes.

3.2.2 Probe Design and Cooling Systems

The laser probe was a custom made, endoscopic, side-firing probe designed by the Biomedical Optics Laboratory and built by the Center for Precision Metrology at UNC-Charlotte. The probe consisted of a gold coated rod mirror for side-firing delivery, and a sapphire window in contact with the flow cell for contact cooling of the tissue. The cooling element of the laser probe consisted of a recirculating chiller (T255P-D5, Thermotek, Carrollton, TX). A coolant (25% ethylene alcohol / 75% water by volume) flowed at a rate of the 12.7 ml/sec through flow cell and allowed the chiller to operate at a temperature of – 5 °C. The custom-built flow cell consisted of aluminum housing with a sapphire plate mounted at the surface. Coolant flowed through a circular channel around the circumference of the flow cell, while an 8-mm-diameter aperture in the center of the flow cell provided a window for transmission of laser energy through the transparent sapphire plate. The sapphire plate temperature measured -2 °C, and provided a thermally conductive medium for contact cooling of the tissue surface, as well as an optically transparent window for delivery of the laser energy.

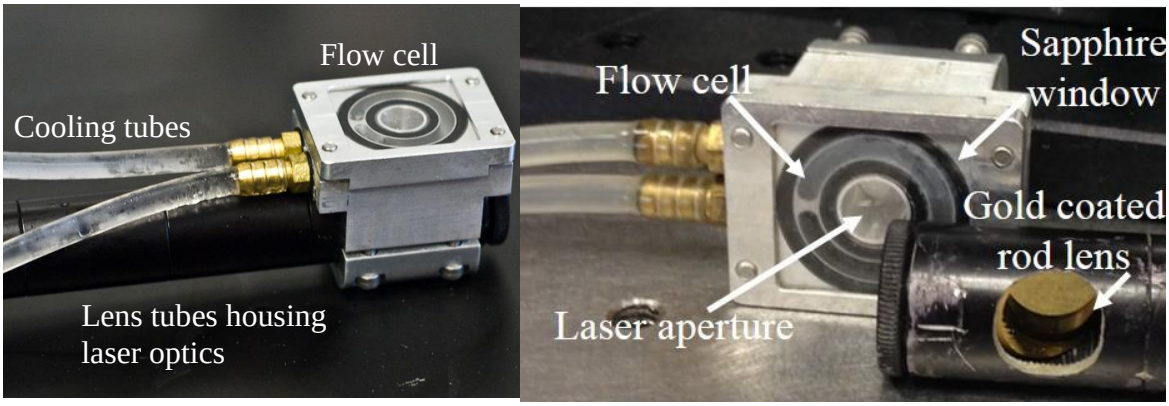

Figure 3.1. Close-up view of laser probe, including flow cell and coolant tubes. An optical fiber (not shown here) connected the laser to the probe.

3.2.3. Laser Parameters

Four lasers were compared in this preliminary study (Figure 3.2), including a 7 W, 650 nm diode laser (Modulight, Finland), 30 W, 808 nm laser (Apollo Instruments, Irvine, CA), 50 W, 980 nm diode laser (Edwards Life Sciences, Irvine, CA), and 50 W Ytterbium fiber laser (IPG Photonics, Oxford, MA). The laser energy was coupled into a custom-made laser probe using a 100-mm-focal-length lens and a 600-µm-core, 0.39 NA optical fiber patch-cord (M29L05, Thorlabs, Newton, NJ). The laser probe was assembled using 12.7-mm inner-diameter lens tubes, housing the optics, including a lens for collimating the laser beam and a mirror for 90° delivery. The comparative wavelength study was limited by the power output through the probe for the 650 nm laser. An incident laser power of 4.2 W and $1/e^2$ spot diameter of 5.25 mm was used (19.0 W/cm^2) for all four lasers. The laser power was calibrated using a power meter (EPM2000, Molectron, Portland, OR) conntected to a detector (PM 150 Coherent, Santa Clara, CA). The Gaussian laser beam was measured using an IR beam analyzer (Pyrocam III, Spiricon, Logan, UT) and by performing a razor blade scan (Figure 3.3).

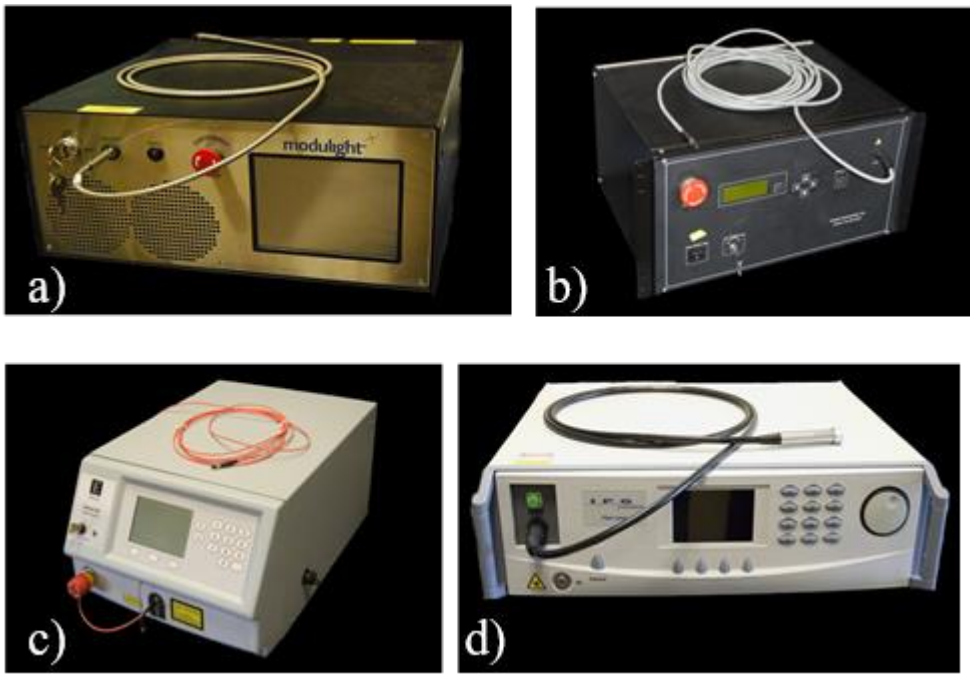

Figure 3.2. Images of the four compact, tabletop lasers used in this study. (a) 650 nm, 7 W diode laser; (b) 808 nm, 30 W diode laser; (c) 980 nm, 50 W diode laser; (d) 1075 nm, 50 W Ytterbium fiber laser.

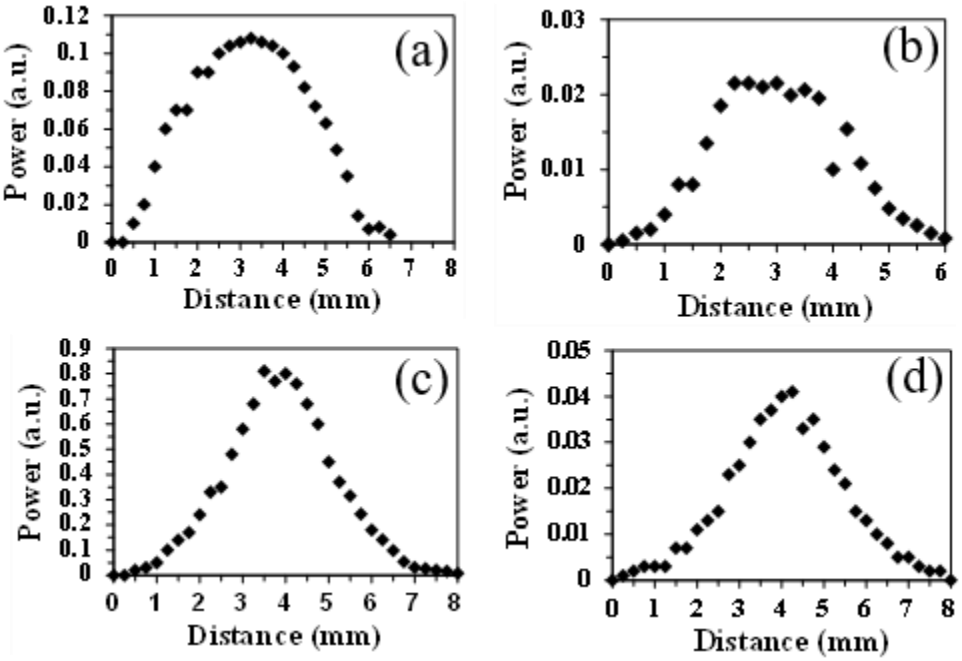

Figure 3.3. Spatial beam profiles for lasers measured using a razor blade scan. (a) 650 nm; (b) 808 nm; (c) 980 nm; (d) 1075 nm. For each laser, spot diameter was 5.2 mm ($1/e^2$).

Once the liver sample was removed from the warm water bath, the tissue was kept warm by using a hot plate with a set temperature of ~ 35°C. The temperature was carefully monitored using an insulated, 125-µm diameter, micro-thermocouple connected to a laptop computer. During the experiment, the laser probe was placed in contact with the liver tissue (Figure 3.4). After laser irradiation, the probe was removed and the lesion area was marked by inserting a pin nearby the lesion area to accurately define the lesion location.

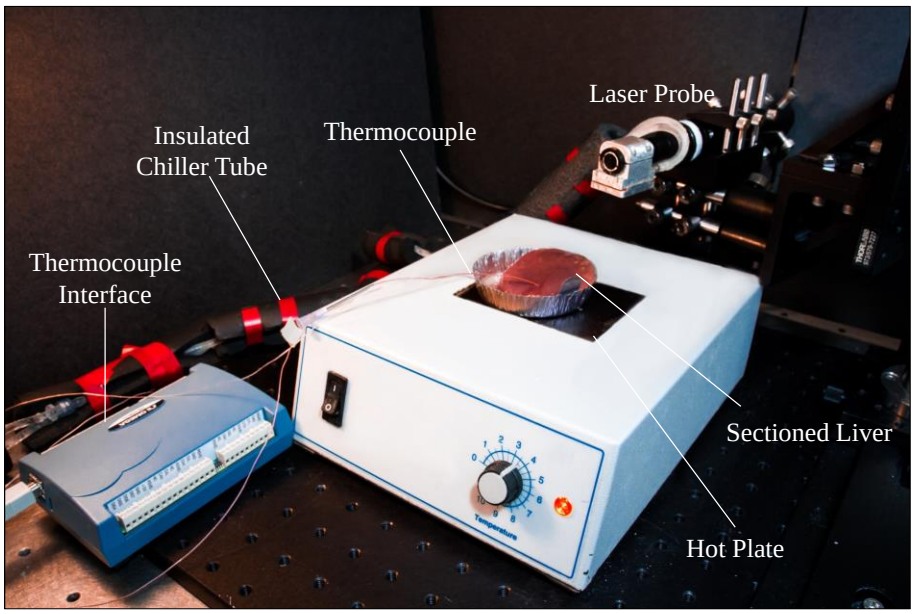

Figure 3.4. Experimental setup showing probe, hot plate, thermocouple system and tissue sample.

3.3. Results

Table 3.1 summarizes the thermal lesion dimensions for the four lasers studied. For the 650 nm wavelength, no surface tissue was preserved, while for the 808 and 980 nm wavelengths only a small tissue layer of ~ 300 µm was preserved. No lesions were observed for the 1075 nm wavelength at 4.2 W, presumably due to the significantly deeper

optical penetration depth at this wavelength. Therefore, a power escalation study was conducted at 1075 nm, until an optimal result of ~ 2 mm of tissue was preserved above the thermal lesion, at an incident laser power of 5.2 W for 60 seconds. Further power escalation studies using 7.2 W for 15 seconds yielded similar results, so shorter procedure times are feasible (Figure 3.5). Power escalation studies performed at the other laser wavelengths resulted in undesirable thermal damage to the tissue surface.

Table 3.1. Comparison of lesion dimensions for the four laser wavelengths tested.

Lesion Characteristics	**650 nm (4.2W/60s)**	**808 nm (4.2W/60s)**	**980 nm (4.2W/60s)**	**1075 nm (5.2W/60s)**	**1075 nm (7.2W/15s)**
Preserved Surface Tissue (mm):	0.0 ± 0.0	0.3 ± 0.2	0.3 ± 0.3	1.9 ± 0.5	1.7 ± 0.5
Lesion Width (mm):	5.3 ± 0.2	3.9 ± 0.6	4.4 ± 0.3	3.0 ± 0.3	2.3 ± 0.4
Lesion Depth (mm):	2.9 ± 0.5	2.3 ± 0.4	3.7 ± 0.6	2.5 ± 0.2	2.3 ± 0.5
Lesion Area (mm^2):	12.2 ± 2.7	7.3 ± 1.9	12.9 ± 2.2	6.0 ± 1.0	4.6 ± 1.8
Sample size (N):	8	6	8	5	6

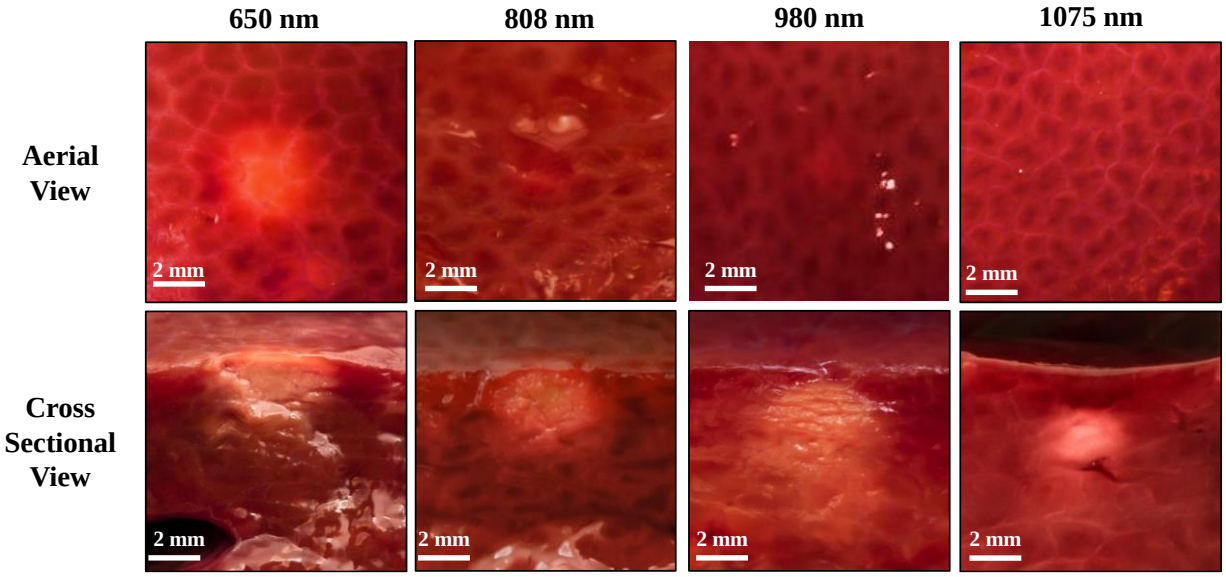

Figure 3.5. Representative gross images of thermal lesions produced in liver tissue, ex vivo, using 650, 808, 980, and 1075 nm lasers. The 1075 nm laser images are shown for optimized laser parameters during power escalation studies (7.2 W, 15 s).

For the 1075 nm laser wavelength, power escalation was needed in search of creating a thermal lesion in liver. Once the damage threshold of liver was surpassed, a thermal lesion became visible. (Figure 3.6).

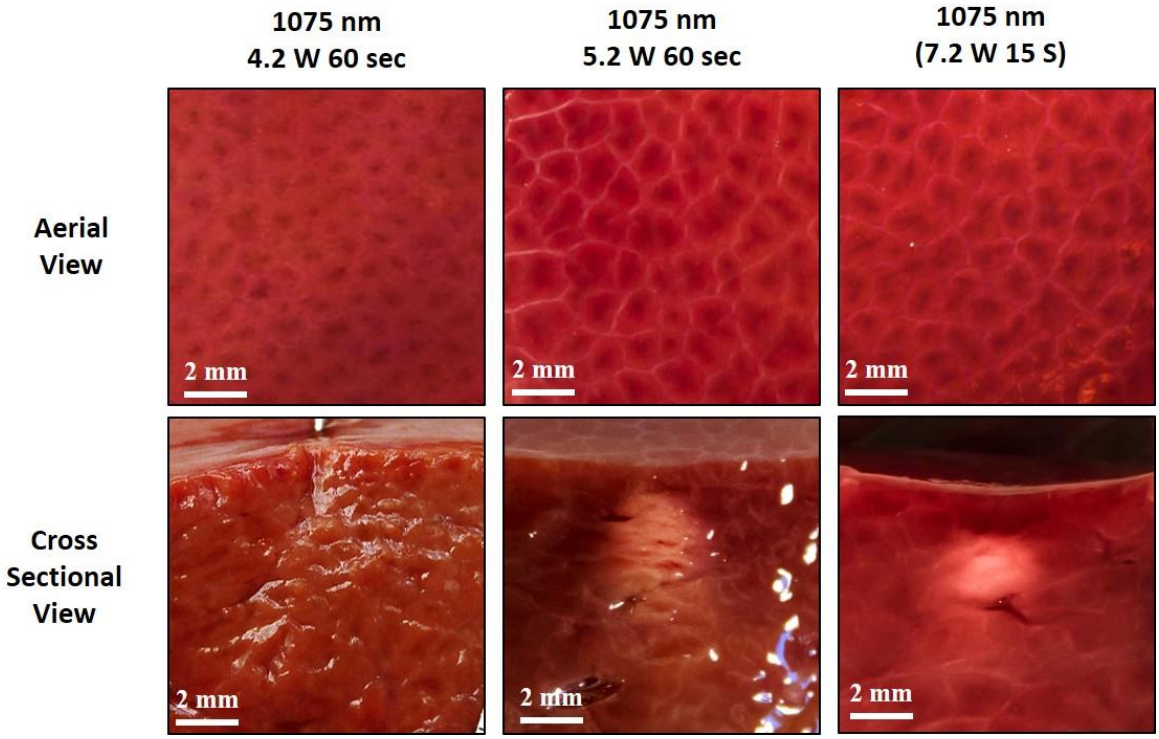

Figure 3.6. Representative gross images of thermal lesions produced in liver tissue, ex vivo, using 1075 nm laser wavelength. Power escalation was needed in order to create thermal lesions.

3.4. Discussion

The majority of therapies utilizing lasers in conjunction with applied cooling techniques only preserve a thin layer (200-400 μm) of tissue during cosmetic dermatological laser procedures. However, the ability to preserve a thicker tissue layer on the order of several millimeters by optimization of the laser and cooling parameters may lead to new noninvasive laser applications in other surgical fields as well. For example, in

urology, development of a noninvasive laser vasectomy procedure preserving the scrotal skin (~ 1 mm thick) may eliminate fear of bleeding, pain, and infection associated with conventional no-scalpel vasectomy. Also, endoscopic laser treatment of female stress urinary incontinence, which preserves the vaginal mucosa (2-3 mm thick) during thermal remodeling of the endopelvic fascia may be less invasive than current conventional surgical sling and radiofrequency energy-based procedures.

3.4. Conclusions

Four lasers spanning the optical window in the visible to near-IR spectrum were tested for producing deep subsurface thermal lesions in porcine liver tissue, *ex vivo*. Surface tissue was not preserved at the 650 nm wavelength, and preserved tissue layers for the 808 and 980 nm wavelengths were superficial. Only the 1075 nm wavelength preserved a thick tissue surface layer of ~ 2 mm. These results are consistent with other previous reports which measured the optical properties of liver tissue in the visible and near-infrared spectrum for potential photodynamic therapy (PDT) and laser interstitial thermal therapy (LITT) applications [8,11-12]. However, this study provides a comprehensive wavelength comparison for deep subsurface thermal lesion generation in tissues using red and near-IR lasers in combination with contact cooling methods.

CHAPTER 4: Optical, Thermal, and Tissue Damage Simulations

4.1 Introduction.

The objective of the simulation study was to help optimize the wide range of experimental laser parameters. Optical, thermal, and tissue damage simulations were used for comparison to the previous experimental results in chapter 3.

4.2 Monte Carlo Simulations.

To simulate the probability of the distribution of photons deposited in tissue, a standard Monte Carlo (MC) program was adapted for these studies [13]. This program modeled photon transport through tissue layers having plane parallel geometry. To achieve a sufficient distribution of photons in the tissue, one million photons were used in this MC simulation. Each simulation run of one million photons took approximately ten minutes depending on the complexity of the input. A previously reported convolution program was used to fit the results to an actual laser beam of known power, profile, and beam size [14]. This MC simulation program was modified from a previous simulation software package [15]. The following optical properties of absorption, scattering, and anisotropy of the liver tissue were used for the simulation, based on the literature (Table 4.1) [16]. This MC simulation model used square mesh dimensions of 350 x 350, in which each square was equally spaced to be 28.5 x 28.5 μm.

Table 4.1. Optical, thermal and Arrhenius integral values used in the simulations.

Laser Parameters	Optical Properties	Thermal Properties	Damage Parameters
λ = 1075 nm	n = 1.38	κ = 0.566 W/m-K	A = 5.51 x 10^{41} s^{-1}
P = 7.2 W	μ_a = 0.5 cm^{-1}	c = 3590 J/kg-K	E_a = 2.769 x 10^5 J/M
Spot = 5 mm	μ_s = 80 cm^{-1}	ρ = 1050 Kg/m^3	T_c = 73.4 ^oC
t = 15 s irradiation	g = 0.97		
t = 15 s cooling	[16]	[16]	[17]

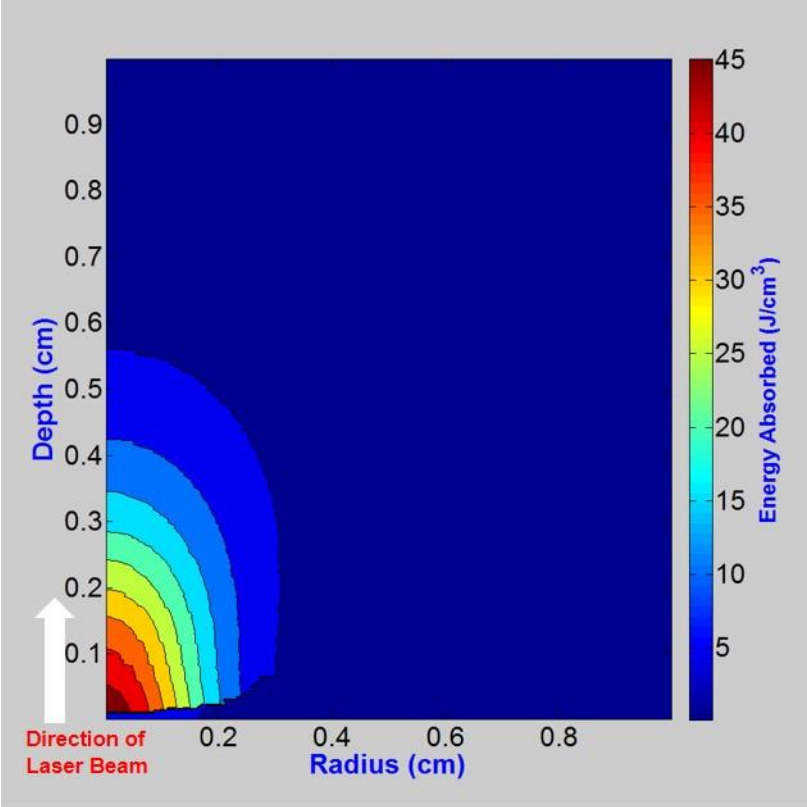

Figure 4.1. Output of Monte Carlo simulation with absorbed photon distribution in 2 spatial dimensions (1 cm x 1 cm).

Figure 4.1 shows the MC simulation in which the photons start from the left bottom corner (0, 0) and propagate upward for a laser beam radius of 2.5 mm. For laser radiation output at the 0 mm location, the 1-dimensional distribution of energy absorbed is displayed in Figure 4.2. Note that contributions due to subsurface scattering causes the absorbed energy peak to shift to ~ 0.01 cm beneath the surface instead of at the surface of the liver tissue.

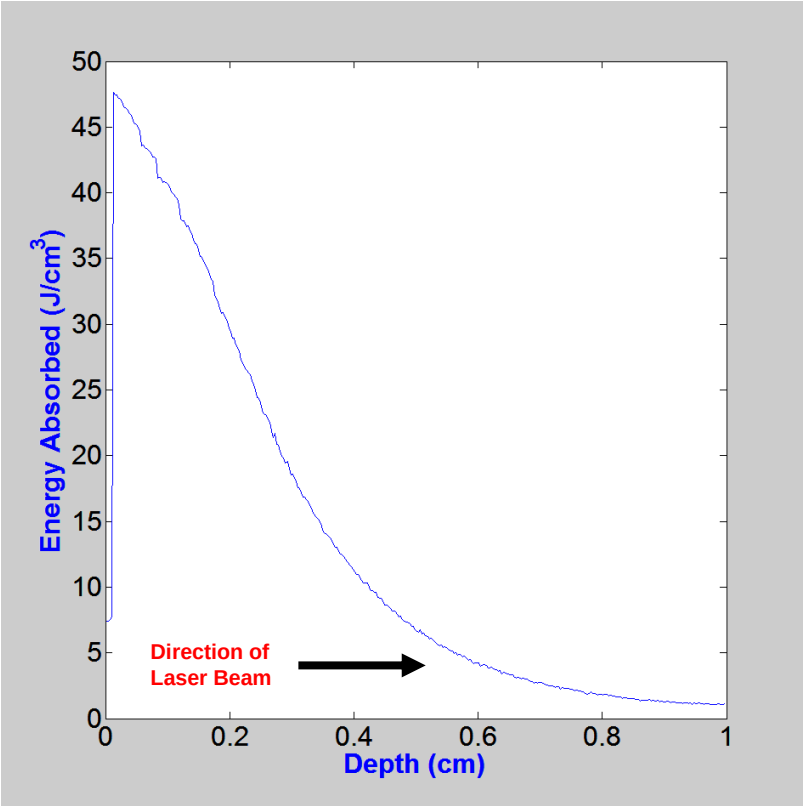

Figure 4.2. Absorbed energy distribution for liver tissue along central axis of laser beam.

4.3 Heat Transfer Simulations.

Tissue temperature simulations were conducted using ANSYS 14.5, a commercially available software package specializing in finite element and thermal problems. The heat transfer model was imported from the MC simulation model dimensions with a square mesh of 350 x 350. Each square was equally spaced to be 28.5 x 28.5 μm. The liver tissue layer was represented in the mesh and the thermal properties entered from Table 4.1. In order to simulate heat created by laser irradiation, the absorption data from section 4.2 was convolved and converted into the input of the heat transfer model in ANSYS. Since both the MC simulation and ANSYS program utilize energy per area as units, no further manipulation was needed to import data across the two programs. Furthermore, the initial tissue temperature was set at 34°C or 307 K and the contact probe to be -2 °C or 271 K. ANSYS allowed the user to focus on different frames of laser irradiation. Time t = 15 s of laser irradiation represents the final frame of laser irradiation for this simulation and thus the maximum temperature as well. Figure 4.2 shows the heat distribution after laser irradiation; reaching the maximum peak temperature of 76.2 °C (349.3 K). Figure 4.3 shows the heat distribution of the liver tissue after 15 s of post procedure cooling, with a temperature of 46.4°C (320.0 K).

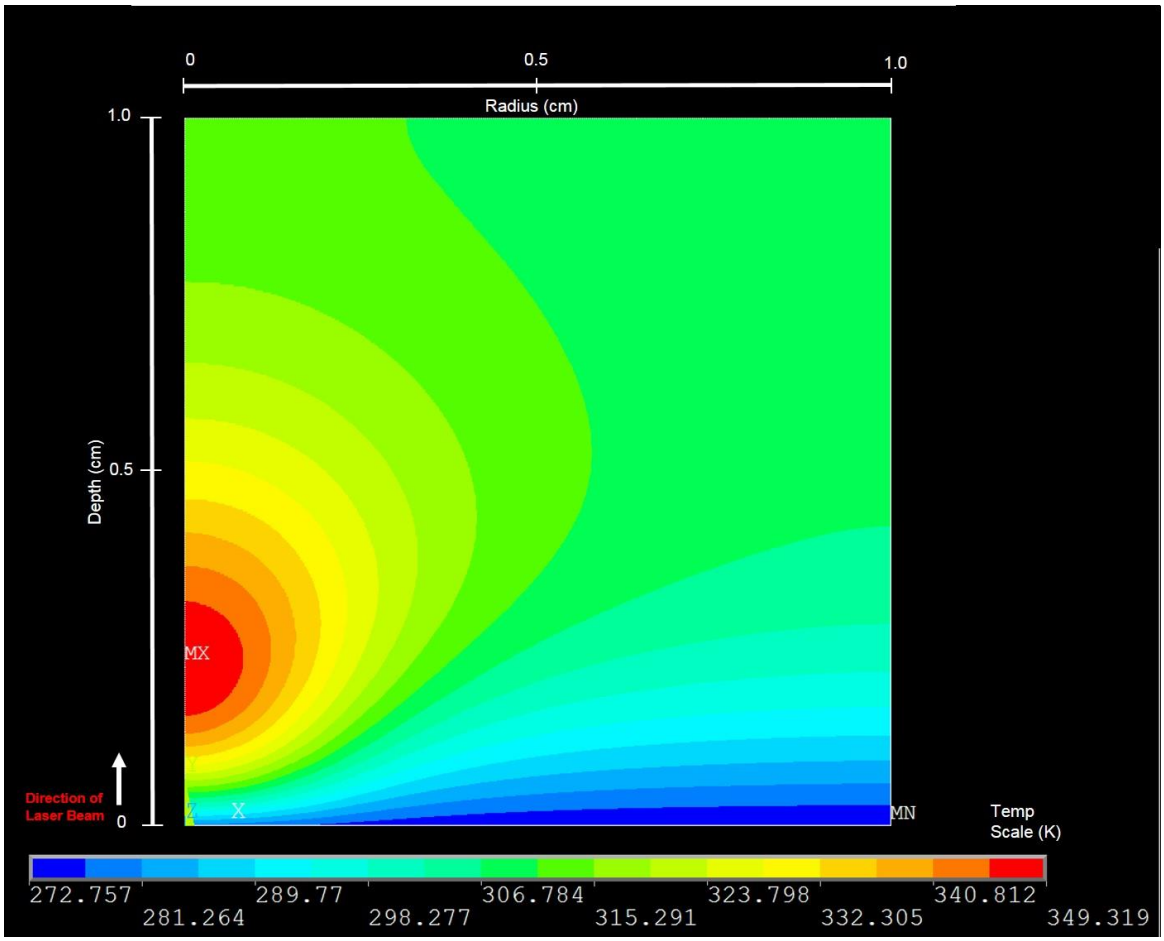

Figure 4.3. Temperature distribution in liver at 15 s after irradiation.

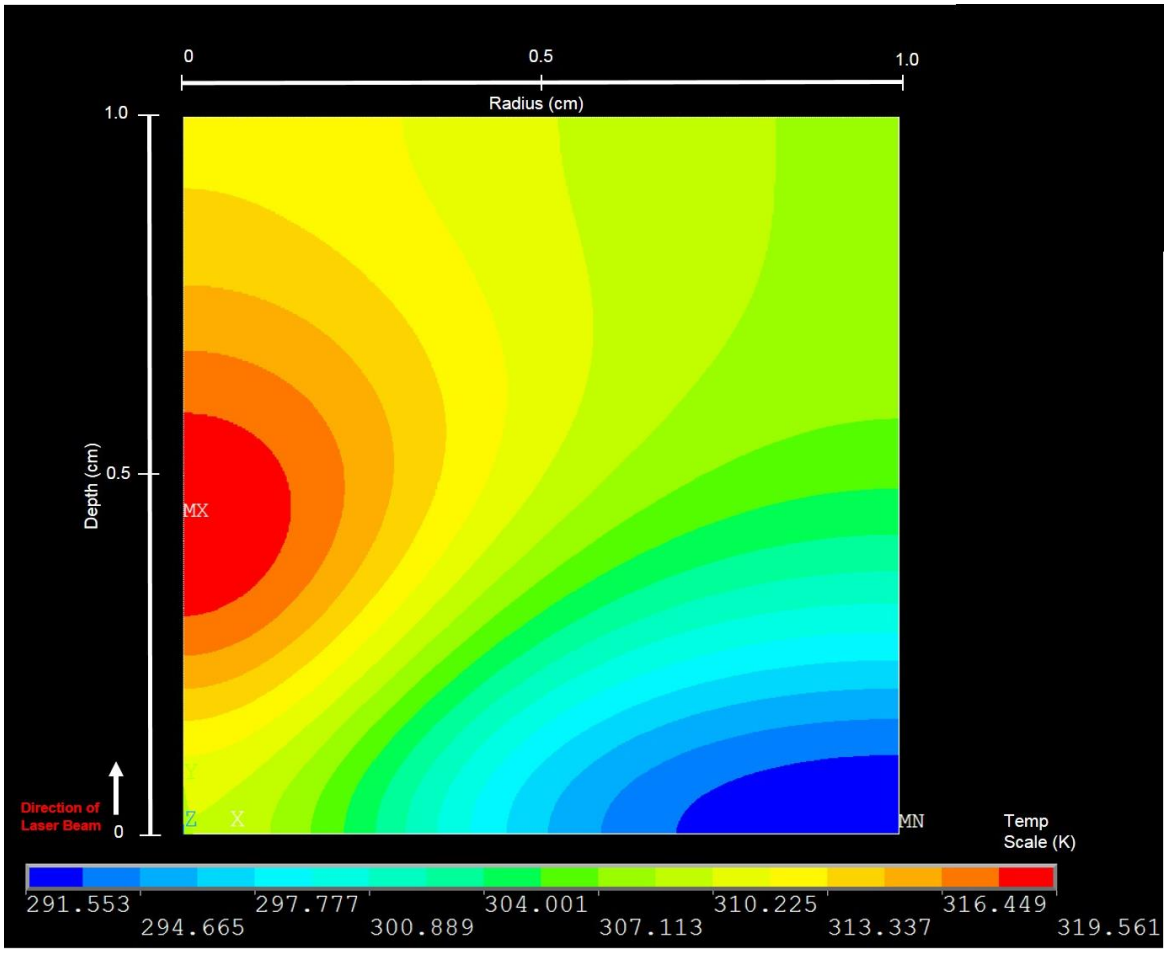

Figure 4.4. Temperature distribution in the liver after 15 s irradiation, and 15 s post treatment cooling time allowing the tissue temperature to stabilize.

4.4 Arrhenius Integral Thermal Damage Model.

In order to translate heat deposited into damaged tissue, a standard Arrhenius integral model was employed. The Arrhenius integral is used to predict and characterize thermal injury using previous experimental results from the literature. This method provides feedback for comparison with the experimental results in Chapter 3. A single thermal damage parameter, $\Omega(t)$, quantifies thermal damage experienced by the tissue (Eq.1).

(Eq. 1) $$\Omega(t) = A\int_0^{\tau} \exp(-\frac{E_a}{RT(t)})dt$$

In equation 1, A (s^{-1}) is a frequency factor determined by an experimentally derived constant; τ (s) is the total heating time; E_a (J/mol) is an activation energy of the transformation, which is also an experimentally derived constant (see Table 4.1) [18]; R (8.32 J/K mol) is the universal gas constant; and T(t) is the absolute temperature of the tissue in Kelvin.

Using Eq. 1, one can also express the damage probability given by:

(Eq. 2) $$Damage(\%) = 100(1 - \exp(-\Omega(t))$$

In Eq. 2 Damage probability is 0 % when the damage parameter is 0, and at 63.2%, damage parameter, $\Omega(t)= 1$.

(Eq. 3) $$\frac{\Delta\Omega}{\Delta t} = A\exp(-\frac{E_a}{RT_{crit}})$$

From Eq. 1, one can also derive Eq. 3, which clearly shows that when liver tissue is below the critical temperature T_{crit} (Table 4.1), the thermal damage rate is insignificant. However, the damage rate increases exponentially when the value exceeds T_{crit}.

By applying the concepts above and transferring the data from ANSYS into MATLAB, we were able to simulate the damage percentage and thermal damage of the liver tissue after 15 s of laser irradiation and 15 s of post-operative cooling. Simulation

results indicate that the preserved surface tissue layer was 1.4 mm, lesion width ~ 2 mm and lesion depth ~ 2.3 mm (Figure 4.5). Comparing the lesion dimensions from Table 3.1 in chapter 3 with the simulation results, there appears to be good agreement between experiment and theory (Table 4.2).

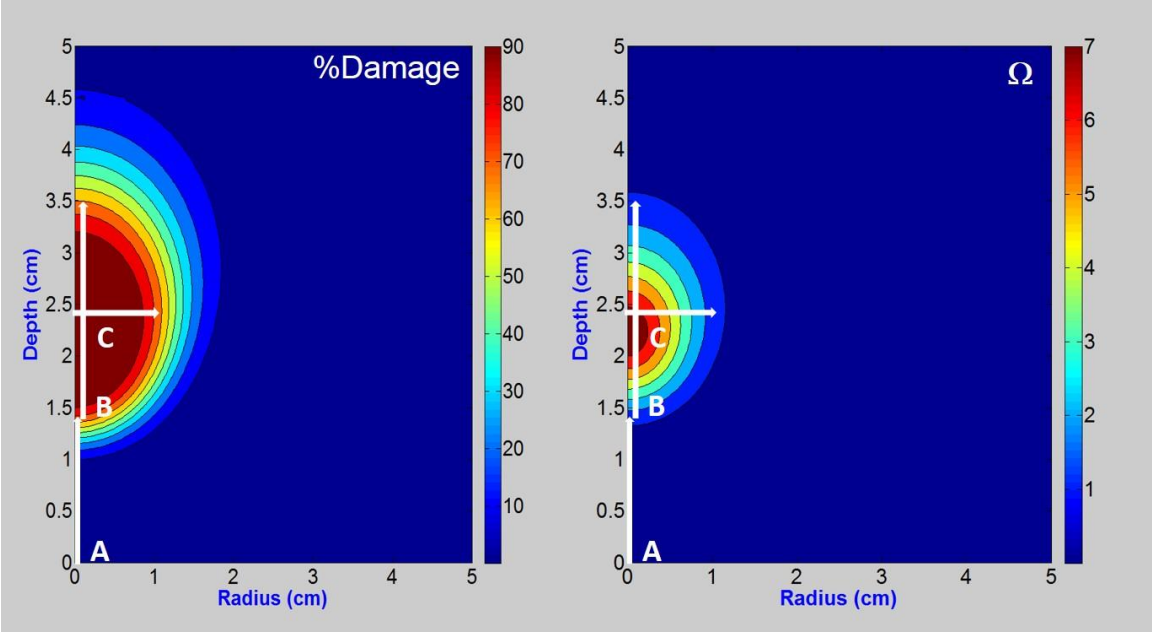

Figure 4.5. Arrhenius integral output: A) Preserved surface tissue layer = 1.3 mm. B) Lesion depth = 2.2 mm. C) Lesion width = 2.0 mm

Table 4.2. Comparison of simulations and experimental results for liver lesion dimensions at λ= 1075 nm.

Lesion Characteristics	**Simulations**	**Experiments**
Preserved Surface Tissue Layer (mm):	1.3	1.7 ± 0.5
Lesion Width (mm):	2.0	2.3 ± 0.4
Lesion Depth (mm):	2.2	2.3 ± 0.5
Lesion Area (mm^2):	3.5	4.6 ± 1.8
Sample size (N):	NA	6

4.5 Conclusions.

The optimal laser wavelength tested for creation of deep subsurface thermal lesions during contact cooling of tissues was 1075 nm, which preserved a surface layer of ~ 2 mm in Chapter 3. Monte Carlo, heat transfer, and Arrhenius integral thermal damage simulations were then conducted at this wavelength, showing good agreement between experiment and simulations (Table 4.2). The near-infrared laser wavelength of 1075 nm provides deep subsurface thermal lesions in liver tissue while preserving up to 2 mm of the tissue surface from thermal result, for potential noninvasive laser applications.

CHAPTER 5: Laser Probe Development

5.1 Introduction.

After identifying the optimal laser wavelength for creation of subsurface lesions in Chapter 3 and simulations in Chapter 4, preparation for future pre-clinical and clinical studies is a logical next step. The side-firing laser probe's head shown in chapter 3 has dimensions of 3.5 cm length x 2.7 cm width x 3.2 cm height, which is too large for endoscopic application. In order to prepare for these studies, new laser probe designs were explored to miniaturize the laser delivery method and then tested with porcine liver for rapid feedback in measuring subsurface thermal lesion formation. Since chapter 3 demonstrated that the 1075 nm wavelength provides the deepest optical penetration depth, the following experiments were conducted using an Ytterbium fiber laser at $\lambda = 1075$ nm. The side-firing laser probe was designed as a miniaturized version of the laser probe in Chapter 3. Moreover, a diffusing laser probe was designed and tested for feasibility of use in cylindrical or tubular tissue structures such as those found in the urinary system (e.g. urethra).

5.2 Materials and Methods.

5.2.1 Balloon Catheter Probe

An 18 French (6-mm-OD) dual balloon catheter (Poiesis Medical *Duette*™) was modified for use as a fiber optic balloon catheter (Figure 5.1). After cutting the subsumed tip and sealing the second distal balloon to allow coolant to flow freely in and out of the

primary balloon, the recirculating primary balloon was formed. A recirculating chiller (T255P-D5, Thermotek, Carrollton, TX) was connected to the primary balloon, which enabled the primary balloon to provide cooling. However, the flow rate was limited to ~ 4.3 ml/sec due to the size of the balloon catheter, which limited the cooling temperature to 7°C. With air in the 9-mm-diameter balloon, the balloon probe transmitted only 71% of laser power. By filling the balloon with water and therefore, decreasing Fresnel reflection through index matching, the 9-mm-diameter balloon probe was able to transmit up to 84% of initial laser power.

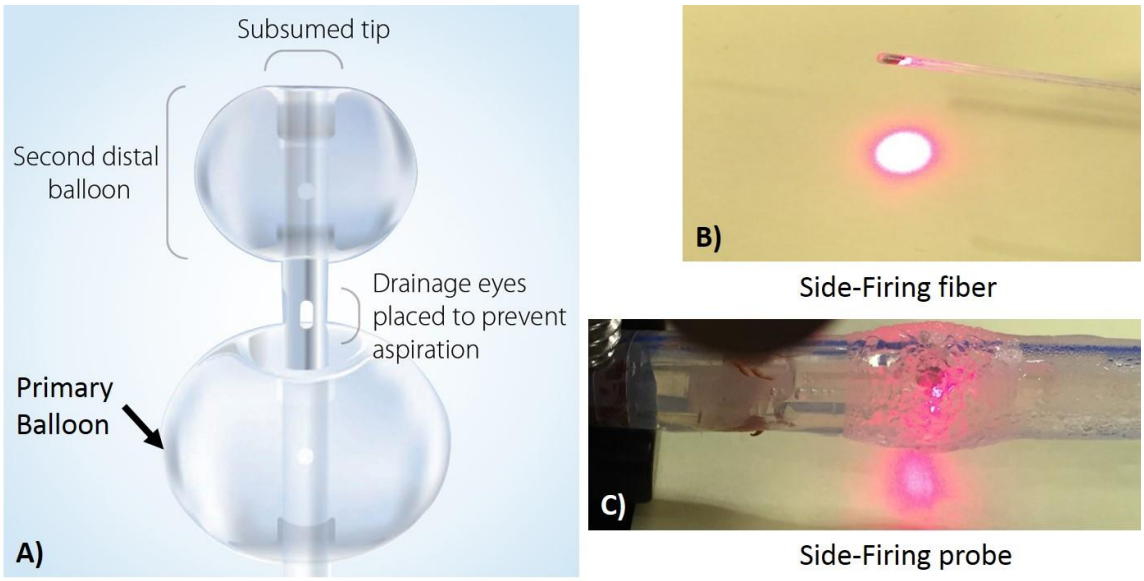

Figure 5.1. Images of the probe development. (A) 18 French dual balloon catheter; (B) Side-firing fiber with polished fiber and 45° angled, 90° reflecting gold coated rod mirror; (C) Combined balloon catheter and side-firing fiber to form side-firing laser probe.

5.2.2 Side Firing Laser Probe

The side firing fiber consisted of a polished 600 µm core fiber with 0.39 NA and a gold coated (0.98-mm-diameter) rod mirror mounted together in a quartz capillary tube

with 1.0 mm inner diameter. Once the fiber was constructed, it reflected light perpendicular (90°) to the fiber (Figure 5.1 B). After placing the fiber in a securely fitted dual balloon catheter (Figure 5.1 C), optical transmission was determined by measuring the differential of output irradiation. The fiber stabilizing fixture was built from a 16 French balloon catheter (Poiesis Medical *Duette*™) as a mold and using a UV-Cured adhesive (Norland Optical Adhesive 81) as filling, and then cured under UV light. The output beam from the 9-mm-diameter balloon probe was elliptical (2 mm length x 3 mm width). A diagram of the laser balloon catheter is provided in Figure 5.2.

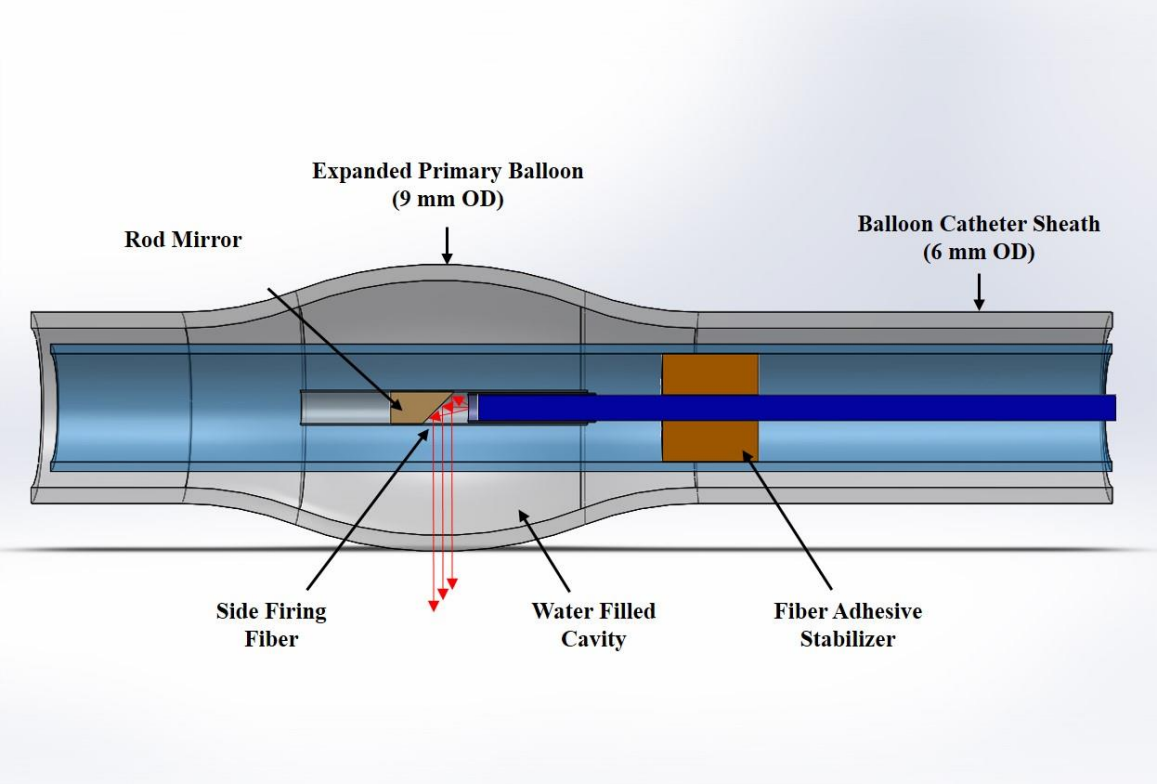

Figure 5.2. Schematic of the side-firing probe.

5.2.3 Diffusing Laser Probe

Similarly, a diffusing laser probe (Figure 5.3) was built to fit into the same 18 French dual balloon catheter. The fiber stabilizing fixture for the diffusing fiber was made with the same method as the side-firing fiber laser probe. The diffusing fiber was provided to the Biomedical Optics Laboratory by Cardiofocus, Inc. (Marlborough, MA). The fiber had a 10 mm active length and a 91% transmission rate.

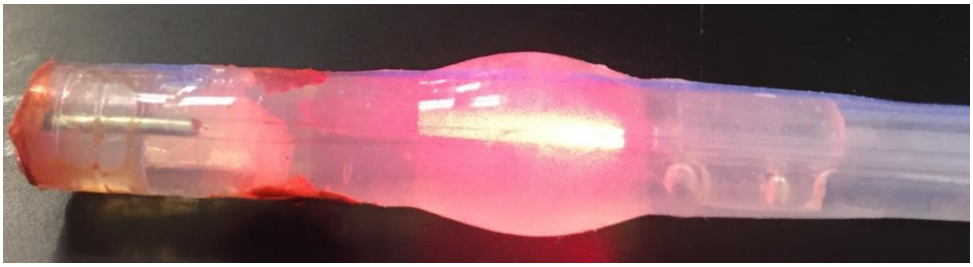

Figure 5.3. Diffusing laser probe.

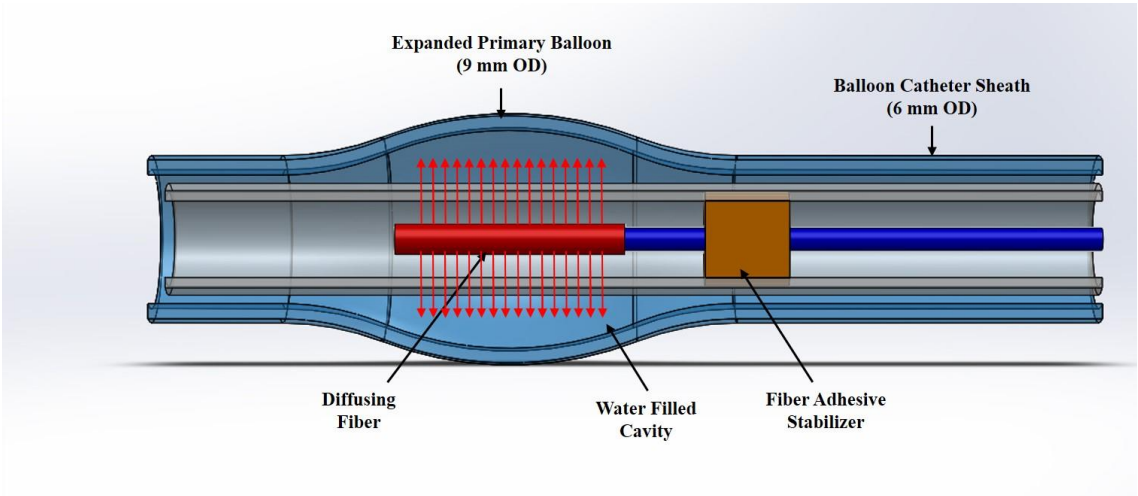

Figure 5.4. Schematic of the diffusing laser probe.

5.2.4 Radial Laser Probe

The Radial laser probe design consisted of a 1-mm-OD, 90% reflective, copper cone mirror (custom machined by the Center for Precision Metrology at UNC-Charlotte) at the tip of

the fiber, which reflected the beam 360 degrees outward uniformly (Figure 5.5), however the beam narrow ring's width was approximately 1 mm outside the balloon surface.

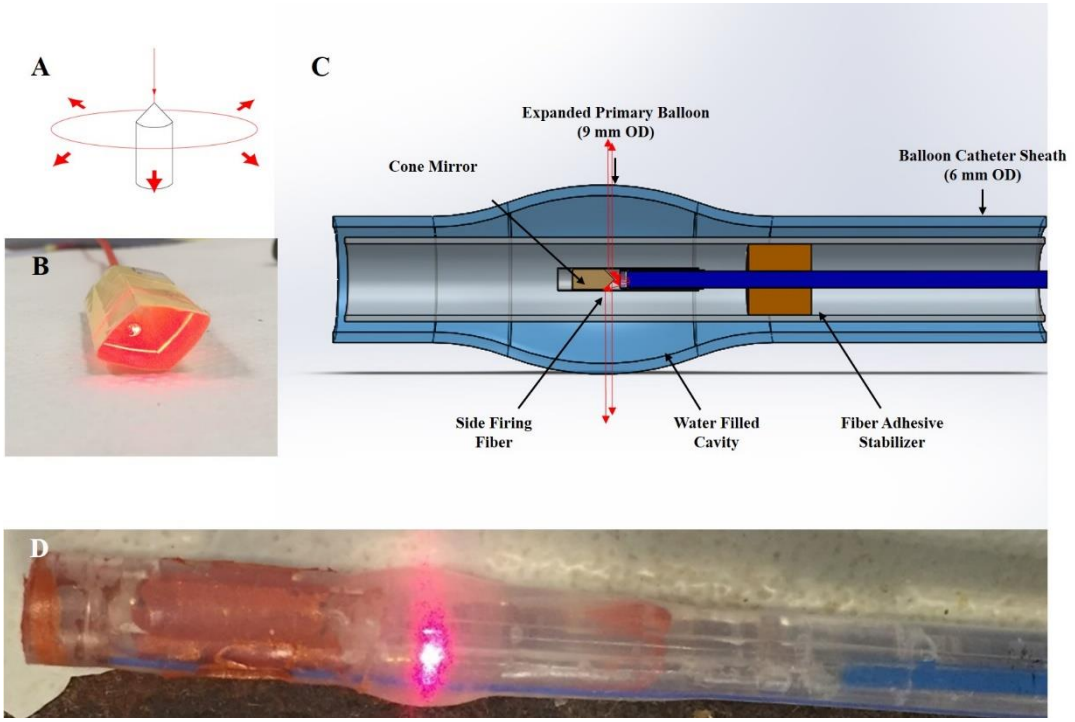

Figure 5.5.. (A) Schematic of cone lens and ray propagation; (B) Radial laser fiber before installing into balloon catehter; (C) Schematic of proposed radial laser probe; (D) Beam delivery through balloon catheter.

5.2.5 Tissue Preparation

Porcine liver tissue was used as a model for the wavelength comparison study because it could be easily quantified by immediately analyzing the gross appearance of the thermal lesions. The liver tissue was obtained from Animal Technology (Tyler, TX) and Spear Products (Coopersburg, PA). The livers were immediately frozen and stored separately. Prior to experiments, the liver tissue was thawed in cold water. The livers were cut into cylindrical samples by a stainless steel biscuit cutter measuring 38 mm in diameter and bored by drill bits measuring 4.8 mm in diameter to tightly fit the 9-mm-diameter

balloon catheter probe. Cutting and boring out the liver tissue into a cylindrical tubular structure was performed to mimic laser operation in a transvaginal or transurethral approach for future application in laser treatment of female stress urinary incontinence. The liver tissue was then warmed up to ~ 34 °C in warm water over 30 minutes.

Once the liver tissue sample was removed from the warm bath, the tissue was kept warm by using a hot plate with a set temperature of ~ 35°C. The temperature was carefully monitored using a micro-thermocouple connected to a laptop computer, similar to the setup in chapter 3. During the experiment, the side-firing laser probe was placed in contact with the liver tissue, while the diffusing laser probe was placed inside the liver tissue. After laser irradiation, the probe was removed and the lesion area was marked by inserting a pin near the lesion area to provide an accurately defined lesion location.

5.3 Results.

5.3.1 Side-firing Laser Probe Results

Table 5.1 summarizes the parameters that were used in the experiments and the characteristics of the thermal lesion. Since the beam spot size was much smaller than the spot size in chapter 3, only 1.3 W of laser power was used in the experiment for 20 seconds of irradiation. When the side-firing laser probe was in contact with liver tissue, it provided limited surface cooling; hence, a pre-cooling time of 10 seconds was used prior to laser irradiation. The balloon catheter was kept at a temperature of 7°C. Despite having a divergent beam (NA = 0.39) and the lower cooling efficiency of the balloon catheter, the

surface of the liver tissue was still preserved from thermal damage. For ten samples, surface preservation averaged 0.5 ± 0.1 mm with a lesion area of 2.4 ± 0.9 mm^2.

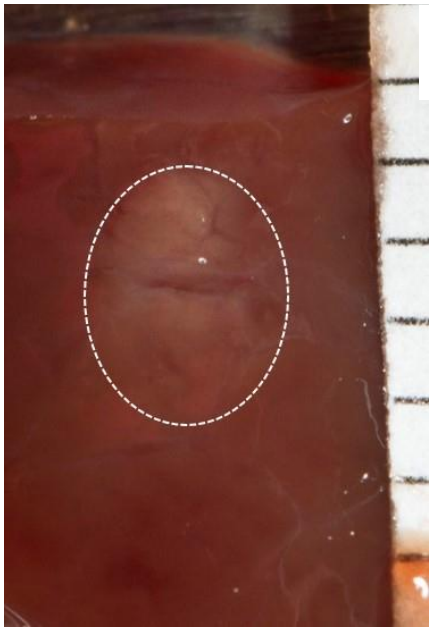

Figure 5.6. Representative gross image of thermal lesion produced in liver tissue, ex vivo, using 1075 nm side-firing laser probe.

Table 5.1. Results for thermal lesion creation using side-firing laser probe in liver tissue.

Parameters	**Side-Firing Laser**
Wavelength (nm)	1075
Laser Power (W)	1.36
Pre-cooling (sec)	10
Laser time (sec)	20
Tissue Temperature (°C)	32
Sample size (N)	10
Lesion Dimensions	
Shape	Elliptical
Lesion to surface (mm)	0.5 ± 0.1
X (mm)	1.9 ± 0.3
Y (mm)	1.6 ± 0.5
Lesion area (mm^2)	2.4 ± 0.9

5.3.2 Diffusing Laser Probe Results

Table 5.2 summarizes the parameters that were employed in the experiments and the shape and size of the thermal lesions. Since power density (irradiance) diminishes by a factor of $1/r^2$ with working distance, 15 W of laser power was used for 100 seconds. The 9-mm-diameter diffusing balloon probe was inserted into a 5 mm-ID cylindrical cavity in liver to provide tight contact of the balloon probe with the tissue. Pre-cooling was not necessary in the experiment. The balloon catheter was kept at a temperature of ~ 7°C.

Tissue surface preservation averaged 0.8 ± 0.1 mm with a lesion area of 49.4 ± 10 mm^2 (n = 10 samples).

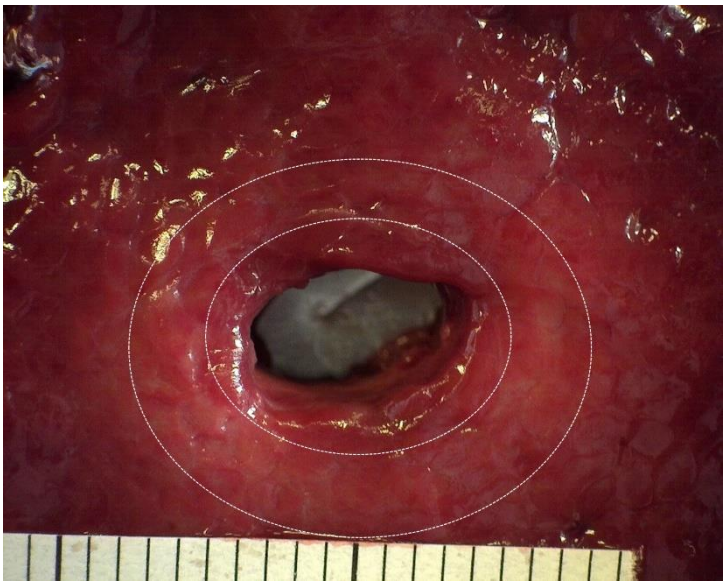

Figure 5.7. Representative gross image of thermal lesion produced in liver tissue, ex vivo via 1075 nm diffusing laser probe.

Table 5.2. Laser parameters and lesion results from the diffusing laser probe studies

Laser Parameters	**Diffusing Probe**
Wavelength (nm)	1075
Laser Power (W)	15
Pre-cooling (sec)	0
Laser time (sec)	100
Tissue Temperature (°C)	33
Sample size (N)	10
Lesion Dimensions	
Shape	Crescent
Lesion to surface (mm)	0.8 ± 0.1
Lesion area (mm^2)	49.4 ± 10

5.3.3 Radial Laser Probe Fiber Results

The radial laser probe was unable to produce any thermal lesions in liver tissue, presumably due to the combination of circular beam delivery, divergent beam, small spot diameter, and beam's narrow ring width at the tissue surface, which resulted in a significant reduction in optical penetration depth (Figure 5.8). Hence most of the thermal energy was removed from the tissue due to the chiller.

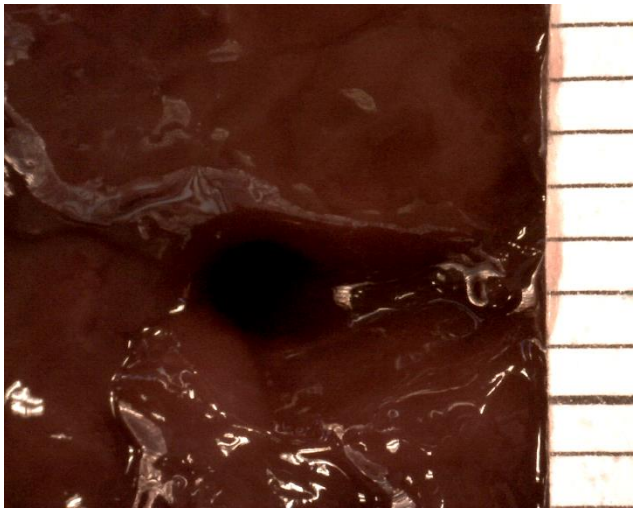

Figure 5.8. Representative image in liver tissue, ex vivo using 1075 nm radial laser probe.

Table 5.3. Laser parameters and lesion results from the radial laser probe studies

Laser Parameters	**Radial Probe**
Wavelength (nm)	1075
Laser Power (W)	15
Laser time (sec)	90
Tissue Temperature (°C)	33
Sample size (N)	9
Lesion Dimensions	
Shape	No Lesion
Lesion to surface (mm)	NA
Lesion area (mm^2)	NA

5.4 Conclusion

Some of the probe designs tested in this study have been commonly used in therapeutic laser applications in medicine. For example, diffusing fiber optic balloon catheters are used in photodynamic therapy (PDT) of cylindrical organs [19] and fiber optic probes and needles are used not only for PDT, but also during laser interstitial thermal therapy (LITT) of cancer as well, including liver tumors [20-24]. The purpose of this study was to determine which probe design provided the deepest subsurface thermal lesions in tissue.

Three laser delivery methods were tested using the 18 French dual balloon catheter probe to produce deep subsurface thermal lesions in porcine liver tissue, *ex vivo*. The radial delivery probe was unable to produce thermal lesions due to limited optical penetration depth. The side-firing probe preserved 0.5 ± 0.1 mm tissue from thermal coagulation, while

the diffusing laser probe preserved 0.8 ± 0.1 mm tissue from thermal coagulation. Since the side-firing probe has a smaller beam spot diameter and due to the scattering nature of the liver tissue, it achieved less optical penetration depth in comparison to the diffusing laser probe (Chapter 2.2 and Figure 2.5). Although the diffusing laser probe preserved more surface tissue, it required significantly higher laser power (15 W) and longer irradiation time (100 seconds). The side-firing fiber, on the contrary, due to its smaller spot diameter, required less power (1.36 W) and irradiation time (20 seconds) for lesion creation. One advantage of the diffusing laser probe is that it simultaneously treats all of the surrounding tissue; however, the limitation of using the diffusing laser probe is that the power density decays by $1/r^2$ with working distance. Presumably, if the modified balloon catheter design could be improved to allow a higher flow rate for tissue cooling (e.g. 12 ml/sec in Chapter 3 instead of 4.3 ml/sec), a deeper lesion with would be expected with greater preservation of the tissue surfaces.

In summary, the radial delivery probe failed to produce thermal lesions due to limited optical penetration depth. The side-firing laser probe preserved 0.5 ± 0.1 mm tissue from thermal coagulation, while the diffusing laser probe preserved 0.8 ± 0.1 mm tissue from thermal coagulation. While these methods produced subsurface thermal lesions in tissue, higher cooling rates and less divergent laser beams are needed for deeper penetration and greater tissue surface preservation.

CHAPTER 6: Laser Treatment of Female Stress Urinary Incontinence

6.1 Introduction.

Previous chapters described the general use of laser radiation to non-invasively target subsurface tissue structures. One application that may benefit many female patients in urology is noninvasive laser treatment of female stress urinary incontinence. Over 6.5 million women in the United States and 10 million women worldwide suffer from genuine Stress Urinary Incontinence (SUI) [25]. Only a small portion of the women in the U.S. suffering from SUI, ~ 200,000 women (3%), seek surgical intervention. Types of surgical therapy include the Burch (open) colposuspension, insertion of a sub-urethral sling, or injection of urethral bulking agents [26]. The need for general anesthesia, prolonged recovery time, incisions, concern about treatment failures with future pregnancies, and concern about procedural morbidity are some of the reasons for patient hesitation to seek SUI therapy. As a result, the remaining women afflicted with SUI use disposable absorbable products, with a cost of billions of dollars, to cope with, but not cure, the symptoms [27]. Given the numerous patient concerns about current treatment options for SUI, there is clearly a role for a non-surgical method which can improve patient quality of life, especially for a treatment that is rapidly performed, carries minimal morbidity, and provides brief recovery time.

Non-surgical treatments such as Kegel exercises, biofeedback, and pelvic floor stimulation are plagued by burdensome compliance and treatment requirements as well as by issues of efficacy and durability. Thus, the vast majority of SUI patients do not select

any definitive nonpalliative treatment. Patient surveys demonstrate that for the majority of incontinent women, treatment selection is driven by desire for a minimally invasive therapy, and expectation of treatment is an improvement in quality of life, with only a minority of patients expecting a cure. Thus, many SUI patients would prefer a minimally invasive therapy which safely improves their quality of life rather than a more invasive treatment even if associated with a higher likelihood of a cure.

Recently, a radiofrequency (RF) energy based device (Lyrette) was introduced for transurethral thermal shrinkage and micro-remodeling of submucosal collagen in the bladder neck and proximal urethra as a nonsurgical treatment for SUI, with a success rate of up to 80% (Figure 6.1) [28-46]. RF micro-remodeling uses heat to denature the sub-mucosal wall, which consists of collagenous tissue, without generating tissue necrosis. RF micro-remodeling is believed to result in a functional change in regional tissue compliance, without producing a gross change in lumenal caliber (thus avoiding stricture formation). The ability of RF micro-remodeling to safely and effectively alter tissue compliance, increase barrier function, and improve patient quality of life has been demonstrated. RF thermal denaturation, shrinkage, and remodeling of collagen tissues has also been used for treatment of fecal incontinence and gastro-esophageal reflux disease [46,47].

One limitation of this RF approach, however, is the limited RF penetration depth. RF heating decays rapidly with depth, proportional to $1/r^4$ ($1/r^2$ term for resistive heating and $1/r^2$ term for electric field strength). Increasing RF power only accelerates thermal coagulation at the tissue surface due to the steep temperature gradient, in turn resulting in a rise in tissue impedance and further limiting RF penetration. Early less invasive attempts

to use RF energy to thermally remodel submucosal tissue failed. Current RF treatment of SUI consists of four RF needles inserted through the bladder and urethra into submucosal tissue for localized heating and thermal collagen denaturation and shrinkage, with constant water irrigation of the mucosa necessary to prevent overheating (Figure 6.1). Due to the limited penetration depth of RF energy, RF thermal remodeling for treatment of SUI is more invasive than is desired by many SUI patients seeking non-surgical treatment.

(a)

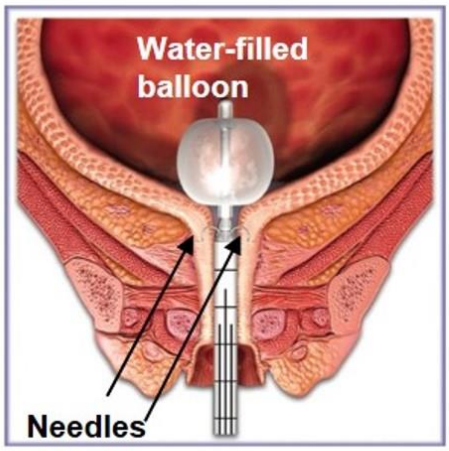

(b)

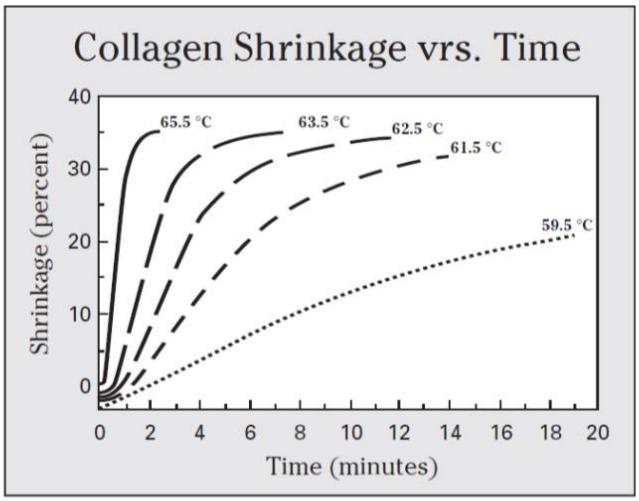

(c)

Figure 6.1. (a) Transurethral RF SUI system. (b) Probe consisting of water-filled anchoring balloon placed in bladder lumen. Four RF needle electrodes are then deployed from probe for insertion into submucosa of bladder neck and urethra. (c) Tissue is heated to 65 ^{o}C for 30 s, resulting in thermal collagen denaturation and shrinkage [41]. The needle electrodes are then withdrawn, marked shaft is rotated 30^{o}, and process is repeated for total of 12 treatment zones of ~ 0.2 mm diameter each.

Alternatively, delivery of laser energy in conjunction with applied cooling methods have been exploited with great success in laser medicine over the past few decades, specifically in cosmetic dermatology for skin resurfacing and wrinkle removal, which also involves a similar mechanism of thermal denaturation and shrinkage of collagen for tissue remodeling [49,50]. The targeted tissue structures are relatively superficial, requiring preservation of only a thin layer of surface tissue (usually epidermis and papillary dermis) measuring ~ 200-400 μm, which can be achieved relatively easily. However, these laser-based techniques have not yet been extended beyond dermatology.

Skin resurfacing lasers (e.g. Erbium:YAG and CO2 lasers) have most recently been applied in gynecology for sub-ablative rejuvenation of atrophic vaginal tissue in post menopausal women, and for treatment of female SUI [51-53]. The short-term studies appear more promising for vaginal rejuvenation, but also show modest improvements for SUI. However, these specific mid-IR laser wavelengths (2.94 and 10.6 μm) are limited to a superficial optical penetration depth of tens of micrometers and a thermal treatment zone < 0.5 mm.

It should also be noted that, unlike the endopelvic fascia, the vaginal wall is not primarily collagen, but instead composed of several layers. The first layer is the stratified squamous non-keratinized epithelium of the mucosa. (The epithelium has folds called transverse epithelial ridges that can be compressed and changes thickness with estrogen content, thinner for pre-pubescent and post menopause). The second layer is lamina propria of connective tissue, also part of the mucosa. The lamina propria is rich in blood vessels and lymphatic channels. Third is the muscular layer made of smooth muscle fibers, with outer layer of longitudinal muscle and inner layer of circular muscle. Fourth is

adventitial layer, which is connective tissue that blends with endopelvic fascia. This layer contains blood vessels, lymphatic vessels and nerve fibers [54]. Therefore, we hypothesize that in the long term, subsurface laser thermal remodeling specifically targeting the endopelvic fascia may potentially produce improved thermal tissue remodeling results for SUI compared to direct treatment of the vaginal wall.

6.2 Objective.

Our objective is to introduce a minimally invasive technique to treat SUI via a minimally invasive transvaginal or transurethral laser based probe. In order for the transurethral approach to be feasible, the probe from chapter 3 was miniaturized and tested as described in chapter 5. Since the bladder neck of the female urethra is about 8 mm in diameter, the contact cooling balloon probe was designed to be slightly bigger (9 mm in diameter) to provide reliable contact. Figure 6.1 A shows an ultrasound image taken of the female urinary system in a human cadaver at Carolinas Medical Center (CMC), along with the anatomical position of each tissue layer. For SUI treatment, the goal is to thermally remodel and tighten the endopelvic fascia without damaging adjacent tissue layers (e.g. urethra or vaginal wall). The thickness of the vaginal wall, endopelvic fascia, and urethral wall measure about 2.7, 4.3, and 2.4 mm, respectively [55,56]. The challenge of creating a minimally invasive technique for SUI focuses on treating endopelvic fascia without damaging adjacent tissue layers such as the urethra or vaginal wall. Therefore, preserving approximately 2.5 mm or greater of the surface tissue layer is the desired experimental outcome. Hence, the objective of this chapter is to use computer simulations to determine whether a “transvaginal” approach can preserve the vaginal wall while treating the

endopelvic fascia, or alternatively, whether a "transurethral" approach can preserve the urethral wall while treating the endopelvic fascia.

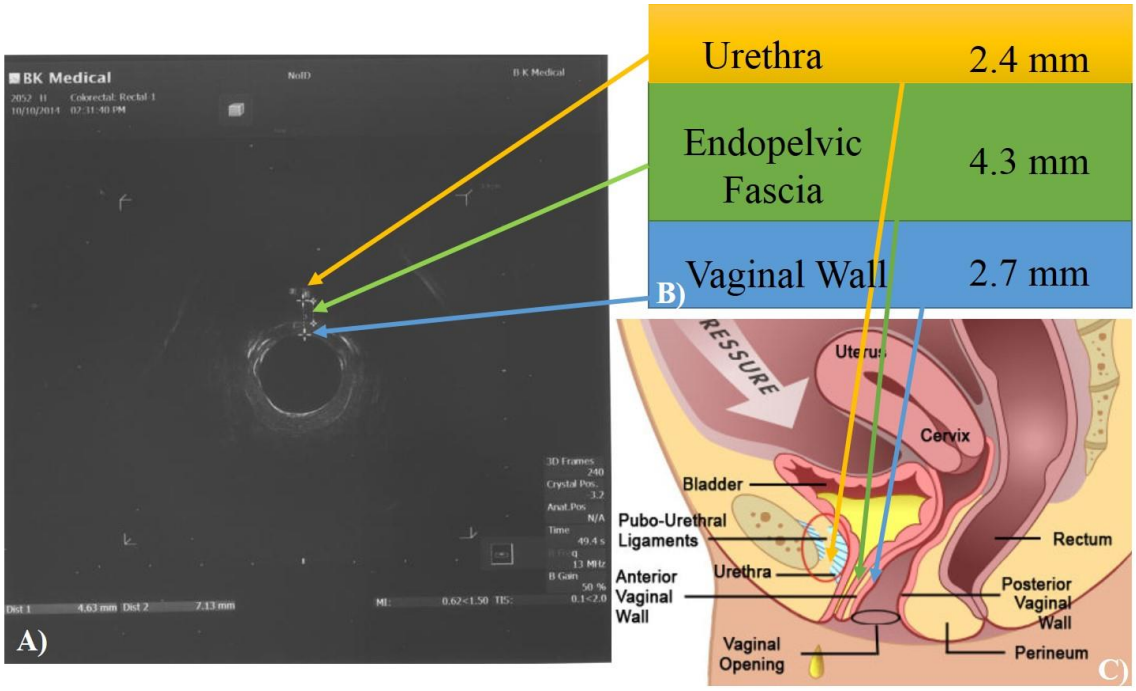

Figure 6.2. A) Ultrasound image of female urinary tract in a human cadaver; B) Diagram of tissue layers. C) Diagram of female human anatomy during SUI.

For treatment of female stress urinary incontinence (SUI), the objective is to tighten the endopelvic fascia. There are two basic endoscopic approaches for achieving this goal. One can treat endopelvic fascia through the vaginal wall, and since the endopelvic fascia is 2.7 mm below the vaginal wall, this is considered a transvaginal treatment. Another approach is to treat the endopelvic fascia through the urethra. The endopelvic fascia is 2.4 mm below the urethra so treatment is considered to be a transurethral approach. During SUI treatment, thermal coagulation is undesirable. A lower power density is required to thermally remodel and tighten the endopelvic fascia. Furthermore, liver tissue has different

thermal conductivity and optical properties than the vaginal wall, endopelvic fascia, and urethra.

6.3 Experimental Results

Table 6.1. Summary of 1075 nm laser probes with combined liver results from chapter 3 and chapter 5 indicating that larger spot size and lower temperature cooling allows deeper surface tissue preservation.

Parameters	**Balloon Diffusing Probe**	**Balloon side-Firing probe**	**Sapphire side-firing probe (5.2W/ 60s)**	**Sapphire side-firing probe (7.2W/ 15s)**
Wavelength (nm)	1075	1075	1075	1075
Laser Power (W)	15	1.36	5.2	7.2
Pre-cooling (sec)	0	10	0	0
Laser time (sec)	100	20	60	15
Tissue Temperature (°C)	33	32	33	33
Sample size (N)	10	10	5	6
Lesion Dimensions				
Shape	Crescent	Elliptical	Circular	Circular
lesion to surface	0.8 ± 0.1	0.5 ± 0.1	1.9 ± 0.5	1.7 ± 0.5
X (mm)	NA	1.9 ± 0.3	3.0 ± 0.3	2.3 ± 0.4
Y (mm)	NA	1.6 ± 0.5	2.5 ± 0.2	2.3 ± 0.5
Lesion area (mm^2)	49.4 ± 10	2.4 ± 0.9	6.0 ± 1.0	4.6 ± 1.8

Table 6.1 summarizes the current capability of our laser probe designs in liver tissue. The sapphire side-firing probe appears to be promising for transvaginal treatment application. Due to the dimension of the probe, the sapphire side-firing probe from chapter 3 enables faster cooling at the rate of 12 ml/sec; moreover, with a larger spot size the laser beam can penetrate deeper than the balloon probe in chapter 5. On the other hand, the sapphire side-firing probe's head is 3.5 cm length x 2.7 cm width x 3.2 cm, which is more than five times the size of the balloon side-firing probe, which has only 18 French (6 mm) diameter with maximal thickness of the inflatable balloon measuring 9 mm in diameter.

6.4 Simulation Results.

6.4.1 Transvaginal Approach.

After taking the previous data into consideration, several simulations were conducted similar to chapter 4 using Monte Carlo simulations, heat transfer simulations, and the Arrhenius integral thermal damage model to compute the final thermal damage produced by the laser, based on the optical, thermal and damage parameters for urinary tissues (Table 6.2). Due to the limited availability of damage parameter data, vaginal wall was modeled after smooth muscle, endopelvic fascia after collagen, and urethra modeled after aorta tissue.

Table 6.2 Simulation parameters for studying the feasibility of transvaginal and transurethral treatment using 1075 nm laser sapphire probe

Optical Properties	**Vaginal Wall**	**Endopelvic Fascia**	**Urethra**
Wavelength (nm)	1064	1064	1064
Absorption coefficient (μ_a) cm^{-1}	0.43	0.35	0.5
Scattering coefficient (μ_s) cm^{-1}	21.6	484	239
Anisotropy (g)	0.9	0.9	0.9
Refractive index (n)	1.38	1.39	1.39
Thickness (mm)	2.7	4.3	2.4
Reference	Huilan [56] Panayi [54]	Tsai [57] Muller [16]	Welch [17] Wieczorek [55]
Thermal Properties	**Vaginal Wall**	**Endopelvic Fascia**	**Urethra**
Thermal Conductivity (κ) w/m-k	0.54	0.47	0.46
Specific Heat (c) J/kg-k	3655	3200	3306
Density (ρ) kg/m^3	1088	1085	1102
Reference	Muller [16]	Muller [16]	McIntosh [46]
Damage Parameters	**Vaginal Wall**	**Endopelvic Fascia**	**Urethra**
Frequency factor (A) s^{-1}	5.73E+34	1.61E+45	5.60E+63
Activation energy (E_a) J/mol	2.40E+05	3.06E+05	4.30E+05
T_{crit} °C	88.0	80.4	78.9
Reference	Welch [17]	Welch [17]	Welch [17]

During phase 1, the Monte Carlo (MC) simulations provided a spatial distribution of absorbed photons in tissue layers (vaginal mucosa, endopelvic fascia, urethral wall). Optical properties (n, μ_a, μ_s, g) were assigned to each tissue at 1064 nm. A 5-mm-diameter laser beam at a power of 5 W for 15 seconds was used, based on previous experiments in liver tissue. In Phase 2, MC output was converted into absorbed energy, serving as input for ANSYS simulation software of tissue temperatures. Convective heat transfer was used to simulate probe contact cooling. Thermal properties (κ, c, ρ) were assigned to each tissue. In Phase 3, MATLAB code was used for the Arrhenius integral calculations. A temperature matrix was constructed from ANSYS output, and a finite sum was incorporated to approximate the Arrhenius integral calculations. Tissue damage properties (E_a, A) were used to compute Arrhenius sums.

During phase 1 optical simulations, the Monte Carlo simulations predicted that the majority of energy would be absorbed by the vaginal wall initially (Figure 6.3). Therefore, surface cooling is critical for transvaginal treatment of SUI.

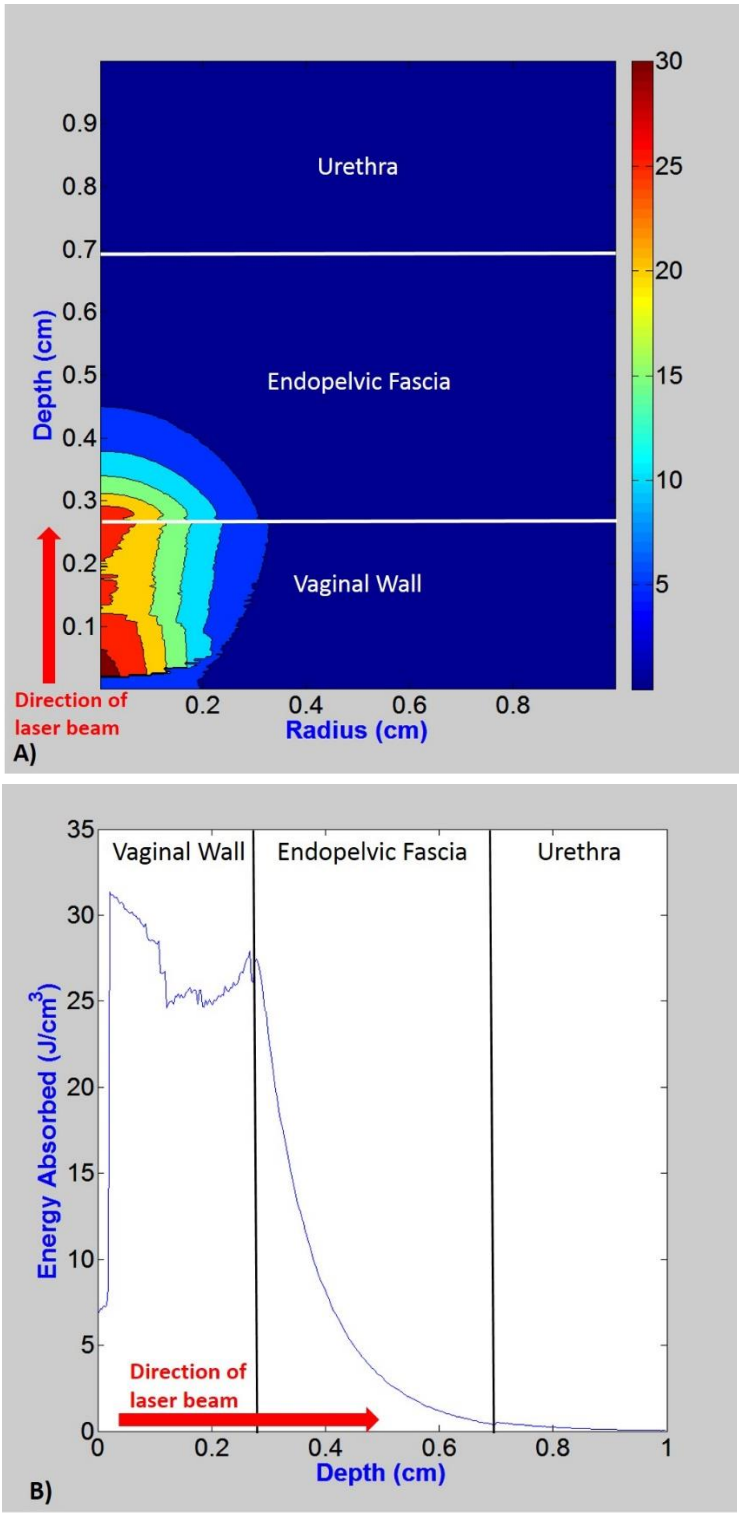

Figure 6.3. Monte Carlo simulation: A) 2-dimensional output of Monte Carlo simulation of photon distribution. B) 1-dimensional absorbed energy distribution by liver tissue at the center of laser radiation.

During phase 2 (heat transfer simulations), 15 seconds of pre-cooling at a temperature of 0 °C was applied to the tissue model prior to laser 5.0 W laser irradiation for 15 seconds. After 15 seconds of laser irradiation the internal tissue temperature in the simulation reached 71°C (344°K) at the boundary between the vaginal wall and endopelvic fascia (Figure 6.4). After laser irradiation, the laser probe was then removed and 15 seconds post-operative tissue cooling was used. The temperature was found to be 42.8°C (316°K) (Figure 6.5).

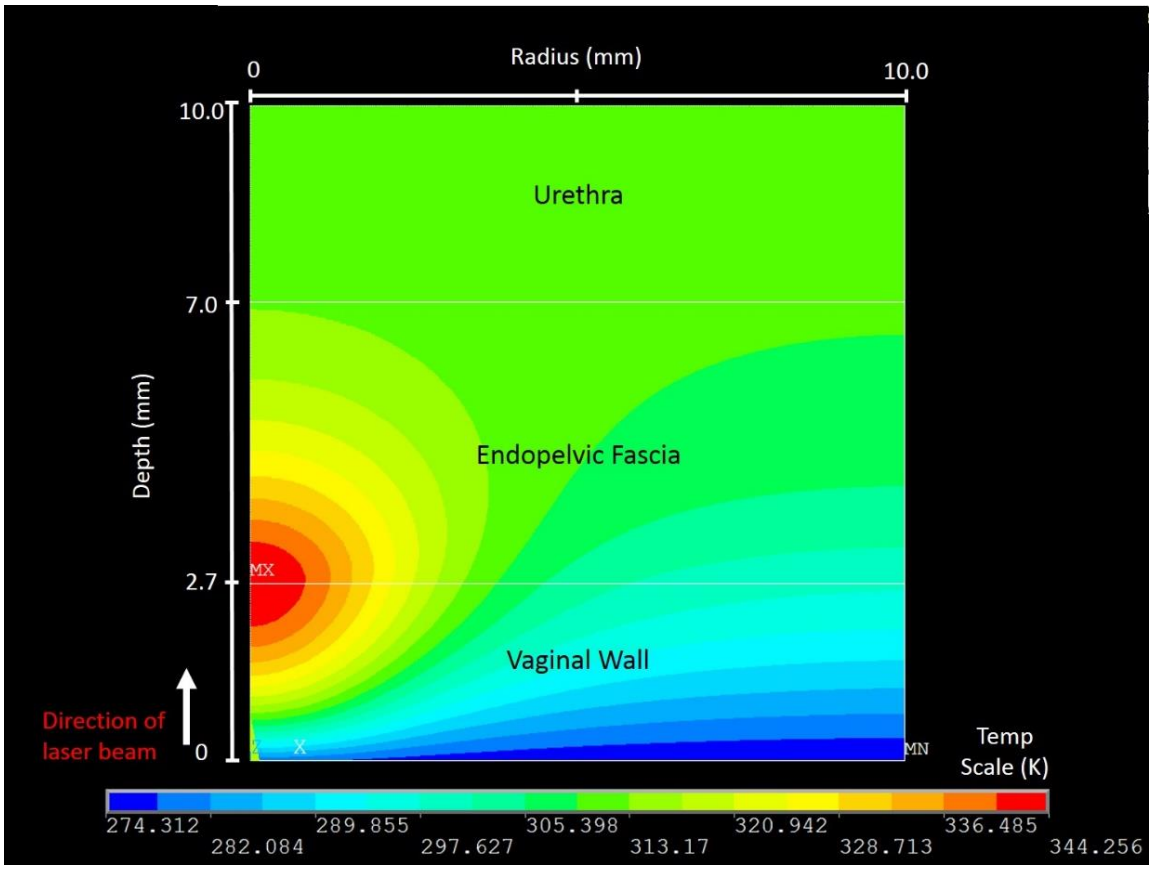

Figure 6.4. 2D temperature distribution (depth x width) after laser irradiation is applied for 15 s, using transvaginal approach. Internal tissue temperature in simulation reached 71°C (344°K) at boundary between vaginal wall and endopelvic fascia.

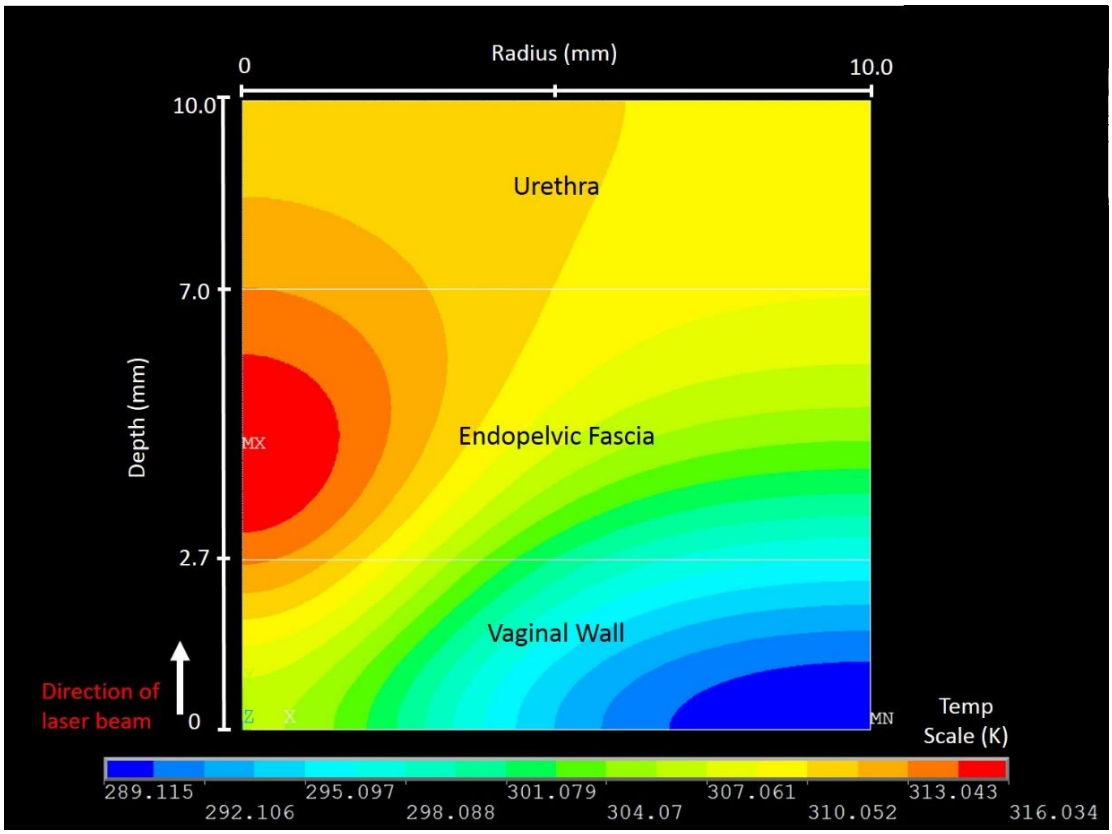

Figure 6.5. Temperature distribution in tissue 15 s after laser irradiation, for transvaginal approach. Peak temperature decreased to 42.8°C (316°K) at end of 15 s postoperative cooling time period.

In Phase 3 (tissue damage simulations), the heat distribution data was converted into percent tissue damage using the Arrhenius integral for thermal damage from chapter 4.4. Almost the entire vaginal layer (2.7-mm-thick-layer) was preserved.

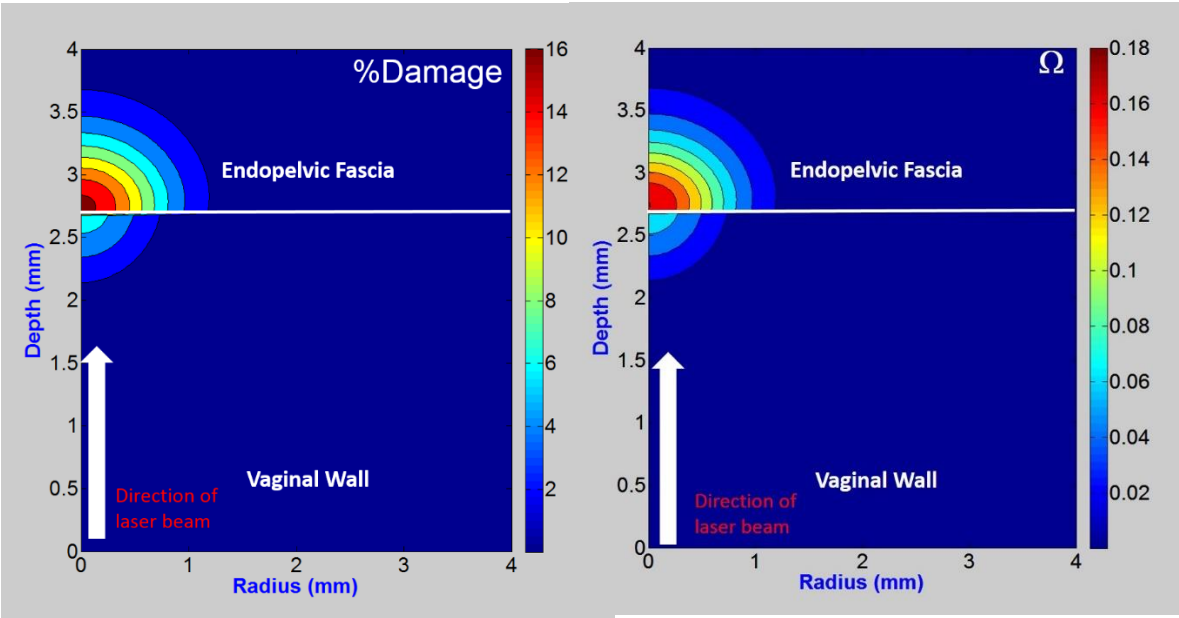

Figure 6.6. Arrhenius integral output: Almost entire vaginal wall tissue layer was preserved. The majority of heat generated in vaginal wall was removed by the contact cooling.

6.4.2. Transurethral Approach.

The transurethral approach was simulated as well, where laser irradiation propagated from the urethra to the endopelvic fascia and then to the vaginal wall in reverse order from the previous transvaginal approach. The laser parameters used were 5 W for 15 sec, and the peak temperature reached 80 ^{o}C, For this approach, 82% of energy is absorbed in urethral wall, only 18% energy is absorbed in endopelvic fascia, and 0.3% deposited in the vaginal wall beyond (Figure 6.7). The urethra is not preserved (see Figure 6.8) and only 0.5 mm of surface tissue out of the entire 2.4-mm-thick urethral wall is preserved.

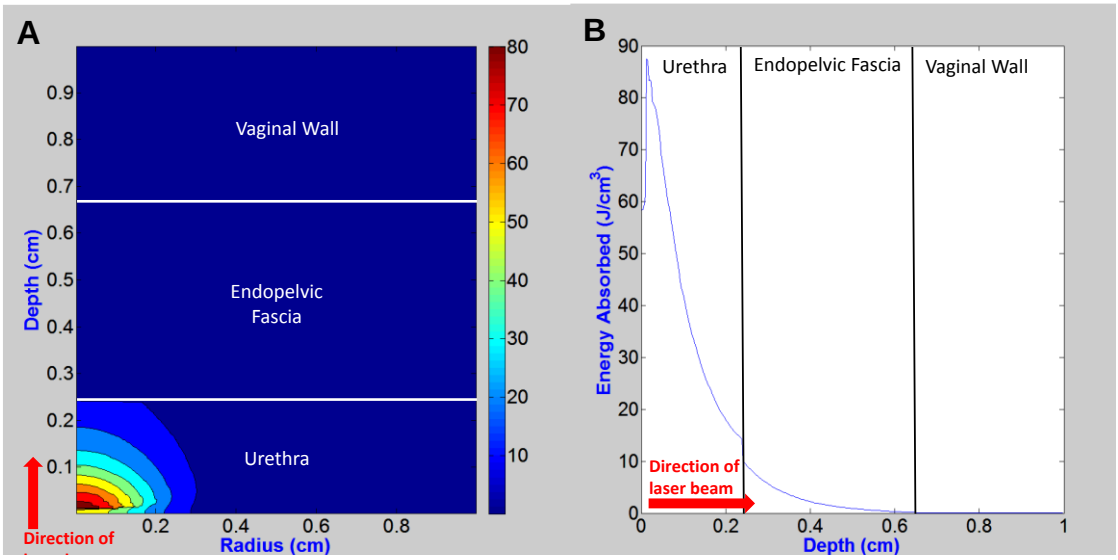

Figure 6.7. MC simulations for transurethral approach: (A) 2D spatial output of MC simulation of photon distribution; (B) 1D spatial absorbed energy distribution along central axis of laser radiation. Majority of energy (82%) is absorbed in urethral wall, only 18% energy is absorbed in targeted endopelvic fascia, and 0.3% is deposited in vaginal wall.

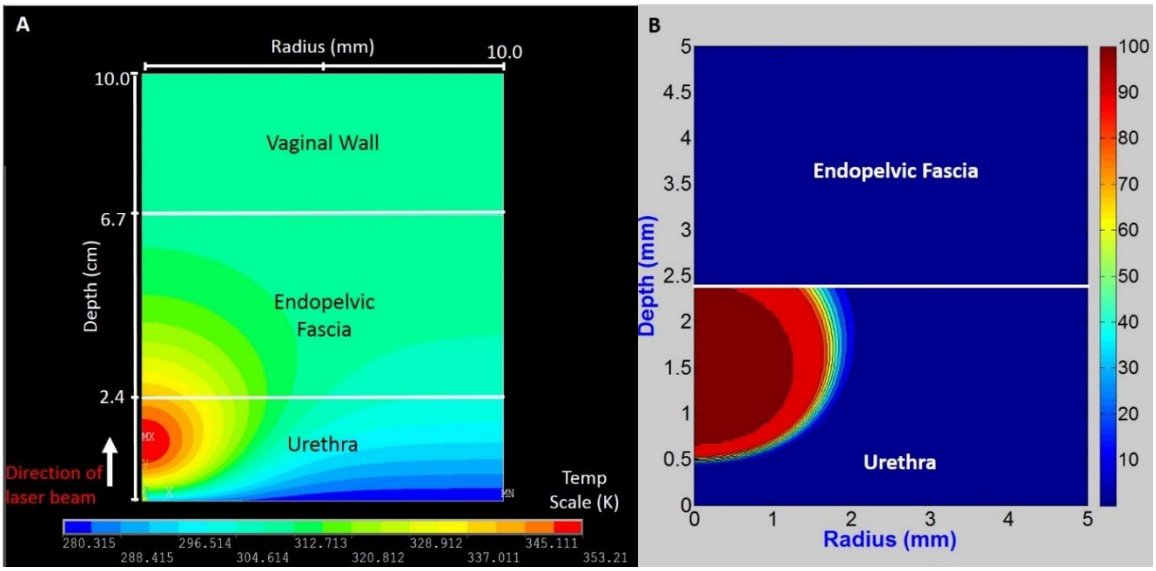

Figure 6.8. A) Temperature distribution when laser irradiation is applied for 15 s. Peak temperature reaches 80 ^{o}C (353 ^{o}K) in urethra; B) Arrhenius integral output showing undesirable damage to urethra. Only 0.5 mm of 2.4-mm-thick urethral wall is preserved from thermal damage during transurethral approach.

The transurethral approach, based on these simulations, did not achieve a desirable outcome. Even when using ideal parameters, where the laser probe was cooled to 0 ^{o}C and 5 mm diameter spot size was used, the transurethral approach was not successful compared to the transvaginal approach. In practice, due to the physical dimensions constraining the balloon side firing laser probe (in Chapter 5.2.2), with the spot size of 2 mm length x 3 mm width, which is smaller than the simulated results, it would in practice achieve even shallower penetration depth than simulated here. Furthermore, due to the limited flow rate of the balloon laser probe, the cooling in the simulation set to 0 ^{o}C is also overly optimistic compared to 7 ^{o}C achieved in practice. In summary, the transurethral approach is not likely to work for the treatment of female stress urinary incontinence.

6.5 Conclusion

Computer simulations utilizing optical, thermal, and damage parameters for vaginal wall, endopelvic fascia, and urethral wall, were conducted for both transvaginal and transurethral endoscopic approaches to minimally invasive laser treatment of female SUI. The transurethral approach, based on the simulations, did not achieve a desirable outcome. Even when using idealized parameters (for direct comparison with transvaginal approach), including probe cooled to 0 ^{o}C and 5 mm diameter laser spot size, irreversible thermal damage and tissue necrosis in the urethral wall was still predicted. However, it should be noted that use of such parameters in practice may not be possible due to limitations in the physical dimensions of the probe (< 6 mm-OD) during a transurethral approach, which would translate into a smaller laser spot diameter and lower coolant flow. A smaller laser spot diameter would in turn limit optical penetration depth, and a low coolant flow rate

would hinder efficient cooling of the tissue surface. Therefore, the experimental results with a transurethral probe may be even worse than the simulations currently predict, and with an even greater percentage of the urethral wall exposed to excessive temperatures, producing irreversible thermal damage and tissue necrosis. Furthermore, the coolant temperature setting of 0 ^{o}C used in the simulations may also be unrealistic compared to 7 ^{o}C actually achieved during our previous preliminary experiments with similar transurethral probe designs with liver in Chapter 3.

Computer simulations utilizing a transvaginal approach predicted that the majority of vaginal wall can be preserved from thermal damage, due to combination of deeper light penetration (greater percentage of energy deposited in targeted endopelvic fascia layer) and applied cooling of vaginal wall. A transvaginal approach also allows use of a larger endoscopic laser probe capable of achieving the laser spot diameter and coolant temperatures simulated in these models [59]. From an anatomical perspective, the transvaginal approach is more challenging, since it requires image guidance or precision alignment of probe with proper orientation, so that endopelvic fascia is correctly targeted. Recently, a transvaginal approach with ruler markings for precise insertion and rotation of endoscopic probe has been utilized for laser vaginal resurfacing and SUI clinical applications, so this approach is feasible [60].

There were several assumptions and limitations to our computer simulations that need to be briefly discussed. First, as previously mentioned, a rectangular geometry was used for the tissue layers, instead of a cylindrical geometry. This is a reasonable approximation since in practice, the laser probe would be applied in contact mode, slightly compressing the tissue and hence providing a flattened surface. For convenience,

simulations were also performed in two dimensions, with the assumption that results may be extrapolated to a third dimension based on symmetry in the anatomy.

Second, the dynamic optical properties of tissue layers due to temperature changes were not included in the MC simulations. Instead, the values for absorption and scattering coefficients were assumed to be constant. While significant changes in absorption and scattering coefficients are well known to occur at high temperatures (e.g. during tissue coagulation and ablation) [61], the moderate temperatures computed in these studies, especially for the transvaginal approach, may not produce significant changes. While tissue optical properties are also dependent on pressure [62], in practice, the contact probe would only lightly compress the tissue surface to provide adequate and efficient contact cooling, so such effects may be minimal as well. Nevertheless, further improvements in the MC model may be warranted in the future to study the potential effects of dynamic tissue optical parameters.

Third, the effect of blood perfusion on tissue temperatures was not included in the heat transfer simulations. For relatively short times scales considered in this study (seconds), perfusion is not a major factor. Convective heat transfer in tissue due to blood flow only becomes significant on the time scale of minutes, for example, during longer duration thermal therapies such as laser interstitial thermal therapy and hyperthermia applications [63].

A more robust MC model may be necessary which incorporates dynamic optical properties of tissues based on both temperature and pressure, and thermal effects due to blood perfusion. It may also be necessary to preserve an even thicker vaginal tissue layer than shown in these simulations. Optical clearing agents (OCA) based on alcohol or sugar

compounds have been shown to improve optical transmission through tissues by temporary dehydration which lowers water absorption, and refractive index matching through close packing of collagen fibrils which reduces light scattering. Although the vaginal wall is not highly collagenous, OCA's may provide sufficient improvement in optical penetration through this surface tissue layer, and deeper penetration through endopelvic fascia layer as well.

CHAPTER 7: Optical Clearing Agents for Enhancing Optical Penetration Depth in Tissue

7.1 Introduction

Optical clearing agents (OCA) have been used for reducing light scattering and increasing optical penetration depth in tissues for applications in optical diagnostics (e.g. imaging and spectroscopy) and laser therapy [64-70]. In this study, the primary goal is to examine the effectiveness of OCA and determine if OCA provides a deeper preservation of the surface tissue layer effectively targeting deeper subsurface tissue structures for laser thermal coagulation and/or remodeling during subsurface laser therapies. Previous studies have demonstrated the effectiveness of OCA on skin. After 60 min of OCA application, skin temporally becomes more transparent, and then slowly returns to its normal opaque appearance after another 30 min of rehydration with saline [71].

Optical clearing is achieved through both refractive index matching and dehydration. The OCA induces water flux from the interstitial space to the tissue surface, and the increase in osmolarity of interstitial fluid draws water from the cell and leads to dehydration [72]. These processes provide additional refractive-index matching and reduced scattering for skin. The reduced scattering achieved with an OCA may significantly enhance optical transmission, which in turn translates into improved optical penetration depth. Typically, optical transmission increases linearly with immersion time in the OCA solution. For example, Deng has demonstrated a 53.3% increase in optical

penetration depth for skin, *in vitro* [73]. This is desirable when using laser energy for noninvasive thermal tissue remodeling.

Moreover, optical clearing techniques have been successfully demonstrated in various tissues ranging from skin [71, 73, 74], muscle tissue [75], collagen [76], cartilage [77] and even bone [78] using different tissue OCA types and concentrations. In general, higher concentration and longer immersion time yield higher transmission. In some cases, however, optimal transmission does not always correspond to the highest concentration. For example, Jung demonstrated that 70% glycerol concentration achieved deeper light penetration than 90% glycerol in porcine skin [79].

In addition, solution temperature plays a critical role in OCA performance. Higher temperature translates into higher kinetic energy which in turns increases interaction between the solution and tissue. Deng et al, demonstrated increase in optical clearing of glycerol as a function of temperature and time [73]. As expected, higher temperatures enable greater perfusion of OCA to react faster with the sample tissue, providing an increase in the optical clearing ability in the same time frame.

7.2 Materials and Methods

7.2.1 Optical Clearing Agents

Optical clearing agents are commonly mixed with other solutions (e.g. DMSO) to enhance the rate of perfusion into tissue [74-76]. To ensure consistency between experiments, a few initial studies using porcine skin at room temperature were carried out as a baseline reference to compare to previous results, where Cilip, et al. demonstrated that

canine scrotal skin with 3:1 Glycerol/ DMSO yielded an increase in transmission of 26 ± 5% [71]. In addition, various different mixtures of common solutions were tested including, 3:1 Propylene Glycol/ DMSO and, 3:1 Ethylene Glycol (EG) / DMSO; furthermore, glycerol based solution was also tested where a mixture of 3:1 glycerol / Ethylene Glycol, and 3:1 glycerol / Propylene Glycol. The solutions above were chosen because hydroxyl-terminated types of chemicals are the most commonly used OCA agents [64-76]. All solutions were tested at the same room temperature (22 °C) to compare 3:1 Glycerol / DMSO mixture. Porcine skin was used as a sample reference. In the experiment, OCA was topically applied on porcine skin over a period of 30 minutes at 22 °C. It resulted in an average of 25.5% increased for 3:1 glycerol / DMSO mixture, 12.5 % for 3:1 polyethylene glycol/ DMSO, 26.7% for 3:1 Ethylene glycol (EG) / DMSO mixture, 30.4 % for 3:1 glycerol / Propylene Glycol, and 30.1% for 3:1 glycerol / Propylene Glycol.

Once preliminary data were collected, a better tissue model was required to simulate the OCA the effect on vaginal tissue at body temperature. Porcine vaginal tissue was used to determine the optimal combination of OCA mixtures. The following solutions were tested ($n \geq 3$ samples): 100% glycerol, 75% glycerol 25% DMSO, 75% glycerol 25% Propylene Glycol, 75% glycerol 25% Ethylene, 75% Propylene Glycol 25% DMSO and 75% Ethylene Glycol 25% DMSO (Table 7.1). OCA's were topically applied on porcine vaginal tissue over a period of 30 min, and a heated incubator experimental setup was used to maintain the tissue sample at body temperature (37 °C).

7.2.2 Experimental Setup for Measuring Percent Change in Optical Transmission

Fresh porcine vaginal tissues were obtained from Spear Products, inc. (Coopersburg, PA). The tissue was stored in saline and refrigerated for use within 48 hours. A continuous-wave, Ytterbium fiber laser operating at a wavelength of 1075 nm, and with a collimated beam diameter of 5.2 mm ($1/e^2$) was used for all of the experiments. A simple heat chamber/incubator was designed and constructed to maintain consistent temperature (37 °C) and measure the initial intensity before OCA was applied (Figure 7.1). After the OCA was applied to the porcine vaginal tissue, transmitted power was recorded from a detector (PM10, Molectron, Portland, OR) connected to a power meter (EPM1000, Molectron) every 2 min for a period of 30 min. Transmission change over time was calculated and plotted using this method.

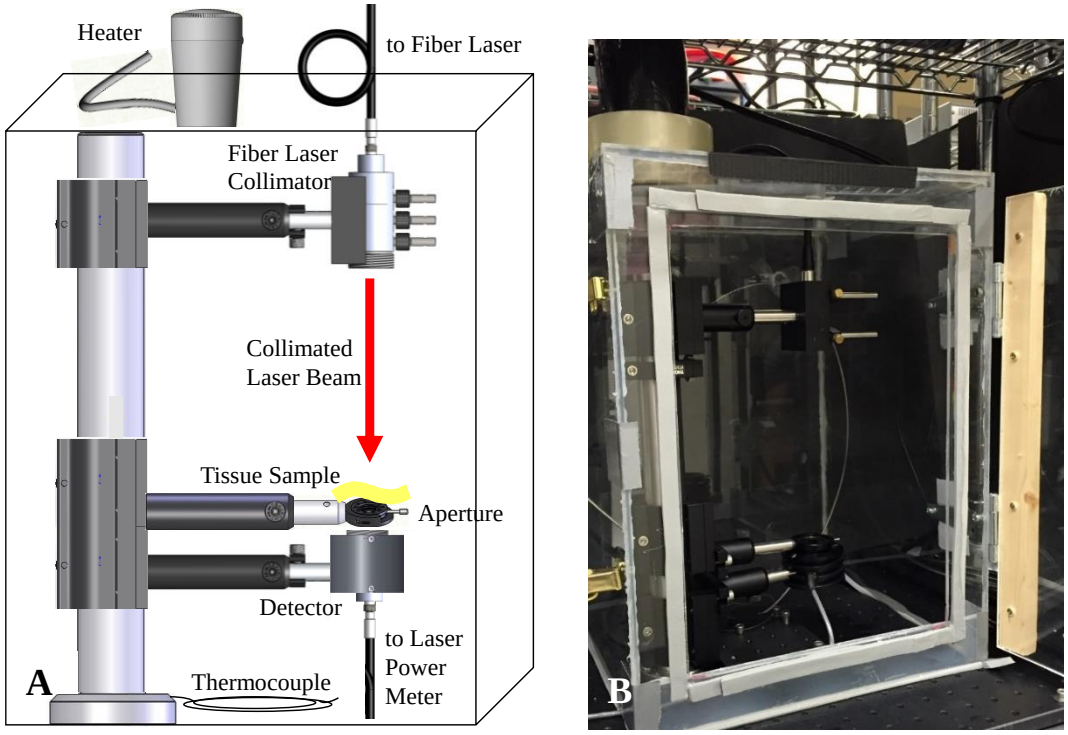

Figure 7.1. (A) Experimental setup to measure optical transmission through porcine vaginal tissue; (B) Photograph of the experimental setup.

7.2.3 Optical Coherence Tomography

Optical coherence tomography (OCT) of vaginal tissue both with and without OCA was also performed with a clinical OCT system (Niris, Imalux, Cleveland, OH) using a handheld 8 Fr (2.67 mm-OD) probe. The OCT system was a time-domain system based on a common-path all fiber interferometer designed to operate at a wavelength of 1300 nm [77], and was capable of acquiring images with 15 μm axial resolution and 25 μm lateral resolution. OCT images of vaginal tissue before and after application of glycerol were acquired to determine increased image depth based on decreased tissue scattering. Measurements were performed using software (ImageJ, National Institutes of Health, Bethesda MD) to analyze the 256 gray scale image.

7.2.4 Reflection Spectroscopy

A spectrometer (USB 4000-VIS-NIR, Ocean Optics, Dunedin, FL) was used to quantify change in reflection spectrum of porcine vaginal wall as a function of OCA application time. A fiber optic Y cable (RP21, Thorlabs, Newton, NJ) was used to connect both the light source (MI-150, Edmund Optics, Barrington NJ), and the spectrometer (USB 4000-VIS-NIR, Ocean Optics, Dunedin, FL). The fiber tip was in direct contact with the sample and reflectance data was collected using the proprietary software Spectra Suite (Ocean Optics). By comparing baseline spectrum from native tissue at 0 min with spectrum from optically cleared tissue, percentage change in reflection spectrum due to OCA was calculated.

7.2.5 Computer Simulations

Using experimental data on the change in transmission by glycerol in known thickness of porcine vaginal tissue, one can then determine the change in scattering and absorption. Using the Beer-Lambert law,

Eq.8a $$I_1 = I_0 e^{-\mu_t x}$$

Eq.9b $$I_2 = I_0 e^{-\mu_t x}$$

Eq.2 $$\frac{I_2}{I_1} = \frac{e^{-\mu_{t2} x}}{e^{-\mu_{t1} x}}$$

Eq.3 $$\mu_t = \mu_a + \mu_s(1 - g)$$

where μ_t is attenuation coefficient (cm^{-1}), μ_a is absorption coefficient (cm^{-1}), μ_s is scattering coefficient (cm^{-1}), g is anisotropy factor, x is tissue thickness (cm), I_0 is initial laser intensity (W/cm^2), I_1 is intensity measured through porcine vaginal tissue at 0 min, and I_2 is intensity measured through tissue after 30 min of OCA topical application.

A reduction in scattering coefficient is the dominant OCA effect on tissue rather than a reduction in absorption coefficient [78]. Hence, the following simulations assume that the absorption coefficient and anisotropy factor remain essentially constant and that only scattering coefficient changes upon OCA application. This calculation reduced the scattering coefficient from 21.6 to 5.9 cm^{-1} as shown below and used in Table 1. From Eq. 2, the following calculation is performed:

$$\frac{I_2}{I_1} = \exp[-\mu_{t2} x - -\mu_{t1} x]$$

$$\ln\left\{\frac{I_2}{I_1}\right\} = x[\mu_{t1} - \mu_{t2}]$$

$$\frac{1}{x}\ln\left\{\frac{I_2}{I_1}\right\} = [\mu_{t1} - \mu_{t2}]$$

Combining this expression with Eq. 3, results in the following:

$$\mu_{t1} = \mu_a + \mu_s(1-g), g = 0.9$$

$$\frac{1}{x}\ln\left\{\frac{I_2}{I_1}\right\} = [\mu_{a1} + 0.1\mu_{s1} - \mu_{a2} - 0.1\mu_{s2}]$$

Since absorption coefficient and anisotropy factor are unchanged, the equation simplifies to:

$$\frac{1}{x}\ln\left\{\frac{I_2}{I_1}\right\} = 0.1[\mu_{s1} - \mu_{s2}]$$

where μ_{s1}= 21.6 cm^{-1} , $x = 0.3\ cm$, I_1=1, I_2=1.6.

Substituting these values into the equation yields a scattering coefficient of μ_{s2} = 5.9 cm^{-1}.

Optical clearing potential (OCP) is defined as the ratio of $\mu'_s(before)$ and $\mu'_s(after)$ (see Eq.4). For human skin, glycerol was reported to have average OCP of 3 [20]; in our study, glycerol applied to the vaginal wall produced an OCP of 3.6.

Eq. 4
$$OCP = \frac{\mu'_s(before)}{\mu'_s(after)}$$

where μ'_s is reduced scattering coefficient (cm-1) given by μ_s (1-g).

Similar to Chapter 6, a Monte Carlo (MC) program was adapted to simulate distribution of one million photons absorbed in tissue layers [13, 14, 79]. A convolution program fitted results to a laser beam of known power, profile, and diameter [14]. Values for tissue optical

properties were compiled based on the Nd:YAG laser wavelength of 1064 nm used in previous experimental studies (Table 6.2).

Temperature simulations were conducted using finite element software (ANSYS 14.5). A heat transfer model was imported from MC model dimensions with mesh of 350 x 350 elements (28.5 x 28.5 μm). Tissue layers were represented in the mesh using thermal properties (Table 6.2). Absorption data from MC simulations was convolved and converted into the input of the heat transfer model to simulate heat created by laser irradiation. The initial tissue temperature was 37°C (310 K) with contact probe cooling temperature set to 0 °C (273 K).

A standard Arrhenius integral model was employed to predict thermal injury using published values [28]. A single damage parameter, Ω(t), quantified thermal damage to tissue (Eq. 5):

Eq. 5
$$\Omega(t) = A\int_0^{\tau} \exp\left(-\frac{E_a}{RT(t)}\right)dt$$

where A (s^{-1}) is experimentally derived frequency factor; τ (s) is total heating time; E_a (J/mol) is experimentally derived activation energy of transformation (Table 6.2), R (8.32 J/K mol) is universal gas constant, and T(t) is absolute tissue temperature (Kelvin). Thermal damage corresponds to Ω(t) = 1. Damage rate increases exponentially when temperature exceeds T_{crit}.

Simulations computed thermal damage based on optical, thermal and damage parameters for the tissues (Table 6.2). Due to limited availability of damage parameter data, vaginal wall was modeled as smooth muscle, endopelvic fascia as collagen, and urethra as aorta tissue. All the simulations from Chapter 6 were repeated from Monte Carlo

simulation, heat transfer simulation to Arrhenius integral thermal damage simulation for both optically cleared tissue and control tissue with optical clearing.

7.3 Result

7.3.1 Comparison of Different OCA Mixtures

Figure 7.2 shows that 100% glycerol provided an optical transmission increase of 61% in vaginal tissue at λ = 1075 nm, after 30 min. This agent provided a superior result compared to 100% concentrations of the other agents, including EG (42%), PG (41%), and DMSO (35%). Table 7.1 shows that 100% glycerol provided the optimal optical transmission increase at the deeply penetrating near-infrared wavelength of 1075 nm, in vaginal tissue over a period of 30 min. This can be explained because vaginal tissue lacks the barrier properties of skin, and hence the additional mixture of DMSO to other OCA solutions which facilitates the perfusion transport process, did not provide improved optical transmission (Table 7.1). Furthermore, due to concerns about the bio-compatibility of DMSO, Propylene Glycol and Ethylene Glycol, 100% glycerol was the preferred OCA for use in our studies.

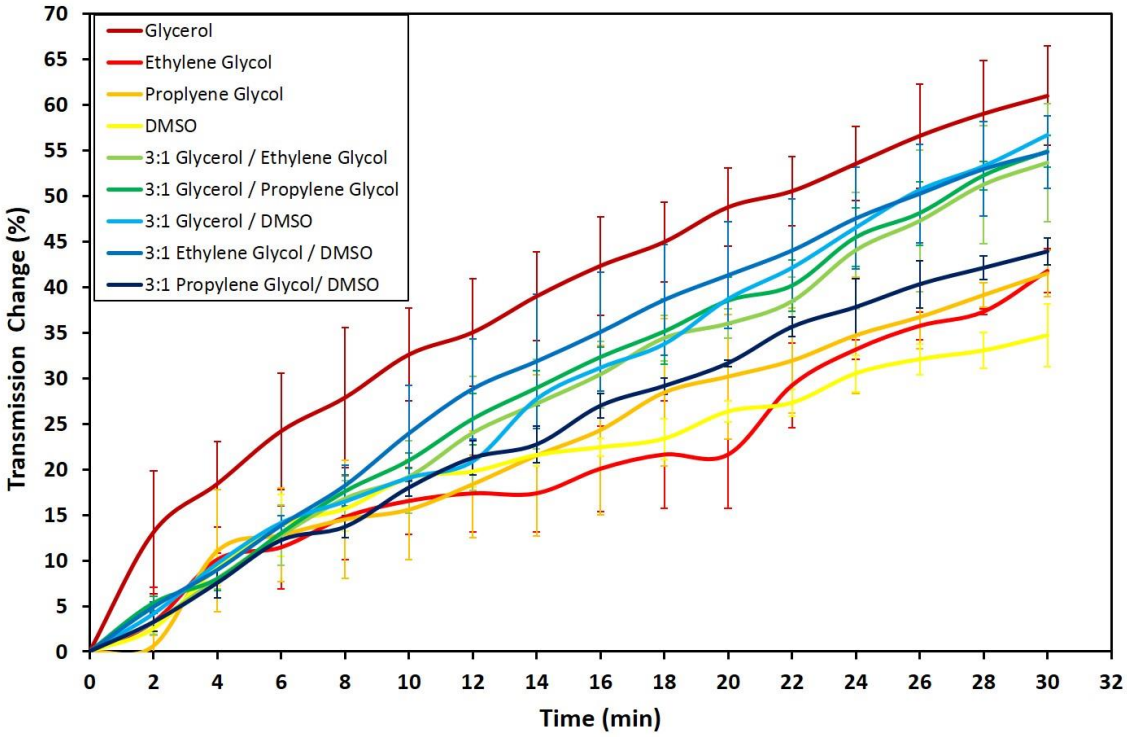

Figure 7.2. Percent increase in optical transmission through porcine vaginal tissue at 37 °C, as a function of optical clearing agent and application time.

Table 7.1. Percent optical transmission increase at 1075 nm, for vaginal tissue as a function of OCA mixture at body temperature 37 °C

Tissue tested: Porcine Vaginal tissue	100% glycerol	100 % EG	100% PG	100% DMSO	75% glycerol 25 % DMSO	75% PG 25% DMSO	75% EG 25% DMSO	75% glycerol 25% EG	75% glycerol 25% PG
Optical transmission % increase (1075nm)	**0.00**	0.00	0.00	0.00	0.00	0.00	0.00	0.00	0.00
2 min	**13.08**	3.22	0.67	2.52	4.13	3.22	4.89	3.18	5.30
4 min	**18.39**	10.08	11.07	9.21	9.64	7.53	8.95	7.98	7.96
6 min	**24.18**	11.43	12.81	13.85	14.10	12.21	13.84	12.74	12.99
8 min	**27.86**	14.76	14.52	15.66	16.43	13.68	18.21	16.77	17.55
10 min	**32.58**	16.52	15.59	19.03	19.04	17.98	23.94	19.17	20.94
12 min	**35.02**	17.36	18.38	19.74	20.84	21.25	28.83	23.97	25.51
14 min	**38.98**	17.36	21.53	21.55	27.69	22.72	31.84	27.19	28.90
16 min	**42.32**	20.06	24.32	22.40	31.12	26.98	35.07	30.40	32.29
18 min	**44.95**	21.62	28.44	23.36	33.73	29.15	38.61	34.39	35.10
20 min	**48.77**	21.62	30.18	26.34	38.67	31.66	41.31	35.98	38.50
22 min	**50.53**	29.22	31.92	27.29	42.10	35.64	44.02	38.42	40.14
24 min	**53.54**	33.16	34.70	30.52	46.51	37.81	47.55	44.03	45.44
26 min	**56.59**	35.76	36.70	32.08	50.64	40.32	50.26	47.25	48.09
28 min	**59.03**	37.32	39.11	33.03	53.25	42.12	52.96	51.24	52.23
30 min	**60.99**	41.79	41.49	34.69	56.67	43.92	54.84	53.64	54.88

7.3.2 Optical Coherence Tomography

Comparison of OCT images taken with and without OCA, and at room (22 °C) and body temperatures (37 °C), shows how diffusion of glycerol in tissue reduces scattering and allows imaging of deeper tissue layers (Figure 7.3). For porcine vaginal tissue at 22 °C, after 30 min of glycerol application, a 31.8% increase in optical transmission was measured using the following method. Since gray scale intensity is directly proportional to photon penetration depth, the 1/e intensity decrease is equal to a gray scale value of 94. At 22 °C, in the initial OCT image (t=0 min), a 1/e intensity decrease was measured at a depth of 0.484 mm. However, after OCA application (t=30 min), the new 1/e, gray scale value of 94 increased to a depth 0.639 mm, which translates to a 31.8% increase in optical penetration depth with OCA. Similarly, at 37 °C, an increase in optical transmission of 58.8% was measured. Improved optical transmission at higher tissue temperatures is achieved due to greater permeability of glycerol due to higher molecular kinetic energy, in agreement with previous studies [73].

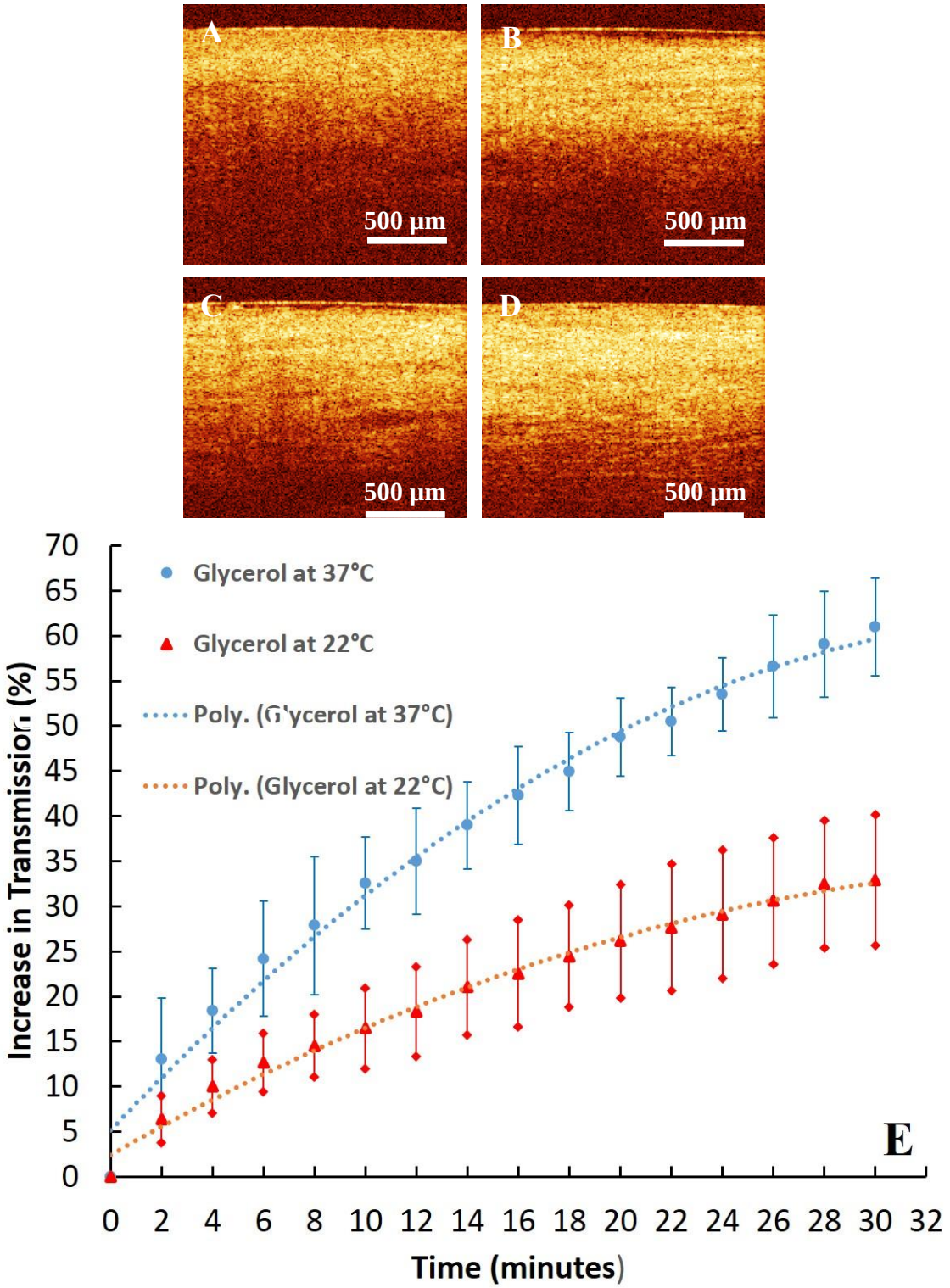

Figure 7.3. Optical coherence tomography images of porcine vaginal wall in its (A) Native state without glycerol, at room temperature, 22 °C; (B) After topical application of 100% glycerol for 30 min, at room temperature, 22 °C; (C) Native state without Glycerol, at body temperature, 37 °C; and (D) After topical application of 100% glycerol for 30 min, at body temperature, 37 °C. (E) Increase in optical transmission using glycerol, for 22 and 37 °C.

7.3.3 Reflection Spectroscopy

OCA temporarily dehydrates the tissue by increasing osmolarity, which draws water from cells, and also provides additional refractive-index matching to further reduce scattering [72]. After OCA application, the tissue reflection spectrum is altered, as observed by a change in color at the tissue surface. For porcine vaginal tissue wall, the tissue temporarily turns a darker red after 30 min of glycerol (Figure 7.4). The rapid decrease in reflection in the green and blue spectrum and slower decrease in reflection in the red spectrum was measured corresponding to progressively darker red appearance of the vaginal tissue wall. This is due to major hemoglobin absorption peaks at 420, 540, and 580 nm, which reduce the amount of re-emitted light from the tissue compared to the red part of the spectrum.

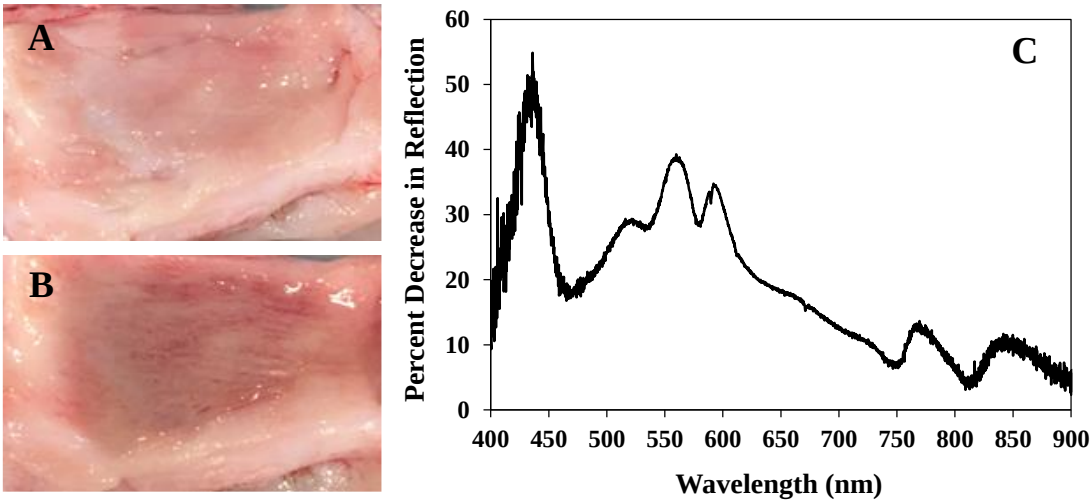

Figure 7.4. Porcine vaginal wall in its (A) native state, and (B) after topical application of 100% glycerol for 30 min. (C) Percent decrease in reflection across the visible and near-IR spectrum. Note that the lowest decrease in reflection occurs in the red (600-700 nm), accounting for the change in appearance of the tissue.

7.3.4 Computer Simulations

Monte Carlo (MC) simulations were performed using the optical parameters listed in Table 1 to compare energy deposition in the tissue layers both with and without OCA. MC simulations predicted that 50% of energy is absorbed by vaginal wall, 49% is absorbed in endopelvic fascia target layer, and only 1% is deposited in urethral wall. There was a 12% decrease in energy absorbed by vaginal wall and corresponding 12% increase in energy absorbed in endopelvic fascia layer using OCA (Table 7.2).

Table 7.2 Percent energy deposited in tissue layers with and without glycerol (1064 nm).

Parameters	**Tissue Layer**		
	Vaginal Wall	Endopelvic Fascia	Urethra
5 W, 15 s without OCA	62%	37%	1%
5 W, 15 s with OCA	50%	49%	1%

After applying glycerol for 30 min, scattering in the vaginal wall decreased significantly, enabling photons to reach deeper into the endopelvic fascia tissue layer where the scattering coefficient is greater by several orders of magnitude (Table 6.2). This energy deposition as a function of depth can also be represented by the one-dimensional plot in Figure 7.5A. Figure 7.5A plots along the center of the laser beam where the radius is zero. The initial subsurface peak is expected due to additional contributions of photons through subsurface scattering. The large peak at the interface between the vaginal wall and endopelvic fascia is due to a large increase in the scattering coefficient across the interface. The rapid decline in energy absorbed across the endopelvic fascia layers is also due to the high scattering coefficient. The spikes in the vaginal wall are contributions from the back scattering from the endopelvic fascia layer. Without OCA, the endopelvic fascia layer has 22.4 times more scattering than the vaginal wall, hence the saw tooth like shape in the first

layer. Furthermore, with application of glycerol for 30 minutes, the scattering coefficient decreases in the vaginal wall. The drop in scattering coefficient in the first layer causes an increase in scatter coefficient ratio between endopelvic fascia and vaginal wall layer to 82:1. The significant change in scattering ratio leads to a more pronounced fluctuation of energy absorbed by the vaginal wall.

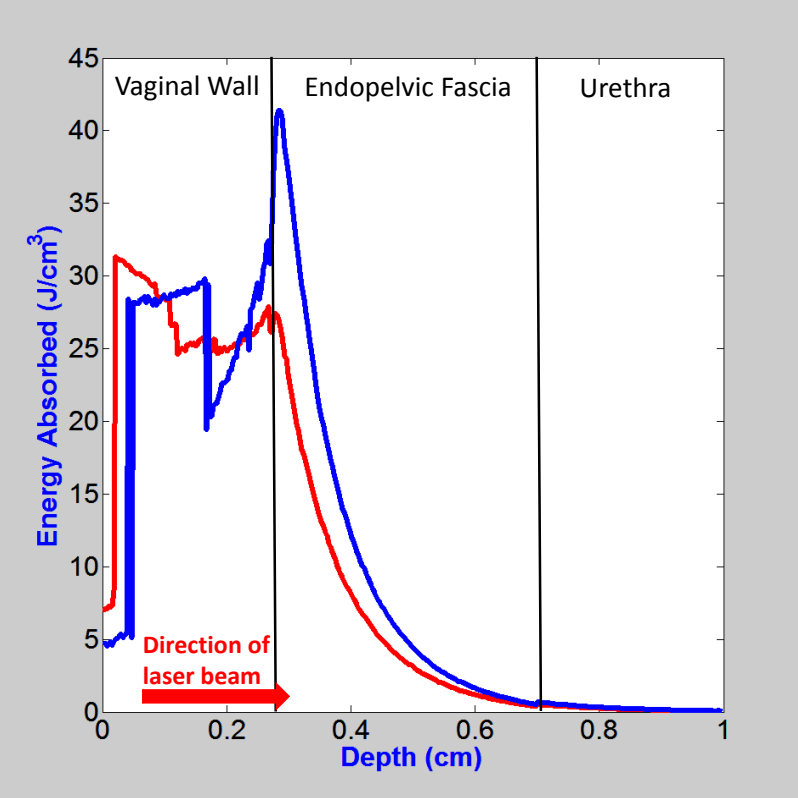

Figure 7.5A**.** One-dimensional absorbed energy distribution by porcine vaginal tissue at the center of laser radiation at 5W, both with OCA (blue) and without OCA (red).

To better understand the change in tissue optical properties over time, step by step optical clearing simulations were calculated at 6 min intervals for a total of 30 min. Using the above equations, one can tabulate a time dependent change with each data point (Table 7.3). Taking the new μ_s for the Monte Carlo simulations for both one-dimensional

absorbed energy distribution along central axis of laser radiation and two-dimensional absorbed energy distribution provides the photon distributions in Figure 7.5 B & C.

Table 7.3 Simulated change in μ_s over 30 min time period.

Time (min)	Percentage increase in transmission	μ_s (Vaginal wall)
0	0.0%	21.6
6	24.2%	14.4
12	35.0%	11.6
18	45.0%	9.2
24	53.5%	7.3
30	60.0%	5.9

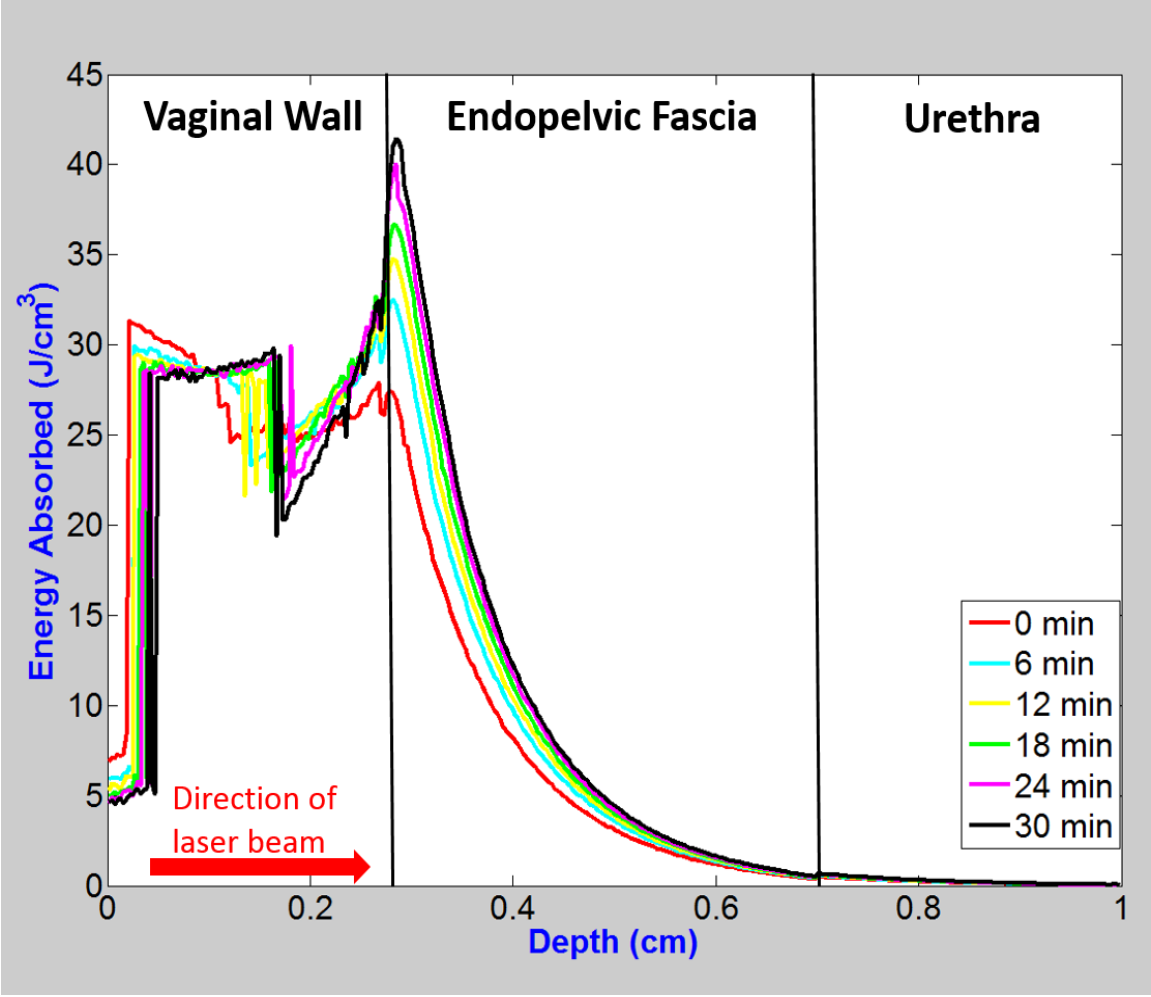

Figure 7.5B**.** One-dimensional absorbed energy distribution by porcine vaginal tissue along central axis of laser radiation at 5 W, as a function of time, from 0 minutes to 30 minutes.

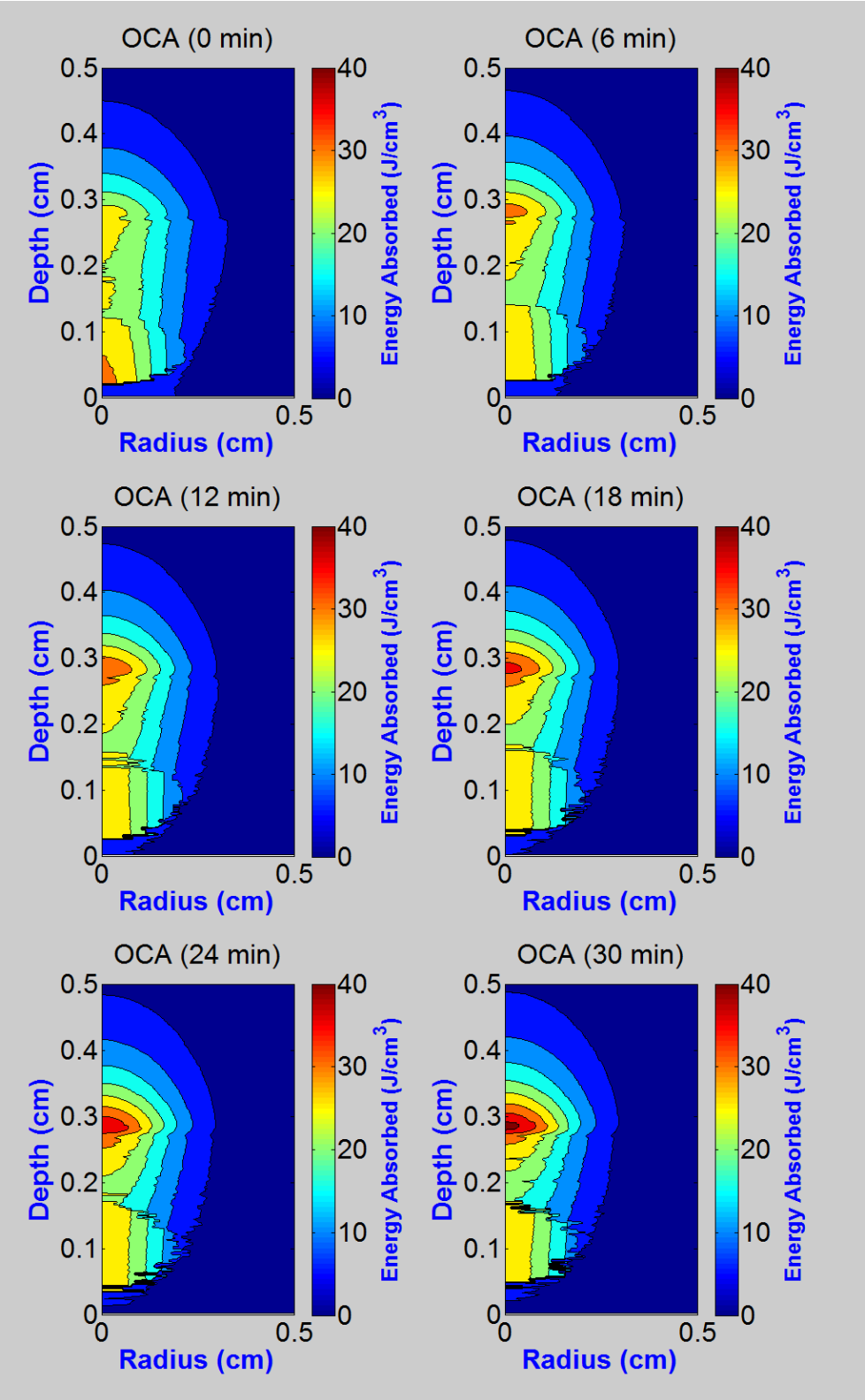

Figure 7.5C**.** Two-dimensional absorbed energy distribution by porcine vaginal tissue at the center of laser radiation at 5 W, as function of time, from 0 minutes to 30 minutes.

Figure 7.5C shows the energy absorbed by the endopelvic fascia (0.27 cm and beyond) increase over period of OCA application. By the end of 30 minutes, the first layer of the vaginal wall experienced much less energy absorption than without OCA treatment.

Heat transfer simulations were also conducted. For similar laser power simulated (5 W), use of OCA resulted in higher energy deposition in endopelvic fascia, which in turn translated into a 7 °C higher peak temperature than without OCA (Figure 7.6AC). However, 15 s after the laser was turned off, peak temperatures in the tissue decayed to a similar value of ~ 43 °C, with tissue including OCA only 0.5 °C higher than tissue without OCA (Figure 7.6BD).

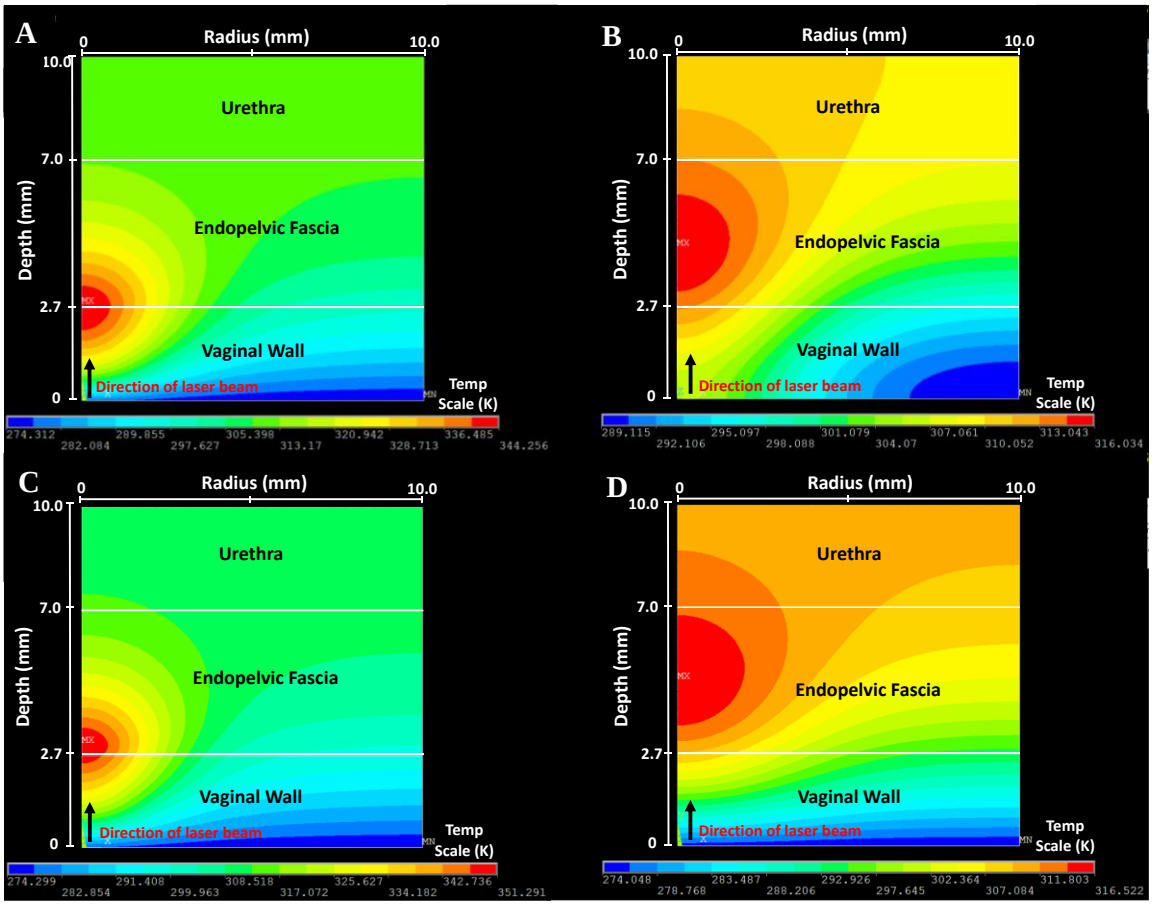

Figure 7.6. (A) 2D temperature distribution (depth x width) after laser irradiation for 15 s. Internal tissue temperature reached 71°C (344°K) at boundary between vaginal wall and endopelvic fascia; (B) Temperature distribution in tissue 15 s after laser irradiation, for transvaginal approach. Peak temperature decreased to 42.8°C (316°K) at end of 15 s postoperative cooling time period. (C) Temperature after laser irradiation for 15 s with OCA reached 78.1°C (351.3°K); (D) Peak temperature decreased to 43.3°C (316.5°K) at end of 15 s postoperative cooling time period.

Arrhenius integral calculations (Eq. 5) indicated that vaginal tissue with OCA had higher damage ($\Omega = 1.4$) compared to tissue without OCA ($\Omega = 0.18$) (Figure 7.7). This difference is due to the higher peak temperature in endopelvic fascia layer with OCA ($\Delta T = 7$ °C).

Previous clinical studies using radiofrequency (RF) energy for thermal tissue remodeling during minimally invasive treatment of female stress urinary incontinence (SUI)

targeted a temperature of 65°C in the endopelvic fascia for a period of 30 s, based on temperature versus time data for the thermal denaturation and shrinkage of collagen [44]. Using the parameters from Table 1, this translates into a damage parameter of $\Omega = 0.28$. Hence, adjustment of laser power was required for both cases (with and without OCA) to target the relevant thermal remodeling value of $\Omega \sim 0.3$. The tissue model without OCA required a power increase from 5.0 W to 5.35 W, while tissue model with OCA required a power decrease from 5.0 W to 4.45 W, to achieve a damage parameter of $\Omega = 0.3$. In practice, OCA treatment is preferred, because it not only enables laser treatment at a lower and hence safer power level, but it also improves the optical penetration depth by about 0.5 mm, thus providing a higher probability of successfully preserving the entire (~ 2.7-mm-thick) vaginal wall during the procedure (Figure 7.8).

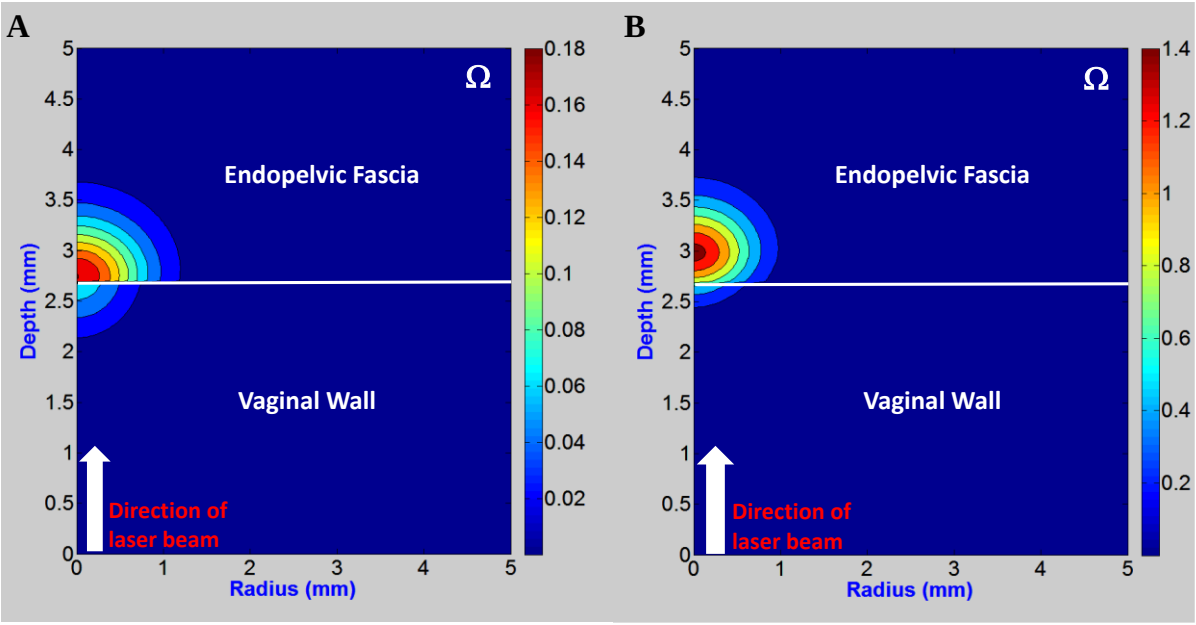

Figure 7.7. (A) 5 W without OCA yields $\Omega = 0.18$ in endopelvic fascia; (B) 5 W with OCA yields $\Omega = 1.4$ in endopelvic fascia.

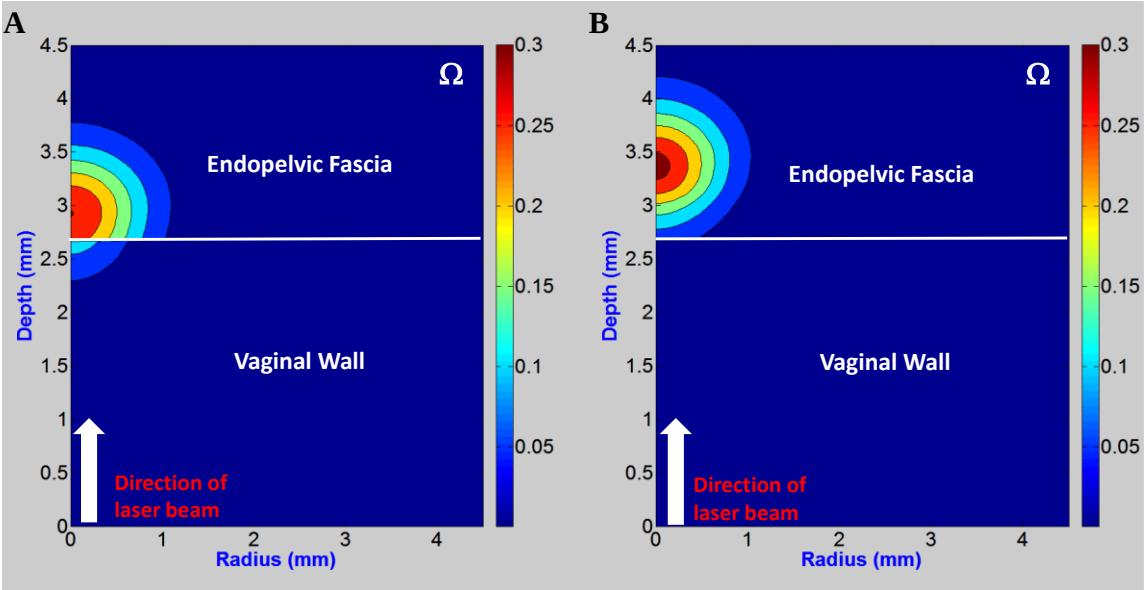

Figure 7.8. (A) Laser power of 5.35 W to thermally remodel endopelvic fascia without OCA (Ω = 0.3); (B) Laser power of 4.45 W to thermally remodel endopelvic fascia with OCA (Ω = 0.3).

7.5 Conclusion

Radiofrequency (RF) energy (mentioned in the previous chapter) produces a functional change in regional tissue compliance, without a gross change in lumenal caliber (thus avoiding strictures). However, the therapy procedure is invasive and has a limited penetration depth. On the other hand, skin resurfacing lasers, including Erbium:YAG (λ = 2.94 μm) and CO2 (λ = 10.6 μm), have recently been applied in gynecology for sub-ablative resurfacing of atrophic vaginal tissue in post-menopausal women, and for treatment of female SUI [52,53,79,80]. Because these wavelengths are directly adopted from the laser skin resurfacing field, they are limited to an optical penetration depth of only tens of micrometers and a thermal treatment zone of less than 0.5 mm.

Preliminary studies in earlier chapters have demonstrated that subsurface thermal denaturation of tissues can be achieved using a deeply penetrating laser wavelength (λ =

1064 or 1075 nm) in conjunction with surface cooling, preserving 1-2 mm of tissue surface (in porcine liver and skin both ex vivo and in vivo) from thermal necrosis [2-4,82,83]. Thus, laser denaturation and shrinkage of the endopelvic fascia may potentially produce improved tissue remodeling results similar to the RF approach, but in a less invasive manner with preservation of the vaginal mucosa.

Computer simulations utilizing optical, thermal, and damage parameters for vaginal wall, endopelvic fascia, and urethral wall, were conducted in this chapter for a transvaginal endoscopic approach to minimally invasive laser treatment of female SUI, with and without an OCA. By combining contact cooling with OCA, it is possible to preserve entire 2.7-mm-thick vaginal wall from thermal insult. In addition, OCA use translated into use of lower laser power, which may provide a safer and less expensive procedure. glycerol used in these studies is not only biocompatible, but also OCA effects can be easily reversed with tissue returning to its original state after rehydration.

These simulations were based on several assumptions. First, it was assumed that experimental OCA results applied to porcine vaginal tissue will be similar to human vaginal tissue. Second, optical clearing was assumed to only produce a decrease in scattering coefficient, but not absorption coefficient or anisotropy factor. Other studies have reported that the decrease in reduced scattering coefficient is primarily due to an increase in the anisotropy factor (g) due to structural changes in average collagen fiber size and packing of collagen fibers, rather than an increase in the scattering coefficient [84]. We therefore simulated this alternative case as well. However, the results were very similar. Monte Carlo simulations predicted that 51% of energy is absorbed by vaginal wall, 48% is absorbed in endopelvic fascia target layer, and only 1% is deposited in urethral wall.

During thermal simulations, the peak temperature in the endopelvic fascia reached 79.5 °C. A laser incident power of 4.43 W was necessary to achieve a damage parameter of $\Omega = 0.3$. Third, thermal property and damage parameters used in Table 6.2 were compiled from different sources, introducing a small error in our simulation results. For example, 5 W with OCA produced a peak temperature of 78.1°C in the endopelvic fascia layer in simulations, slightly below the critical damage threshold of 80.4 °C provided in Table 6.2. However, the damage parameter was $\Omega = 1.4$, a value greater than $\Omega = 1$, which indicates irreversible thermal damage to the tissue. Finally, dynamic optical property values due to changes in temperature and pressure and changes in thermal properties due to tissue perfusion were not included in this model. Despite these limitations, the simulations demonstrate that use of an OCA may further improve treatment depth for thermal remodeling by approximately 0.5 mm. This should allow preservation of the entire (2.7-mm-thick) vaginal wall during subsurface laser targeting and thermal remodeling of the endopelvic fascia for minimally invasive treatment of female stress urinary incontinence.

CHAPTER 8: Cadaver study

8.1 Introduction.

After determining the optimal wavelength, 1075 nm, for laser operation from chapter 3, the computer simulations demonstrated that a transvaginal approach for SUI treatment would be ideal. In addition, the application of glycerol as an OCA further improves the treatment depth for thermal remodeling by approximately 0.5 mm. An even more representative model would further strengthen our laser treatment approach for SUI. Both cadaver studies and *in vivo* animal pig studies were considered. There are additional milestones to achieve in order to proceed with those studies.

For example, the geometry of the transvaginal probe must be modified to fit the porcine vaginal anatomy. Also, the anatomy of the treatment zone needs to be carefully examined to better understand *in vivo* laser application. Ideally the goal is to develop one contact cooling laser probe, that can apply for both pre-clinical and clinical studies.

With help from Carolinas Medical Center, a total of three human female cadavers were available for testing. Despite the lack of blood flow and limited confirmation methods to validate thermal remodeling, a cadaver study offers crucial information such as treatment zone location, tissue similarity and more realistic surgical challenges than a laboratory setup.

8.2 Materials & Methods: Probe Modification.

In chapter 3, the 1st generation contact cooling laser probe was designed and used mainly for an *ex vivo* table top study and it was not optimized for *in vivo* animal studies. To conduct a proper *in vivo* animal experiment, reducing the size of the 1st generation contact cooling probe is necessary. Optimizing the flow rate was critical in the design process; therefore, the inflow and outflow diameters were kept unchanged. A careful balance was examined to minimize the physical dimensions for the 2nd generation contact cooling laser probe, and at the same time maximize the footprint of the sapphire window for optimal contact cooling. Despite smaller dimensions in the 2nd generation contact laser probe, to maintain similar coolant reservoir, the circulating well was designed to be 2 mm deeper than the previous generation of laser probe (Figure 8.1).

A 6.25 mm right angle prism was used to replace the custom-made rod lens from the 1st generation laser probe. This substitution of the rod lens with a standard, but smaller right angle prism slightly reduced power output due to an aperture mismatch (Figure 8.2 and Figure 8.3). Only 4% of laser was lost in the new design, which is not likely to affect the overall performance of the 2nd generation contact cooling laser probe. Meanwhile the surface of the 2nd generation laser probe cooled down to -4 °C, 2 °C colder than the 1st generation contact cooling laser probe.

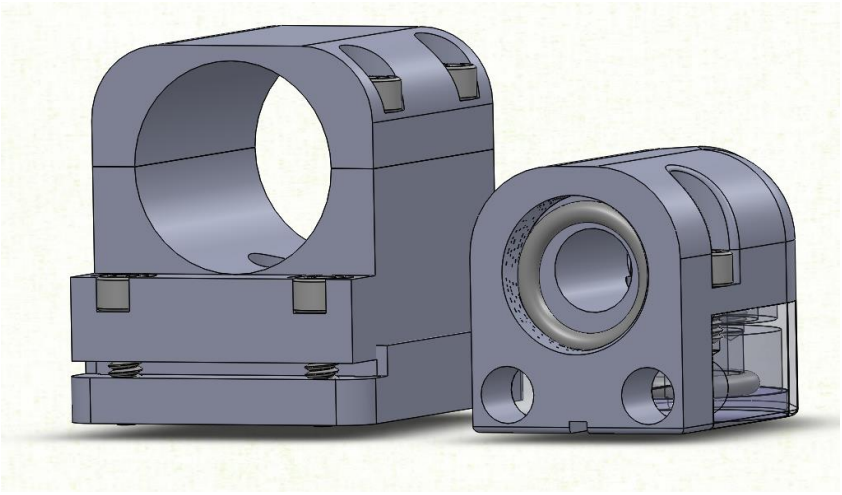

Figure 8.1**.** Diagrams of 1st generation laser probe side by side comparison with 2nd generation laser probe.

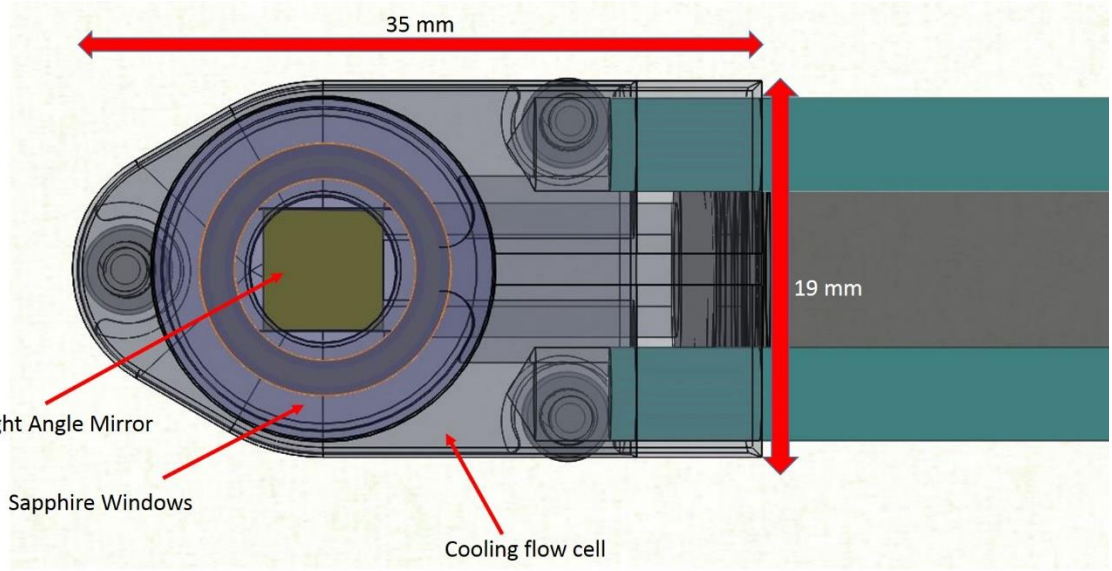

Figure 8.2**.** 2nd generation contact cooling laser probe (bottom view)

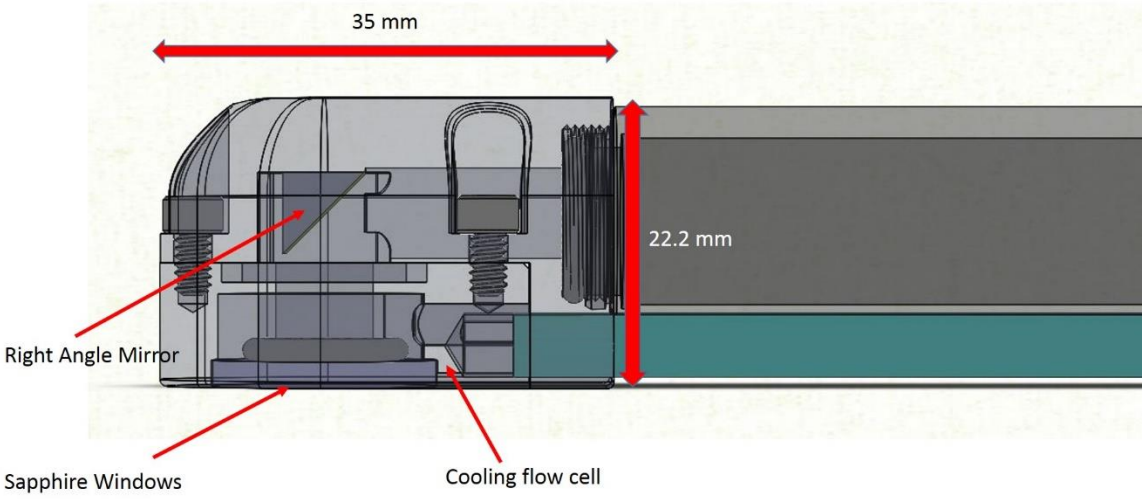

Figure 8.3. 2nd generation contact cooling laser probe (sideview)

To ensure constant contact with the vaginal tissue, a force sensor was added to the 2nd generation contact cooling laser probe (Figure 8.4). The circuit was custom built. The first 3 red LED's light up at 0.29, 0.59, and 0.88 newton, while the second 2 green LED's light up at 1.18, and 1.77 newton, respectively. The 2 blue LED's light up when 2.45 and 2.94 newton are applied, (Figure 8.5). The LED and force is programmable via USB using Atmel Studio software. This force sensor may help the surgeon to apply consistent force to the tissue and decrease variation between different treatments. Additionally, thermal data can be collected by attaching a micro-thermocouple (125-µm-OD) on the side of the laser probe (Figure 8.5).

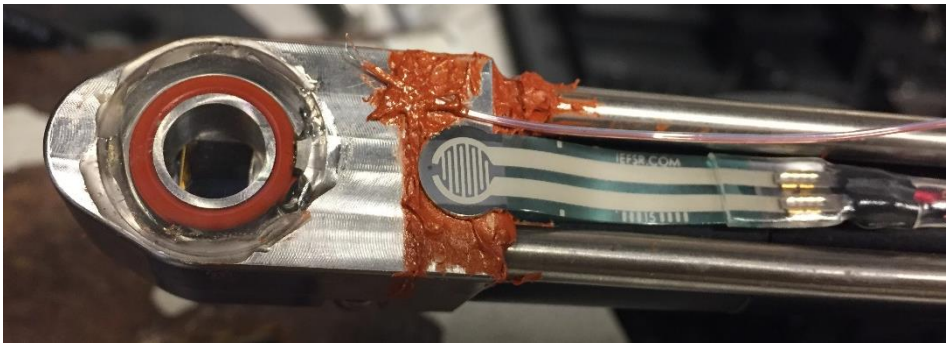

Figure 8.4**.** 2nd generation contact cooling laser probe with force sensor and micro-thermocouple attached.

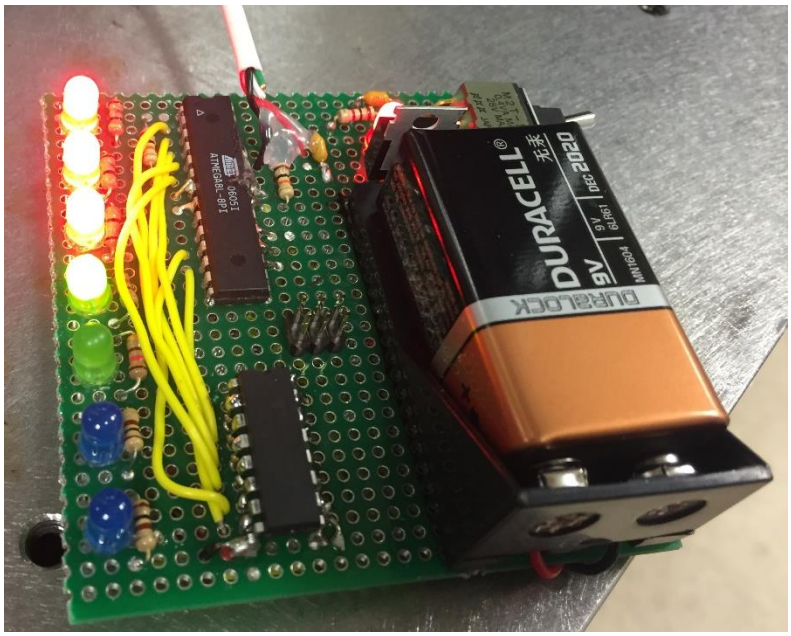

Figure 8.5**.** Force sensor circuit modules with LED indicator.

8.3 Cadaver Study.

8.3.1 Cadaver Methods.

Three cadaver studies were conducted to better understand the anatomical position of the treatment area and to test the ergonomics of the transvaginal laser probe. In the first cadaver study, an experienced gynecologist at Carolinas Medical Center, performed ultrasound scans to locate the treatment zone. The target location of endopelvic fascia through both transvaginal and transurethral approaches was the main goal of the study, to determine the ideal treatment zone location via ultrasound. The silicone balloon catheter had a distinct signature under ultrasound. An ultrasound machine (Flex Focus 400) was used to capture tissue position. An anorectal 3D 2052 Probe was deployed for cadaver 1, using a frequency of 13 MHz, to scan transvaginally with ultrasound transmission gel to ensure full contact between the tissue and probe (Figure 8.6).

In the second cadaver study, a few objectives were achieved. The initial test was to examine the depth of the laser treatment region. The optimal position was at 12 o'clock when the cadaver was in supine position and ~ 3 cm deep from the vaginal opening. The second test involved the effect of an optical clearing agent on cadaver tissue. Although the cadaver was at room temperature (19.4 °C) and not body temperature (37 °C), the OCA should still have a significant effect on the vaginal tissue.

Both non-invasive and invasive procedures were carried out in the third cadaver study. The 2nd generation probe was tested and the spectrum study from the second cadaver was repeated (n=4) for data confirmation purposes. In addition, a 1300 nm OCT system was employed to collect data in parallel with the reflection spectroscopy. The OCT data

were recorded every 5 minutes during the optical clearing experiments (n=4). Finally, the vaginal tissue was excised, and the 2nd generation probe was used to deliver the laser energy.

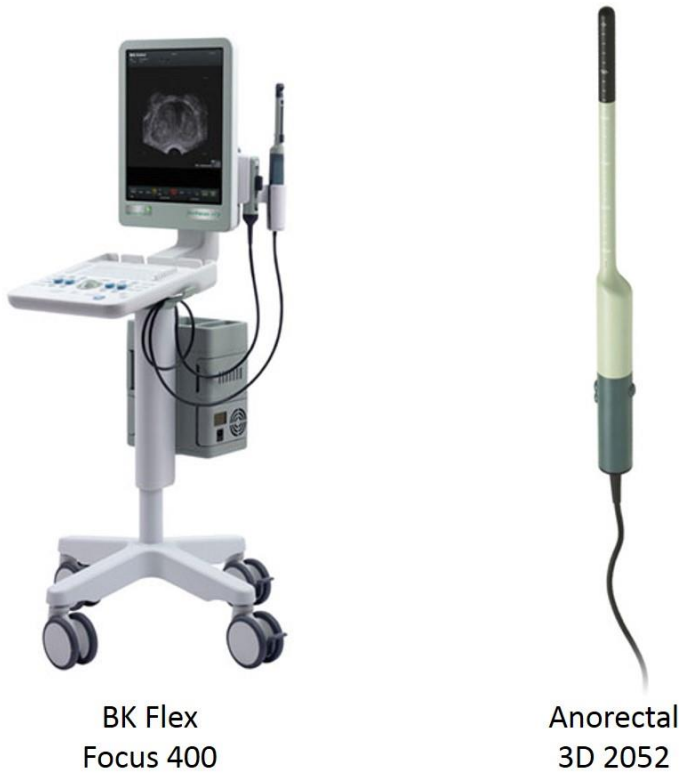

Figure 8.6**.** Ultrasound machine (Flex Focus 400) with Anorectal 3D probe.

8.3.1.1 Reflection Spectroscopy

A spectrometer (USB 4000-VIS-NIR, Ocean Optics, Dunedin, FL) was used to quantify change in the reflection spectrum of porcine vaginal wall as a function of OCA application time. A fiber optic Y cable (RP21, Thorlabs, Newton, NJ) was used to connect both the light source (MI-150, Edmund Optics, Barrington NJ), and the spectrometer (USB 4000-VIS-NIR, Ocean Optics, Dunedin, FL). The fiber tip was in direct contact with the sample and reflectance data was collected using proprietary software (Spectra Suite, Ocean

Optics). By comparing the baseline spectrum from native tissue at 0 min with the spectrum from optically cleared tissue, percentage change in reflection spectrum due to OCA was calculated and collected every 30 seconds over a total period of 30 minutes.

8.3.1.2 Optical Coherence Tomography

Optical coherence tomography (OCT) of vaginal tissue both with and without OCA was also performed with a clinical OCT system (Niris, Imalux, Cleveland, OH) using a handheld 8 Fr probe (2.67-mm-OD). The OCT system was a time-domain system based on a common-path all fiber interferometer designed to operate at a wavelength of 1300 nm [77], and was capable of acquiring images with 15 μm axial resolution and 25 μm lateral resolution. OCT images of vaginal tissue before and after application of glycerol were acquired to determine increased image depth based on decreased tissue scattering. Measurements were performed using software (ImageJ, National Institutes of Health, Bethesda, MD) to analyze the 256-gray scale image.

8.3.1.3 Excised vaginal tissue preparation.

Human vaginal tissue was excised by an attending physician. The tissue was approximately 1.5 cm wide by 5 cm long. The cadaver tissue had been defrosted and stored in the surgical laboratory at room temperature (~ 20 °C) for 3 days. An OCA (glycerol) was applied to the distal end of the tissue for 30 minutes for the spectrum study (Figure 8.7 and 8.8) and then afterwards, tissue was rehydrated with saline for 15 minutes before the laser treatment study. The excised vaginal tissue exhibited non-uniform coloration from the distal end to the proximal end (Figure 8.9).

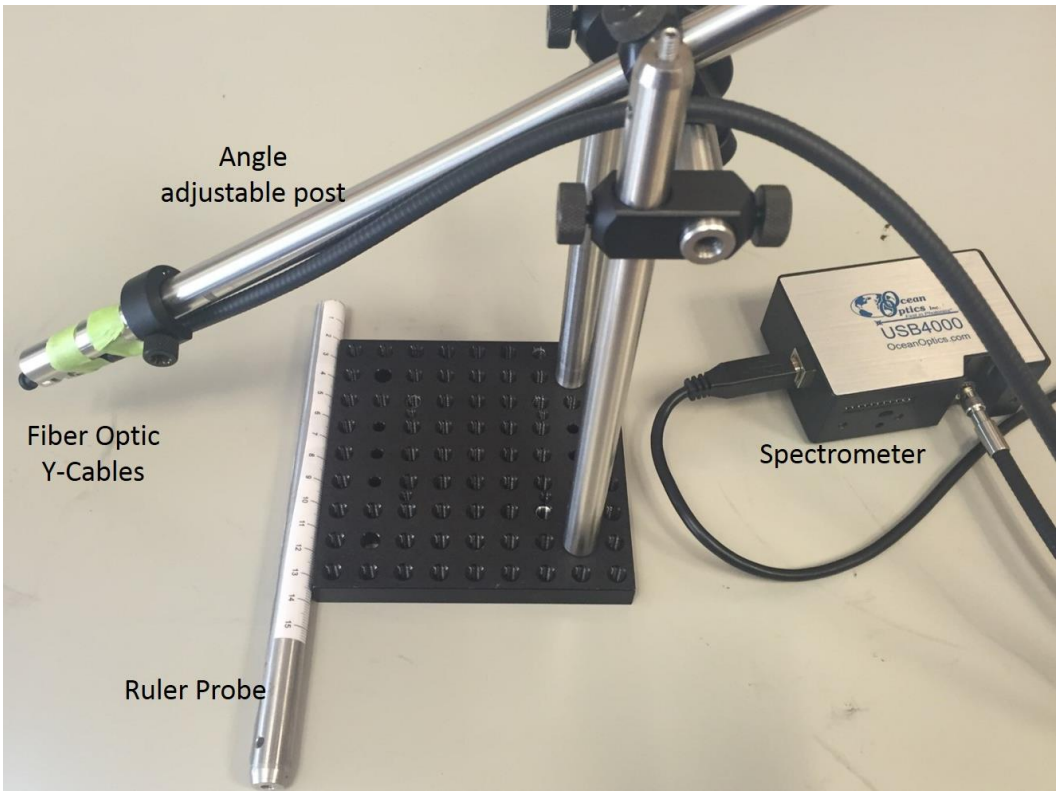

Figure 8.7. Spectrometer and Y-cables setup for cadaver data collection.

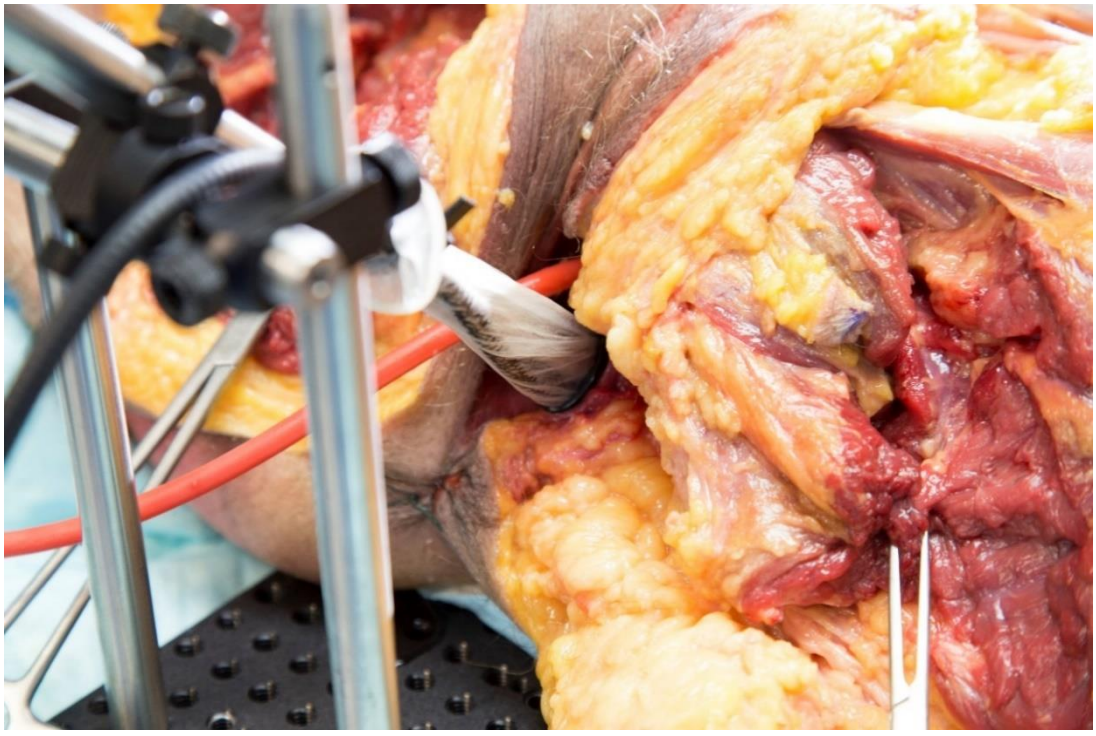

Figure 8.8. Setup for collecting reflectance spectrum response of glycerol, OCA, over a period of 30 minutes.

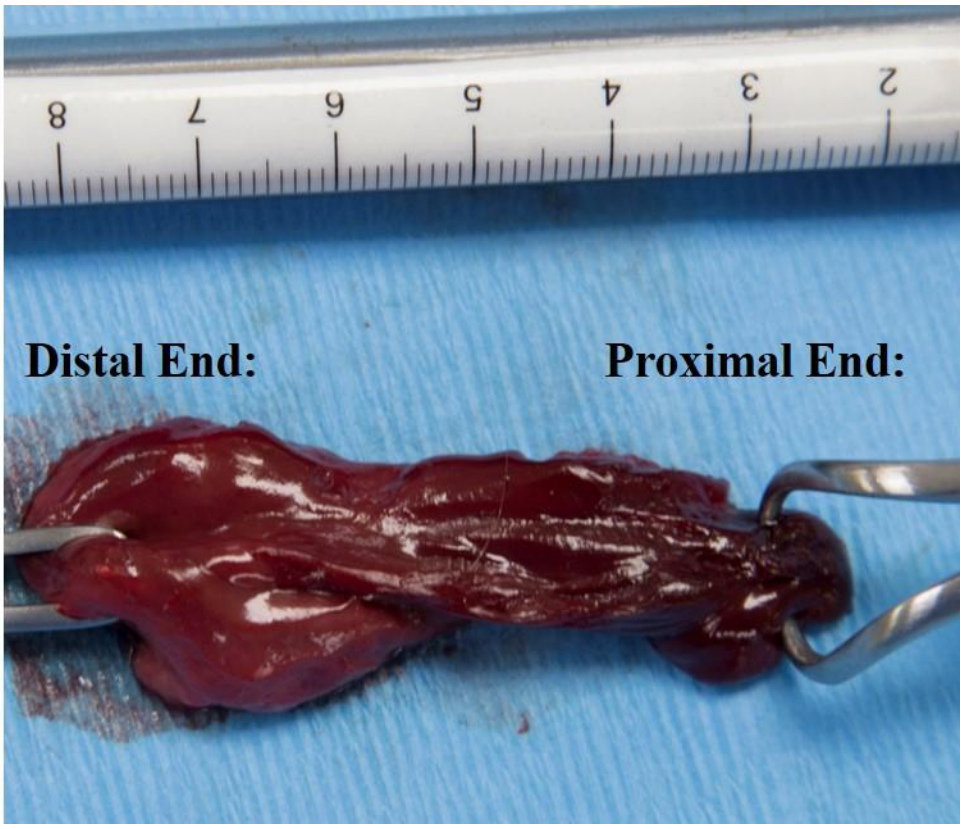

Figure 8.9. Excised vaginal tissue with an approximate dimension of 1.5 cm wide by 5 cm long.

8.3.2 Cadaver Results.

In the first cadaver study, ultrasound images were obtained to locate the ideal treatment zone area of the endopelvic fascia, labeled in Figure 8.10.

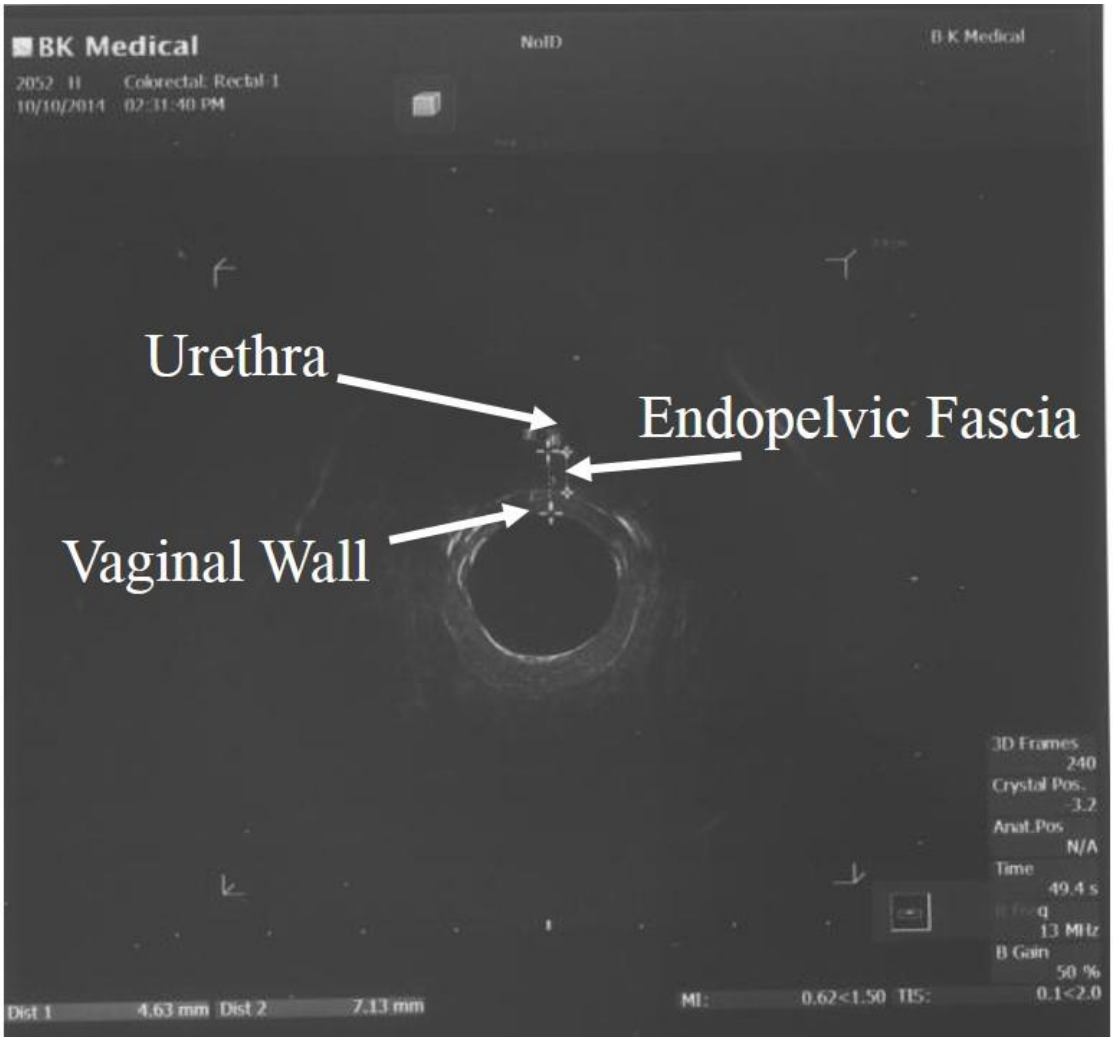

Figure 8.10**.** Cadaver's ultrasound image of vaginal canal collected from Flex Focus 400 with Anorectal 3D probe.

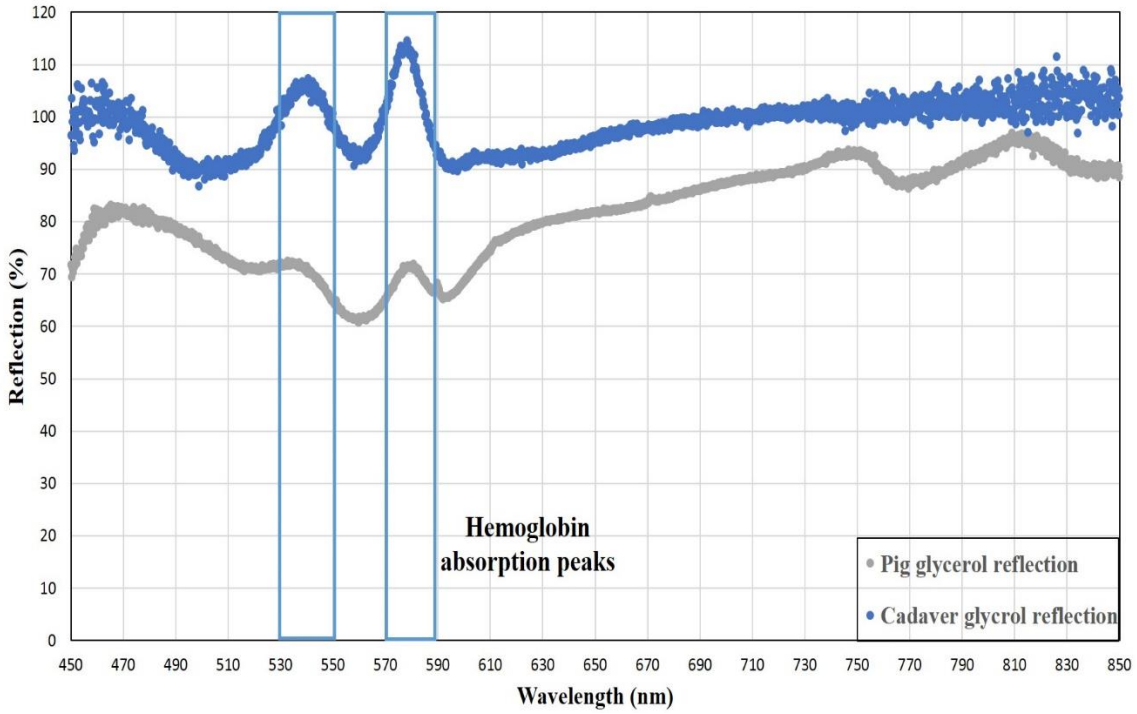

Figure 8.11**.** Spectrum response after applying glycerol, OCA, for a period of 30 minutes.

During the 2nd cadaver study, the vaginal tissue was treated with an optical clearing agent over for 30 minutes. The vaginal tissue was dehydrated and changed in spectrum response. As glycerol cleared out the vaginal wall making the tissue more transparent, it led to an increase in transmission which corresponded to the decrease in reflection (Figure 8.11).

Since the reference baseline was taken from the surface of the vaginal wall where hemoglobin was present, once the vaginal wall was cleared by glycerol through the reduction of scattering, the spectrometer effectively detected deeper into the tissue layer. If the tissue was dissected with a fixed thickness (similar to *ex-vivo* pig vaginal tissue in chapter 7), the reflection curve would be expected to decrease, similar to the response of pig glycerol OCA reflection curve in grey. The reflection curve matches with the

absorption of hemoglobin on vaginal wall (at 540 nm and 580 nm which are the absorption peaks of hemoglobin), which indicates the presence of blood in the endopelvic fascia layer.

In the third cadaver study, the force sensor on the 2nd generation probe was tested. The ideal contact force was found to be between 0.29 and 0.59 newton. The vaginal tissue was softer than expected, so re-programing may be necessary to further dial in the accuracy of the force sensor.

8.3.2.1 Reflection Spectroscopy

Reflection percentage change data was collected every 30 seconds in the wavelength range from 500 to 800 nm and compiled in 50 nm increments. The optical clearing experiment using glycerol was repeated 4 times. Glycerol tended to diffuse deeper into the tissue and the optical clearing affects diminished over time when the vaginal tissue was intact. In Figure 8.12 the U part of the blue curve shows that solution diffused into the surrounding tissue. It also indicates the optimal treatment time was about11 minutes with ~ 15% transmission change (assuming no change in absorption). On the other hand, when the vaginal tissue was excised, glycerol completely saturated the tissue and increased the transmission change to ~ 65 %. In Figure 8.12, excised vaginal tissue has a reflection spectrum that decays over time.

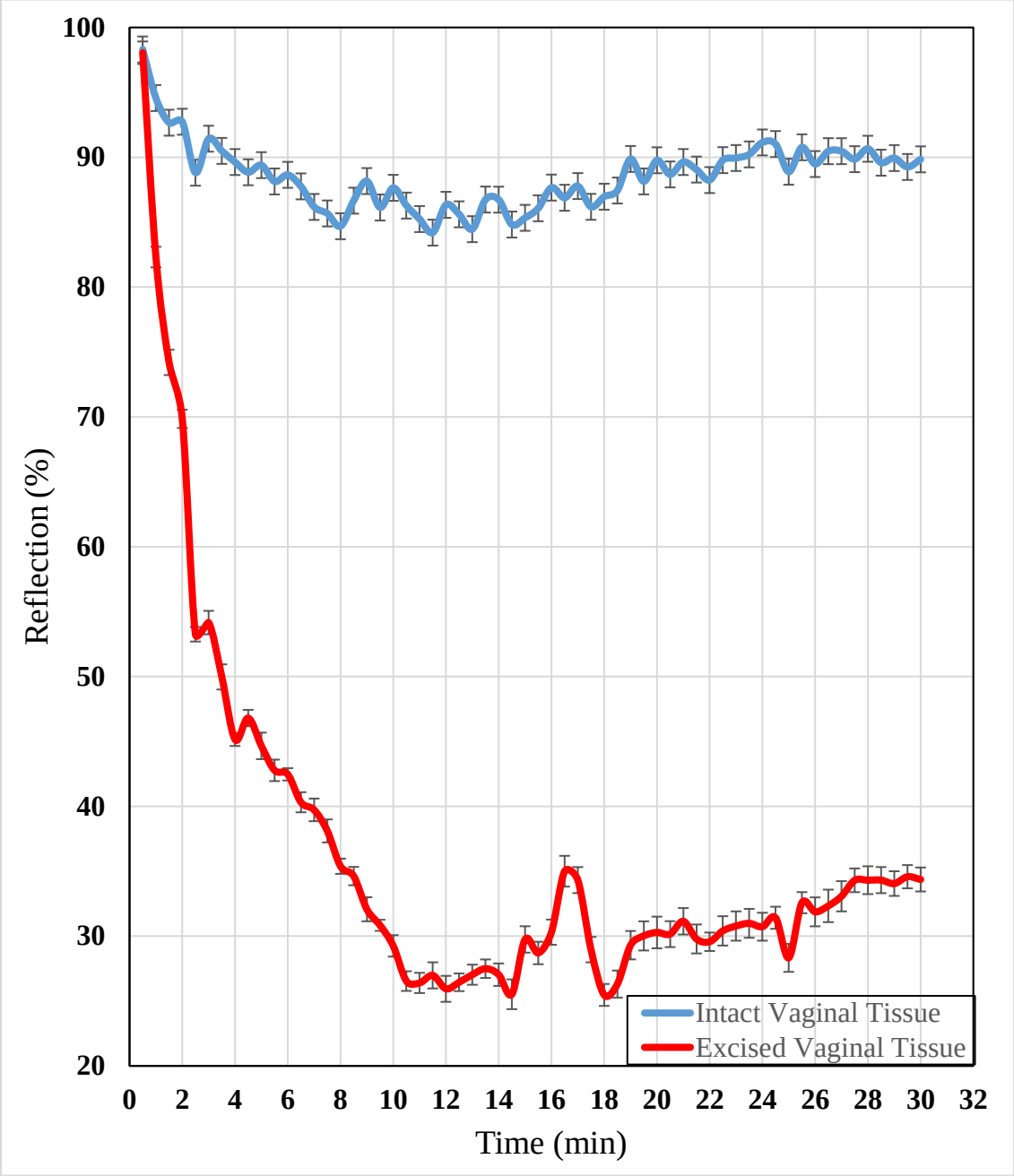

Figure 8.12. Average curve for reflection change from 500 to 800 nm over 30 minutes. Intact vaginal tissue has a U curve while excised vaginal tissue reflectance spectrum decays over time.

8.3.2.2 Optical Coherence Tomgraphy:

Since gray scale intensity is directly proportional to photon penetration depth, the 1/e intensity decrease is equal to a gray scale value of 94. Figure 8.13 (a) shows the initial OCT image (t=0 min). A 1/e intensity decrease was measured at a depth of 0.464 mm. For example, after OCA application (t=10 min) (Figure 8.13 (c)), the new 1/e, gray scale value of 94 increased to a depth 0.536 mm, which translates to a 15.5% increase in optical penetration depth with OCA.

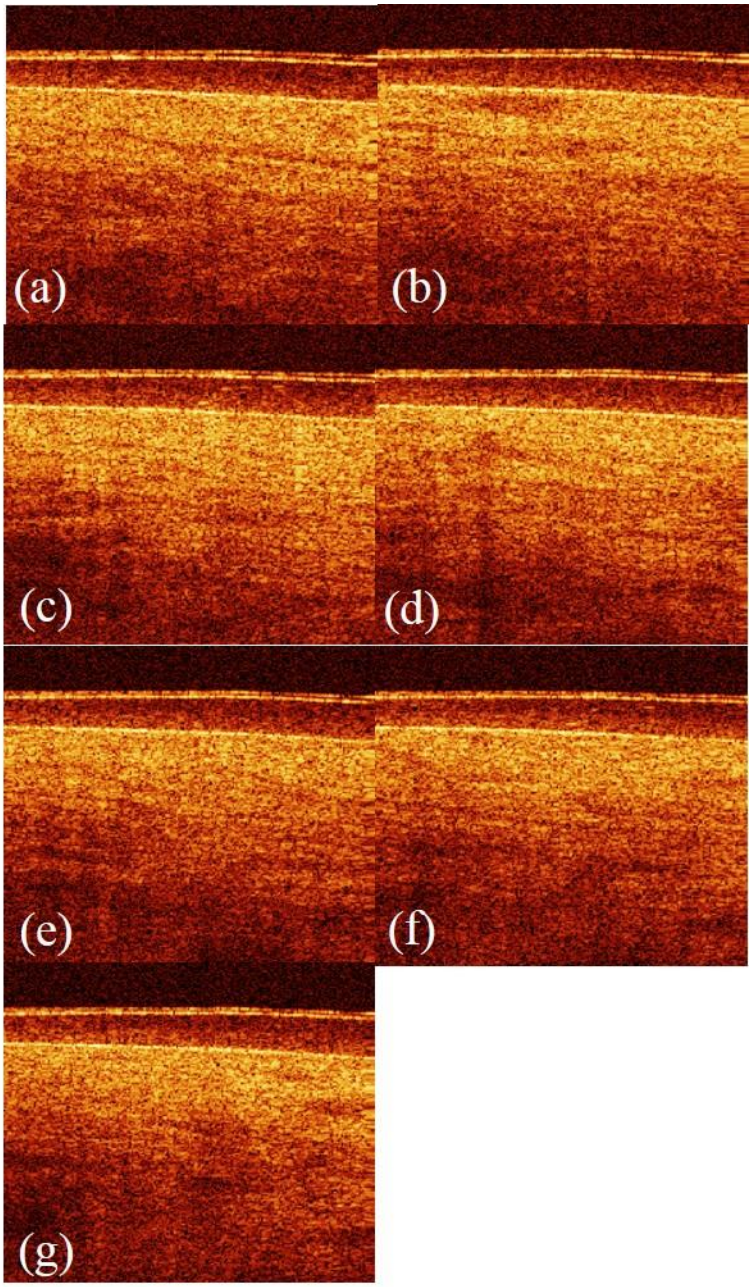

Figure 8.13**.** OCT progression a) t = 0 min, d = 0.464 mm b) t = 5 min, d = 0.496 mm. c) t = 10 min, d = 0.536 mm. d) t = 15 min, d = 0.528 mm. e) t = 20 min, d = 0.480 mm. f) t = 25 min, d = 0.472 mm. g) t = 30 min, d = 0.468 mm.

After the OCT transmission percentage change data is plotted over time via changing of gray scale, the affect of optical clearing at 1300 nm wavelength for intact

vaginal tissue demonstrates an optimal time of 10 minutes. This optimal treatment time at 10 minutes matches the optimal treatment time of 11 minutes from the reflection spectrum data above. Assuming no change in tissue absorption, the inverse of transmisson change displays the change in reflection. Figure 8.14 (b) exhibits a similar U curve as in Figure 8.12 despite the difference in wavelength range. Furthermore, OCT image data at 1300 nm wavelength for the intact vaginal tissue has a transmission change of ~ 16.9%, which is consistent with the spectrum transmission change at 11 minutes of ~ 15%.

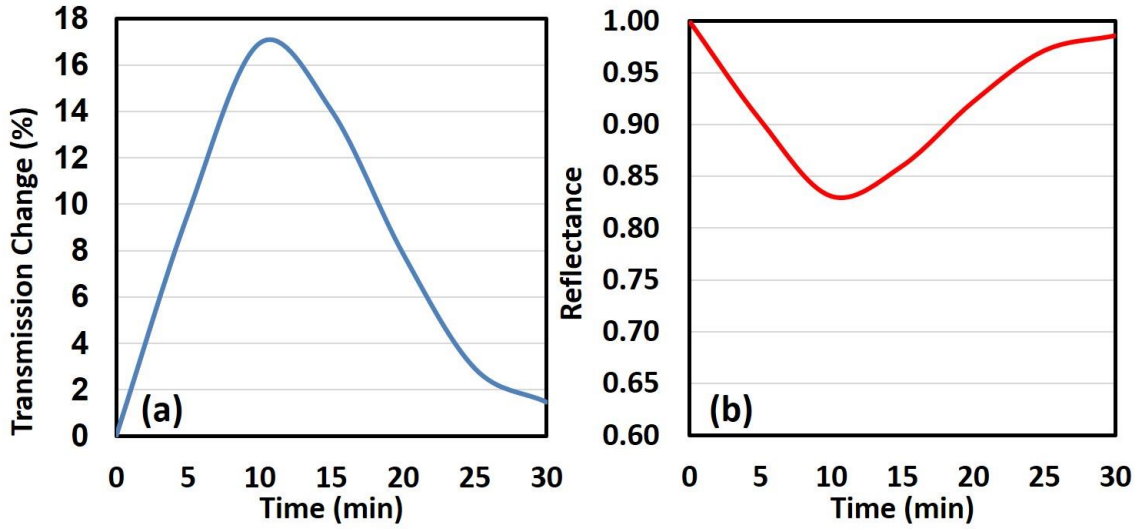

Figure 8.14**.** a) OCT gray scale progression of transmission change over time. b) If no change in absorption is assumed then reflection change is the inverse of transmission change.

8.3.2.3 Laser power escalation results:

Since the human cadaver tissue was non-uniform from distal to proximal end, a careful power escalation study was conducted at 30 seconds irradiation time, allowing a 5 minute pause in between studies. Subsurface lesions were made with 4.6 W and 6.4 W settings. It should be noted that the 4.6 W laser setting preserved a deeper surface tissue

layer than the 6.4 W setting (1.1 mm vs 0.77 mm) while also creating a larger lesion area (4.57 mm^2 vs 3.06 mm^2). This phenomenon can be attributed to the difference of the initial tissue temperature and the slight non-uniformity of the tissue composition from distal to proximal end.

Table 8.1 Lesion characteristics for laser power escalation test (λ = 1075 nm).

Parameters	**4.6 W**	**6.4 W**
Irradiation time (sec)	30	30
Tissue initial temperature (°C)	20	17
Contact cooling laser probe temperature (°C)	-2	-2
Lesion Characteristics		
Preserved Surface Tissue Layer (mm):	1.1 ± 0.17	0.77 ± 0.09
Lesion Area (mm^2):	4.57 ± 0.55	3.06 ± 0.32
Lesion Shape	Circular	Elliptical

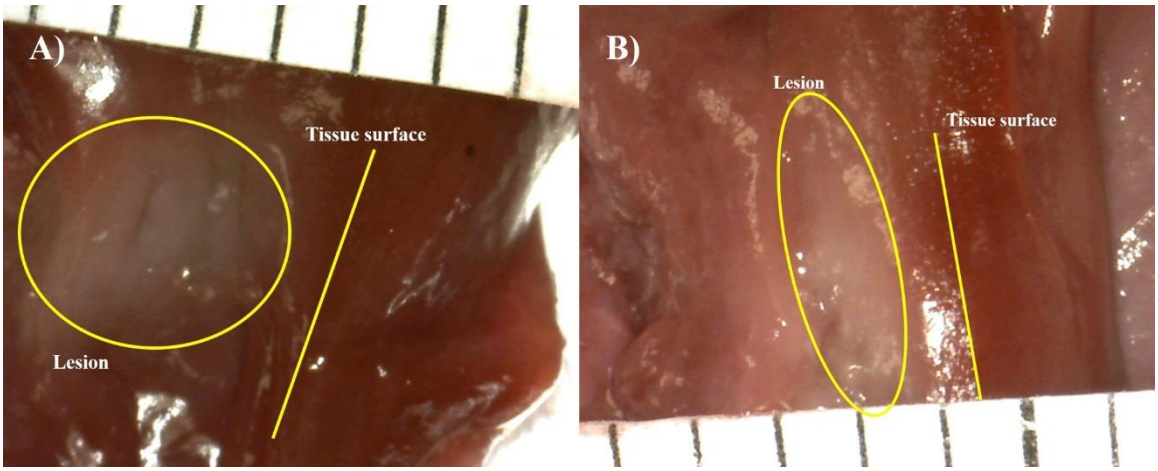

Figure 8.15. Representative gross images of thermal lesions produced in human vaginal tissue, ex vivo, using 1075 nm laser wavelength. a) 4.6 W for 30 s preserved 1.1 +/- 0.17 mm b) 6.4 W for 30 s preserved 0.77 +/- 0.09 mm.

.

8.3.3 Discussion

It was shown from chapter 7, at 22 °C porcine vaginal tissue with glycerol treatment for 10 minutes yielded a 16.4 % transmission change at 1075 nm (Figure 7.3). This data is in close agreement with the 1300 nm OCT gray scale analysis data of 16.9% transmission change at 10 minutes. The 1075 nm data from chapter 7 also agrees with the average spectrum result of 15 % at 11 minutes.

In chapter 7, at body temperature (37 °C), the OCA treated *ex-vivo* porcine vaginal tissue experienced ~1.98 times more transparency than room temperature (22 °C) OCA treated vaginal tissue over the same treatment period of 10 minutes. Assuming human vaginal tissue has a similar composition as pig vaginal tissue, a linear improvement in effectiveness of OCA is expected for human vaginal tissue at body temperature (37 °C). Therefore glycerol is expected to improve transmission to approximately 32.5% at body temperature over 10 minutes of application.

Subsurface lesions in human vaginal tissue indicated the feasibility of non-invasive laser treatment for SUI. However, more optimization is required to determine the exact laser parameters and cooling settings for thermal remodeling. An optical clearing agent can be used to temporary increase optical penetration depth for the laser treatment.

8.4 Conclusion

The 2nd generation contact cooling laser probe has a smaller form factor, is 2 °C colder than the 1st generation contact cooling laser probe, and has additional benefits of force sensor and thermal feedback. In the 1st cadaver study, we could identify the treatment

zone area; the 2nd cadaver study further confirmed the treatment zone at 12 o'clock and ~3 cm deep from the vaginal opening when the patient was in the supine position. An optical clearing agent was applied to cadaver vaginal tissue and demonstrated a similar behavior with porcine vaginal tissue. In the 3rd cadaver study, the 2nd generation contact cooling laser probe was tested, and the optimal contact force was determined to be 0.29 newton. Both reflection spectroscopy and OCT gray scale analysis indicate the optimal OCA treatment time to be 10- 11 minutes, providing a 15 - 17 % transmission improvement at room temperature with a predicted 32.5 % improvement at body temperature. Subsurface thermal lesions were made in human vaginal tissue, which preserved surface tissue from 0.77 to 1.1 mm, and demonstrated the feasibility of laser treatment for SUI.

CHAPTER 9: Conclusion

After confirming the laser spot size effect on optical penetration depth through simulations, a detailed wavelength comparison study was conducted, concluding that the near infrared wavelength of 1075 nm produced the deepest optical penetration depth in the therapeutic window, while preserving a surface layer of ~ 2 mm. From here on the dissertation focused on using the 1075 nm wavelength for most of the experiments.

To further understand how photons propagate in highly scattering tissue, Monte Carlo simulations were employed. After simulating the distribution of photons with known thermal properties from the published literature, the thermal effects of laser irradiation were studied. Finally, using a standard Arrhenius integral model, the tissue damage was simulated.

Several laser probe miniaturization studies were explored to find the optimal probe dimensions, and the capabilities of each laser probe were compared. The diffusing fiber produced subsurface thermal lesions measuring 49.3 ± 10.0 mm^2 and preserved 0.8 ± 0.1 mm of surface tissue. The side-firing fiber produced subsurface thermal lesions of 2.4 ± 0.9 mm^2 diameter and preserved 0.5 ± 0.1 mm of surface tissue. The cone mirror probe assembly failed to produce subsurface thermal lesions, presumably due to the small effective spot diameter at the tissue surface, which limited optical penetration depth. Optimal power and irradiation time measured 15 W and 100 s for diffusing fiber and 1.4 W and 20 s, for side-firing fiber, respectively. Diffusing and side-firing laser balloon

catheter designs provided subsurface thermal lesions in tissue. However, the divergent laser beam in both designs limited the ability to preserve a thicker layer of tissue surface.

The simulations in Chapter 4 were later modified to simulate the response of female urinary tissue under laser irradiation, for potential treatment of female stress urinary incontinence (SUI). For the transvaginal approach, 37% of energy was absorbed in endopelvic fascia layer with 0.8% deposited beyond it. Peak temperature was 71°C, and almost all of the 2.7-mm-thick vaginal wall was preserved. For the transurethral approach, 18% energy was absorbed in endopelvic fascia with 0.3% deposited beyond it. Peak temperature was 80°C, treatment zone was 2.0-mm-diameter, and only 0.6 mm of 2.4-mm-thick urethral wall was preserved. Computer simulations suggested that a transvaginal approach to thermal remodeling of endopelvic fascia is more feasible than a transurethral approach.

To achieve even deeper optical penetration depth, application of optical clearing agents were examined. Characterization studies were performed using various OCA mixtures, at different temperatures, and with additional OCT and spectroscopy for analyzing the experimental data and computer simulations of thermal damage to tissue. 100% glycerol was found to be the optimal agent. It produced a 61% increase in optical transmission through the vaginal wall at 37 °C after 30 min. Computer simulations, including Monte Carlo (MC) light transport, heat transfer, and Arrhenius integral model of thermal damage were performed. The MC model showed improved energy deposition in endopelvic fascia using glycerol. Without OCA, 62, 37, and 1% of energy was deposited in vaginal wall, endopelvic fascia, and urethral wall, respectively, compared with 50, 49,

and 1% using OCA. Use of OCA also resulted in 0.5 mm increase in treatment depth, allowing potential thermal tissue remodeling at a depth of 3 mm.

Finally, three human cadaver studies were performed. The treatment zone and laser probe dimensions for SUI treatment were investigated. The effectiveness of glycerol as an optical clearing agent was tested and the optimal treatment time was found to be 10 minutes. Subsurface lesions were made using 1075 nm laser and preserved surface tissue of 0.77 ± 0.09 mm and 1.1± 0.17 mm with 6.4 W and 4.6 W for 30 seconds. The results demonstrated the feasibility of laser treatment for SUI and a solid foundation for future pre-clinical and clinical studies.

References

[1] Berlien H, G. Muller. Applied Laser Medicine. Springer 2003.

[2] Ramli R, D. Durand, and N. M. Fried, "Subsurface tissue lesions using an Nd:YAG laser and cryogen cooling," J. Endourol. 17, 923-926 (2003).

[3] Ramli R, C. C. Chung, N. M. Fried, N. Franco, and M. H. Hayman, "Subsurface tissue lesions created using an Nd:YAG laser with a sapphire contact cooling probe," Lasers Surg. Med. 35, 392-396 (2004).

[4] Cilip C. M, J. P. Jarow, and N. M. Fried, "Noninvasive laser vasectomy: preliminary ex vivo tissue studies," Lasers Surg. Med. 41, 203-207 (2009).

[5] Jacques SL. Prahl, SA, Henyey-Greenstein scattering function. Oregon Graduate Institute. http://omlc.org/education/ece532/class3/hg.html.

[6] Niemz M. H. Laser-Tissue Interactions: Fundamentals and Applications. Springer 2003.

[7] Bashkatov N, E. Genina, V. I. Kochubey, and V. V. Tuchin, "Optical properties of human skin, subcutaneous and mucous tissues in the wavelength range from 400 to 2000 nm," J. Phys. D: Appl. Phys.38, 2543–2555 (2005).

[8] Ritz J, A. Roggan, G. Muller "Optical properties of native and coagulated porcine liver tissue between 400 and 2400 nm" Lasers Surg. Med. 29: 205-212 (2001)

[9] Keijzer M, S. L. Jacques, S. A. Prahl, and A. J. Welch, "Light distribution in artery tissue: Monte Carlo simulations for finite laser beams.," Lasers Surg. Med. vol. 9, pp. 148-154, 1989.

[10] Zhu D, Q. Luo, J. Cen. Effects of dehydration on the optical properties of in vitro porcine Lasers Surg. Med. 33:226-231 (2003).

[11] Stolik S, J. A. Delgado, A. Perez, and L. Anasagasti, "Measurement of the penetration depths of red and near infrared light in human ex vivo tissues," J. Photochem. Photobiol. 57, 90-93 (2000).

[12] Cheong W. F, S. A. Prahl, and A. J. Welch, "A review of the optical properties of biological tissues," IEEE J. Quantum Electron. 26, 2166-2185 (1990).

[13] Wang LH, SL. Jacques, LQ Zheng. MCML – Monte Carlo modeling of photon transport in multi-layered tissues. Comput. Methods Programs Biomed. 47:131-146, 1995.

[14] Wang LH, SL Jacques, LQ Zheng. CONV – Convolution for responses to a finite diameter photon beam incident on multi-layered tissues. Comput. Methods Programs Biomed. 54:141 150, 1997.

[15] Schweinsberger GR, CM Cilip, Trammell SR, Cherukuri H, Fried NM. Noninvasive laser coagulation of the human vas deferens: optical and thermal simulations. Lasers Surg. Med. 43:443-449, 2011.

[16] Muller G, A Roggan. Laser induced Interstitial Thermotherapy. SPIE Optical Engineering Press.1995.

[17] Welch A, JC. Martin J, V Gemert Optical-Thermal Response of Laser-Irradiated Tissue. P. 536. Plenum Press 2011.

[18] Ritz J, A Roggan, C.T, Germer, C Isbert, G Muller, H Buhr. Continuous changes in the optical properties of liver tissue during laser-induced interstitial thermotherapy Laser in Surg. Med. 28:307-312 (2001).

[19] Grossman C, Zhu T, Finlay J, Dimofte A, Malloy K. Weinstein Jr, G, Busch T. M, and Quon H, "Targeted laryngeal photodynamic therapy with balloon diffusing light source," Photodiagn. Photodyn. Therapy (2010) 7, 158-161 (2010).

[20] HeisterKamp J, Hillegersberg R. V, Sinofsky E, and IJzermans J. N, "Heat-resistant cylindrical diffuser for interstitial laser coagulation: comparison with the bare-tip fiber in a porcine liver model," Lasers Surg. Med. 20, 304-309 (1997).

[21] Knappe V, Roggan A, Glotz M, Muller M, Ritz G. P, Germer C. T, and Muller G, "New flexible applicators for laser-induced thermotherapy" Med. Laser Appl. 16, 73-80 (2001).

[22] Kosoglu M. A, Hood R. L, Rossmeisl J. H, Grant D. C, Xu Y, Roberson J. L, Rylander M. N, and Rylander C. G, "Fiberoptic microneedles: novel optical diffuser for interstitial delivery of therapeutic light" Lasers Surg. Med. 43, 914-920 (2011).

[23] Kang H. W, Kim J, and Oh J, "Enhanced photocoagulation with catheter-based diffusing optical device" J. Biomed. Opt. 17(11), 118001 (2012).

[24] Fanelli R. D, Gersin K. S, and Bakhsh A, "The Stretta procedure: effective endoluminal therapy for GERD," Surg. Technol. Int. 11, 129-134 (2003).

[25] Lightner DJ, NM Itano. Treatment options for women with stress urinary incontinence. Mayo Clin. Proc. 74:1149-1156, 1999.

[26] Pesce F. Current management of stress urinary incontinence. BJU Int. 2004; 94:8-13.

[27] Bent AE, MT McLennan. Surgical management of urinary incontinence. Obstet Gynecol. Clin. North Am. 25:883, 1998.

[28] Sotomayor M, GF Bernal. Transurethral delivery of radiofrequency energy for tissue micro-remodeling in treatment of stress urinary incontinence. Int Urogynecol J 14:373-379, 2003.

[29] Ross JW, DI Galen, K Abbott, D Albala, J Presthus, C Su-Ou, T Turk. A prospective multisite study of radiofrequency bipolar energy for treatment of genuine stress incontinence. J Am Assoc Gynecol Laparosc 9(4):493-499, 2002.

[30] Dmochowski RR, RA Appell. Advancements in minimally invasive treatments for female stress urinary incontinence: RF and bulking agents. Curr Urol Rep 4(5):350-355, 2003.

[31] Dmochowski RR, M Avon, J Ross, JM Cooper, R Kaplan, B Love, N Kohli, D Albala, B Shingleton. Transvaginal radio frequency treatment of the endopelvic fascia: a prospective evaluation for the treatment of genuine stress urinary incontinence. J Urol 169, 1028-1032, 2003.

[32] Sotomayor M, GF Bernal. Twelve-month results of nonsurgical radiofrequency energy micro-remodeling for stress incontinence. Int Urogynecol J 16(3):192-196, 2005.

[33] Lenihan JP. Comparison of the quality of life after nonsurgical radiofrequency energy tissue micro-remodeling in premenopausal and postmenopausal women with moderate-to-severe stress urinary incontinence. Am J Obstet Gynecol 192:1995-2001, 2005.

[34] Appell RA, S Juma, WG Wells, JP Lenihan, IW Klimberg, A Kanellos, SF Reilley. Transurethral radiofrequency energy collagen micro-demodelling for the treatment of female stress urinary incontinence. Neurourol Urodyn 25(4):331-336, 2006.

[35] Edelstein P.S, "A preclinical study of nonsurgical radiofrequency collagen remodelling for the treatment of stress urinary incontinence." Expert Rev Med Devices 3(6):743-748, 2006.

[36] Buchsbaum GM, J McConville, R Korni, EE Duecy. Outcome of transvaginal radiofrequency treatment of women with stress urinary incontinence. Int Urogynecol J Pelvic Floor Dysfunct 18(3):263-265, 2007.

[37] Appell RA, GW Davila. Treatment options for patients with suboptimal response to surgery for stress urinary incontinence. Curr Med Res Opin 23(2):285-292, 2007.

[38] Appell RA, G Singh, IW Klimberg, C Graham, S Juma, WG Wells, A Kanellos, SF Reilley. Nonsurgical, radiofrequency collagen denaturation for stress urinary incontinence: retrospective 3-year evaluation. Expert Rev Med Devices 4(4):455-461, 2007.

[39] Vianello A, E Constantini, M Del Zingaro, M Porena. Mini-invasive techniques for the treatment of female stress urinary incontinence. Minerva Ginecol 59(6):557-569, 2007.

[40] Ismail SI. Radiofrequency remodelling of the endopelvic fascia is not an effective procedure for urodynamic stress incontinence in women. Int Urogynecol J Pelvic Floor Dyfunct 19(9):1205-1209, 2008.

[41] Appell RA. Transurethral collagen denaturation for women with stress urinary incontinence. Curr Urol Rep 9(5):373-379, 2008.

[42] Elser DM, GK Mitchell, JR Miklos, KG Nickell, K Cline, H Winkler, WG Wells. Nonsurgical transurethral collagen denaturation for stress urinary incontinence in women: 12-month results from a prospective long-term study. J Minim Invasive Gynecol 16(1):56-62, 2009.

[43] Dillon B, R Dmochowski. Radiofrequency for the treatment of stress urinary incontinence in women. Curr Urol Rep 10(5):369-74, 2009.

[44] Davila GW. Nonsurgical outpatient therapies for the management of female stress urinary incontinence: long-term effectiveness and durability. Adv Urol 2011:176498.

[45] Wall MS, SH Deng, PA Torzilli, SB Doty, SJ O'Brien, R Warren. Thermal modification of collagen. J. Shoulder Elbow Surg 4:339-244, 1999.

[46] Effron JE, JL Corman, J Fleshman, J Barnett, D Nagle, E Birnbaum, EG Weiss, JJ Nogueras, S Sligh, J Rabine, SD Wexner. Safety and effectiveness of temperature

[47] Lustgarten DL, Spector PS. Ablation using irrigated radiofrequency: a hands-on guide. Heart Rhythm 2008; 5:899-902.

[48] Brace CL. Radiofrequency and microwave ablation of the liver, lung, kidney, and bone: what are the differences? Curr Probl Diagn Radiol 2009; 38:135-143.

[49] Nelson J. S, Majaron B, and Kelly K. M, "Active skin cooling in conjunction with laser dermatologic surgery," Semin. Cutan. Med. Surg. 19(4), 253-266 (2000).

[50] Zenzie H. H, Altschuler G. B, Smirnov M. Z, and Anderson R. R, "Evaluation of cooling methods for laser dermatology," Lasers Surg. Med. 26(2), 130-144 (2000).

[51] Salvatori S, Nappi RE, Zerbinati N, Calligaro A, Ferrero S, Origoni M, Candiani M, Leone Roberti Maggiori U. A 12-week treatment with fractional CO2 laser for vulvovaginal atrophy: a pilot study. Climacteric 2014; 17:363-369.

[52] Salvatore S, Leone Roberti Maggiore U, Athanasiou S, Origoni M, Candiani M, Calligaro A, Zerbinati N. Histological study on the effects of microablative fractional CO2 laser on atrophic vaginal tissue: an ex vivo study. Menopause 2015; 22:845-849.

[53] Zerbinati N, Serati M, Origoni M, Candiani M, Iannitti T, Salvatore S, Marotta F, and Calligaro A, "Microscopic and ultrastructural modifications of postmenopausal atrophic vaginal mucosa after fractional carbon dioxide laser treatment," Lasers Med. Sci. 30(1), 429-436 (2015).

[54] Singh N. Development and anatomy: disorders and development. In Brown L, ed. Pathology of the vulva and vagina. London: Springer-Verlag. 2013:1-11.

[55] Panayi D.C, A. Digesu, P. Tekkis, R. Ferando, V. Khullar. Ultrasound measurement of vaginal wall thickness: a novel and reliable technique. International Urogynecological Association (2010) 21:1265-1270.

[56] Wieczorek A.P, M.M. Wozniak, e.t. al. 3-D high-frequency endovaginal ultrasound of female urethral complex and assessment of inter-observer reliability. European Journal of Radiology 81 (2012) e7-e12.

[57] Huilan A, D. Xing, H. Wei, H. Gu, J. Lu. Thermal coagulation-induced changes of the optical properties of normal and adenomatous human colon tissue in vitro in the spectral range 400-1100nm. Phys. Med. Biol. 53 2008.

[58] Tsai C.L, J.C Chen, WJ. Wang. Near-infrared absorption property of biological soft tissue constituents. Journal of Medical and Biological Engineering, 21(1): 7-14 2001.

[59] McIntosh R.L, V. Anderson. Comprehensive tissue properties database provided for the thermal assessment of a human at rest. Biophysical Reviews and Letters 09/2010:5(3):129-151.

[60] Roggan A, Dorschel K, Minet D, Wolff D, Muller G. The optical properties of biological tissue in the near infrared wavelength range – review and measurements. In Muller G, Roggan A, eds. Laser-induced interstitial thermotherapy. Bellingham, WA: SPIE Optical Engineering Press. 1995:10-44.

[61] Barton JK. Dynamic changes in optical properties. In Welch AJ, van Gemert MJC, eds. Optical-thermal response of laser-irradiated tissue, 2nd ed. Heidelberg: Springer. 2011:321-349.

[62] Chan EK, Sorg B, Protsenko D, O'Neil M, Motamedi M, Welch AJ. Effects of compression on soft tissue optical properties. IEEE J Sel Top Quantum Electron 1996; 2:943-950.

[63] Niemz MH. Interaction Mechanisms. In Niemz MH, ed. Laser-tissue interactions: fundamentals and applications, 3rd ed. Heidelberg: Springer. 2004:45-150.

[64] Zhu D, Larin K.V, Luo Q, and Tuchin V.V, "Recent progress in tissue optical clearing," Laser Photonics Rev. 7, 732-757 (2013).

[65] Tuchina D, Shi R, Bashkatov A. N, Genia E. A, Zhu D, Luo Q, and Tuchin V.V, "Ex vivo optical measurements of glucose diffusion kinetics in native and diabetic mouse skin," J. Biophoton. 8, 332-346 (2015).

[66] Khan M. H, Choi B, Chess S, Kelly K. M, McCullough J, and Nelson J. S, "Optical clearing of in vivo human skin: implications for light-based diagnostic imaging and therapeutics," Lasers Surg. Med. 34, 83-85 (2004).

[67] Zhu Z, Wu G, Wei H, Yang H, He Y, Xie S, Zhao Q, and Guo X, "Investigation of the permeability and optical clearing ability of different analytes in human normal and cancerous breast tissues by spectral domain OCT," J. Biophoton. 5, 536-543 (2012).

[68] Zhao Q, Wei H, He Y, Ren Q, and Zhou C, "Evaluation of ultrasound and glucose synergy effect on the optical clearing and light penetration for human colon tissue using SD-OCT," J. Biophoton. 7, 938-947 (2014).

[69] Zhao Q. Li L, Li Q, Jiang X, Ren Q, Chai X, and Zhou C, "Concentration dependence of optical clearing on the enhancement of laser scanning optical-resolution photoacoustic microscopy imaging," J. Biomed. Opt. 19, 036019 (2014).

[70] Genina E. A, Bashkatov A. N, Kolesnikova E. A, Basko M.V, Terentyuk G.S. and Tuchin V. V, "Optical coherence tomography monitoring of enhanced skin optical clearing in rat in vivo," J. Biomed. Opt. 19, 021109 (2014).

[71] Cilip C. M, A. E Ross, J. P Jarow, N.M. Fried. Application of an optical clearing agent during noninvasive laser coagulation of the canine vas deferens. Journal of Biomedical Optics 15 (4), 048001 2010.

[72] Rylander CG, OF Stumpp, TE Milner, NJ Kemp, JM Mendenhall, KR Diller, AJ Welch. Dehydration mechanism of optical clearing in tissue. Journal of Biomedical Optics 11 (4), 04117 2006.

[73] Deng Z, Liu C, Tao W, and Zhu D, "Improvement of skin optical clearing efficacy by topical treatment of glycerol at different temperatures," J. Phys., 277, 012007 (2011).

[74] Xu X. and Wang R. K, "Synergistic effect of hyperosmotic agents of dimethyl sulfoxide and glycerol on optical clearing of gastric tissue studied with near infrared spectroscopy," Phys. Med. Biol. 49, 457-468 (2004).

[75] Jiang J and Wang R. K, "Comparing the synergistic effects of oleic acid and dimethyl sulfoxide as vehicles for optical clearing of skin tissue in vitro," Phys. Med. Biol. 49, 5283-5294 (2004).

[76] Bui A. K, McClure R. A, Chang J, Stoianovici C, Hirshburg J, Yeh A.T, and Choi B "Revisiting optical clearing with Dimethyl Sulfoxide (DMSO)" Lasers Surg. Med. 41, 142-148 (2009).

[77] Fried N. M, Rais-Bahrami S, Lagoda G. A, Chuang Y, Burnett A. L, and Su L. M, "Imaging the cavernous nerves in the rat prostate using optical coherence tomography," Lasers Surg. Med. 39, 36-41 (2007).

[78] Tuchin V. V, "Tissue and blood optical immersion by exogenous chemical agents," in *Optical clearing of tissue and blood*, SPIE Press, Bellingham, WA, 9-18 (2006).

[79] Jacques S L, "Monte Carlo modeling of light transport in tissues (steady state and time of flight)," In A. J. Welch and M. J. C. van Gemert, eds. Optical-thermal response of laser-irradiated tissue, 2nd ed. Heidelberg: Springer, 109-144 (2011).

[80] Vizintin Z, Lukac M, Kazic M, and Tettamanti M, "Erbium laser in gynecology," Climacteric 18 (suppl 1), 4-8 (2015).

[81] Ogrinc U. B, Sencar S, and Lenasi H, "Novel minimally invasive laser treatment of urinary incontinence in women," Lasers Surg. Med. 2015; 47, 689-697 (2015).

[82] Chung C. C, Varkarakis I. M, Permpongkosol S, Lima G, Franco N, Hayman M. H, T. L. Nicol, and N. M. Fried, "Laser probes for noninvasive coagulation of subsurface tissues," Proc. SPIE 607822, 1-5 (2006).

[83] Chang C. H, Wilson C. R, and Fried N. M, "Comparison of four lasers (λ = 650, 808, 980, and 1075 nm) for noninvasive creation of deep subsurface lesions in tissue. Proc. SPIE 9542, 95420G:1-4 (2015).

[84] Samatham, R., Phillips, K. G., Jacques, S. L., "Assessment of optical clearing agents using reflectance-modeconfocal scanning laser microscopy," Journal of Innovative Optical Health Sciences 3(3), 183-188 (2010).

[85] Takacs P and Nguyen A, "Mechanism of action of the Lyrette treatment for stress urinary incontinence," Verathon Medical, Lyrette, white paper (2013).

Appendix A: Simulation Comparisons

Optical Properties Represented wavelength (nm)	**650**	**808**	**980**	**1075**
Reference wavelength (nm)	650	830	980	1070
Absorption coefficient (μ_a) cm^-1	3	0.73	0.64	0.18
Scattering coefficient (μ_s) cm^-1	70	55	53.9	43.4
Anisotropy (g)	0.92	0.93	0.93	0.93
Refractive index (n)	1.38	1.38	1.38	1.38
Tested energy (J)	4.2	4.2	4.2	4.2
Reference	[1,16]	[16,18]	[16,18]	[16,18]

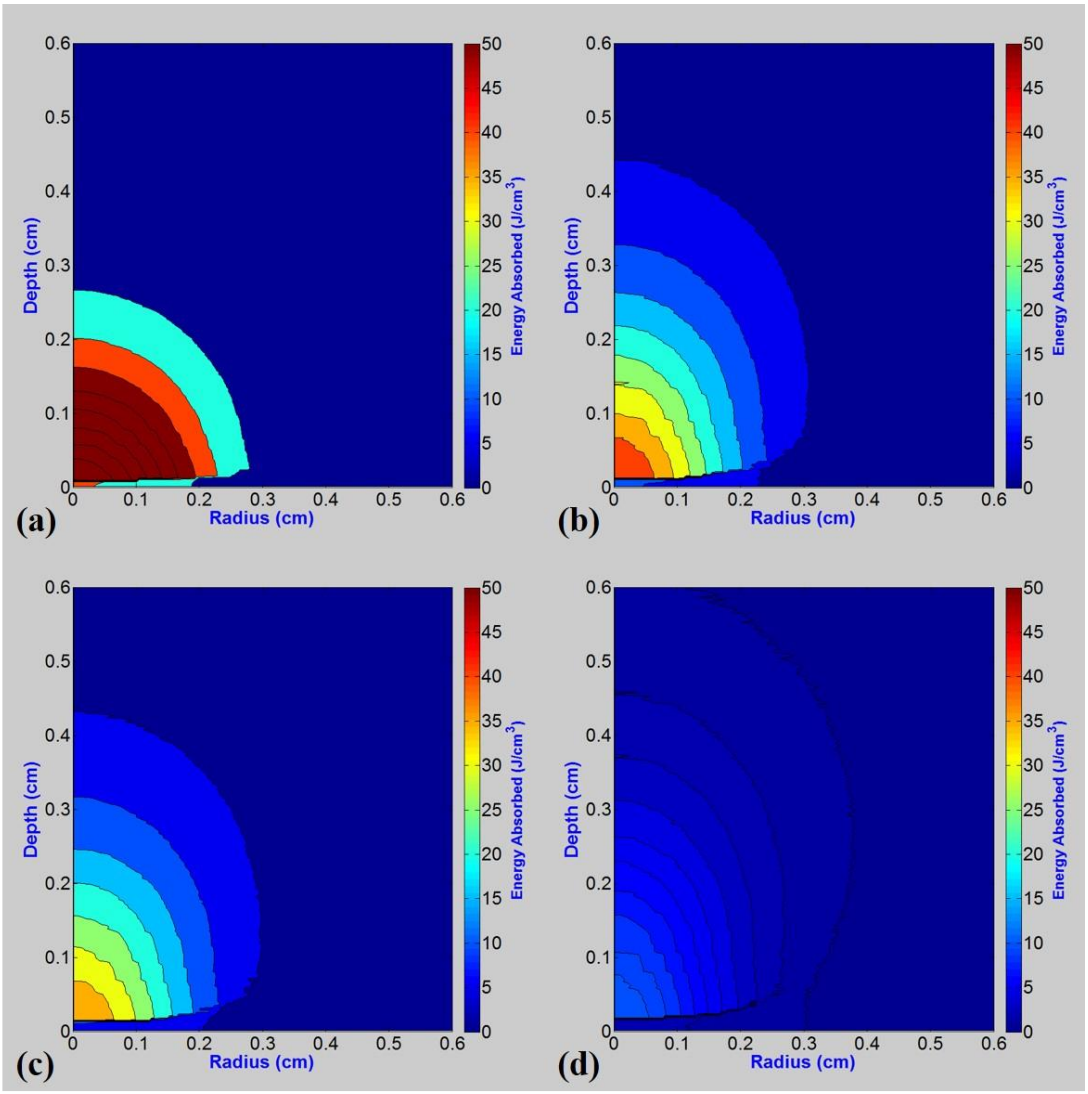

2D MC simulation of liver at 4.2W: a) 650 nm; (b) 808 nm; (c) 980 nm; (d) 1075 nm. For each laser, spot diameter was 5 mm.

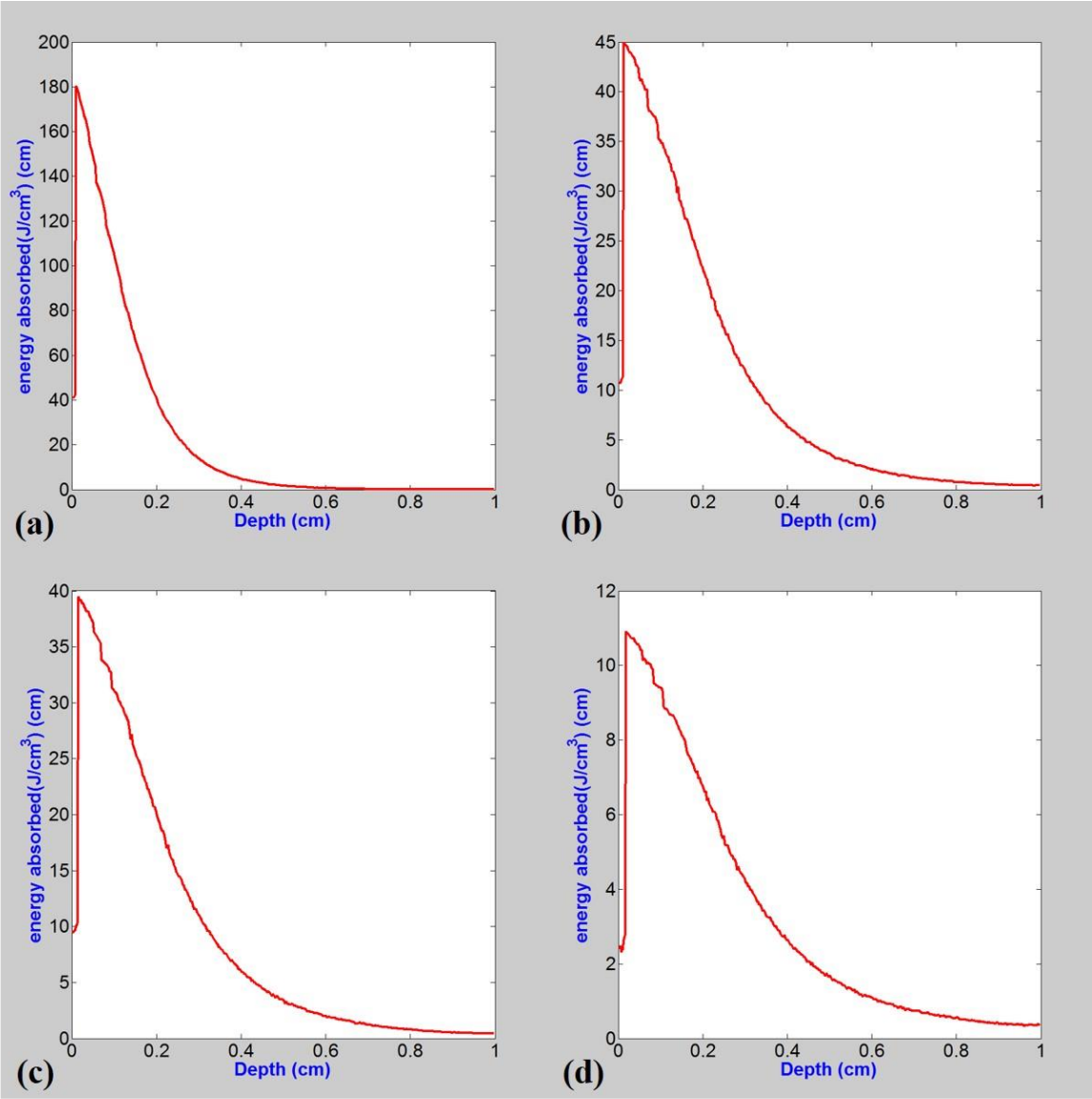

1D MC simulation of liver at 4.2W: a) 650 nm; (b) 808 nm; (c) 980 nm; (d) 1075 nm. For each laser, spot diameter was 5 mm.

Appendix B: Computer Code

Phase I: Monte Carlo Simulation

```
%Chapter 2 simulation (figure 2.5) & Chapter 4 simulation & Chapter 6
%Modified from 'graph_for_transvaginaltest4_all_three_graph' by Luke
Hardy
clear;
clf;
clc;
close all;
% place .arzc file here with 350*350 bins
M=dlmread('liver5mm7_2wd.arzc','',1,0);
X= reshape(M(1:122500),350,350);
XX= reshape(X(1,1:350),350,1);
XXX=reshape(XX(1:316,1),316,1);
negXX=flipud(XX*(-1));

newXX=[negXX; XX];

Y= reshape(M(1:122500,2),350,350);
YY= reshape(Y(1:350,1),350,1);

Z= reshape(M(1:122500,3),350,350);
Z2=fliplr(Z);
newZ=[Z2,Z];

figure(1);
contourf(newXX,YY,newZ);
axis([-0.6 .6 0 .6])
set(gca,'fontsize',26)
xlabel('Radius (cm)','FontSize',28,'FontWeight','bold','Color','b');
ylabel('Depth (cm)','FontSize',28,'FontWeight','bold','Color','b');
colorbar;

figure(2);
contourf(XX,YY,Z);
set(gca,'fontsize',24)
xlabel('Radius (cm)','FontSize',24,'FontWeight','bold','Color','b');
ylabel('Depth (cm)','FontSize',24,'FontWeight','bold','Color','b');
colorbar;

radius=input('how far along "r" for contour map?');
n=round(radius*1/(23/7000)+1);

ZZ=reshape (Z(1:350,n),350,1);

figure(3);
plot(YY,ZZ);
set(gca,'fontsize',24)
xlabel('Depth (cm)','FontSize',24,'FontWeight','bold','Color','b');
ylabel('Energy Absorbed
(J/cm^3)','FontSize',24,'FontWeight','bold','Color','b');
```

Phase II: Heat transfer simulation via ANSYS 14.5

Phase III: Calculating Arrhenius Integral for Thermal Damage

```
%Chapter 4 simulation_2 & Chapter 6
%Modified from 'nodetemps_Arrhenius_integral' by Luke Hardy
clear;
clf;
clc;
close all;
M=dlmread('1064.txt','',0,0); % input temperature file from ansys
nodes= reshape(M,123904,30); % rows are nodes, columns are time steps
Ctemp= nodes-273.15;
c=max(Ctemp)
b=max(c)
damage=zeros([1 123904]); % creates damage vector and populate it with
zero
R= 8.3146421; % gas constant
%{
Takes text file from ansys and delets all 'NODES, X,Y, and Z'
then converts the cells into doubles and puts them into one large
matrix
%}
fileID= fopen('C_NLIST1064T.txt'); %input list of nodes and
corresponding coordinates file from ansys
C=textscan(fileID, '%s %s %s %s');
G=C{2};
inds=~cellfun('isempty',strfind(G(:,1),'X'));
G(inds,:)=[];
G=str2double(G)*10^3;
F=C{3};
inds=~cellfun('isempty',strfind(F(:,1),'Y'));
F(inds,:)=[];
F=str2double(F)*10^3;
fclose(fileID);
N=horzcat(G,F);
DIGITS=10;
J= [N nodes];
J2= sortrows(J,[2 1]);
global n t
for n=1:1:123904; % node number going from 1 to 180
    for t=1:1:30; % time step going from 1 to 30
            A= 5.51*10^41;% updated from welch 2011 book for Arrhenius
integrals
            E= 2.769*10^5; % updated from welch 2011 book for Arrhenius
integrals
            damage(n)=damage(n)+ A*exp((-E/(R*J2(n,t+2)))); % calculate
damage integral for each node
    DIGITS=10;
    actual(n)=(1-(1/exp(damage(n))))*100; % percent of damaged tissue
    end
    end
damage2=damage.';
actual2=actual.'; % transpose of percent of damaged tissue vector

N2= sortrows(N,[2 1]);
O=horzcat(N2, actual2); %putting r,z, and damaged percent for columns
with rows being vector numbers
```

```
O2=horzcat(N2,damage2);%putting r,z, and omega for columns with rows
being vector numbers

P=sortrows(O,[2 1]); % sorts r column then z column to prepare for
plotting of the damage
P2=sortrows(O2,[2 1]);

r= reshape(P(1:123904,1),352,352);
r2= reshape(r(1:352,1),352,1); % r column vector
z= reshape(P(1:123904,2),352,352);
z2= reshape(z(1,1:352),1,352); % z column vector
con= reshape(P(1:123904,3),352,352).'; % percent tissue damage matrix
con2= reshape(P2(1:123904,3),352,352).'; % omega tissue damage matrix
figure(1);%percent tissue damage
contourf(r2,z2,con);
set(gca,'fontsize',18)
xlabel('Radius (mm)','FontSize',18,'FontWeight','bold','Color','b');
ylabel('Depth (mm)','FontSize',18,'FontWeight','bold','Color','b');
colorbar;
figure(2);%omega tissue damage
contourf(r2,z2,con2);
set(gca,'fontsize',18)
xlabel('Radius (mm)','FontSize',18,'FontWeight','bold','Color','b');
ylabel('Depth (mm)','FontSize',18,'FontWeight','bold','Color','b');
colorbar;

%Chapter 6 parts

for n=1:1:124256; % node number going from 1 to 180
    for t=1:1:45; % time step going from 1 to 30
        if n<=33440;
            A= 5.6*10^63;% Aorta frequency factor for Arrhenius
integrals
            E= 4.30*10^5; % Aorta Activation energy for Arrhenius
integrals
            damage(n)=damage(n)+ A*exp((-E/(R*J2(n,t+2)))); % calculate
damage integral for each node
        elseif 33440<n<86592
            A=1.606*10^45; % rat collegen
            E=3.06*10^5; % rat collegen
            damage(n)=damage(n)+ A*exp((-E/(R*J2(n,t+2)))); % calculate
damage integral for each node
        else
            A=8.4*10^78;
            E=4.98*10^5;
        damage(n)=damage(n)+ A*exp((-E/(R*J2(n,t+2)))); % calculate
damage integral for each node
        end
    end
    DIGITS=10;
    actual(n)=(1-(1/exp(damage(n))))*100; % percent of damaged tissue
end
```

Appendix C: Probe Design Drawings

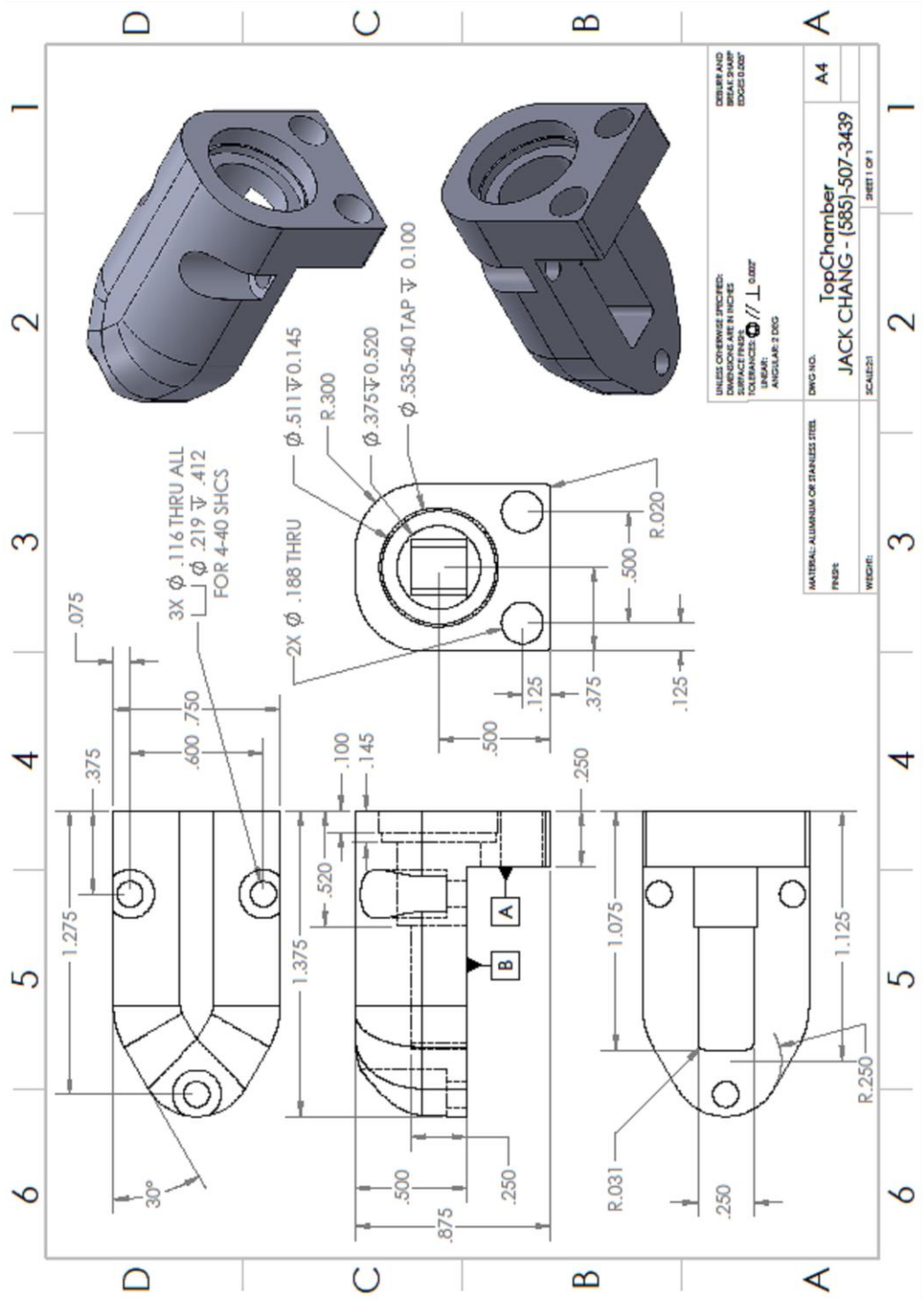

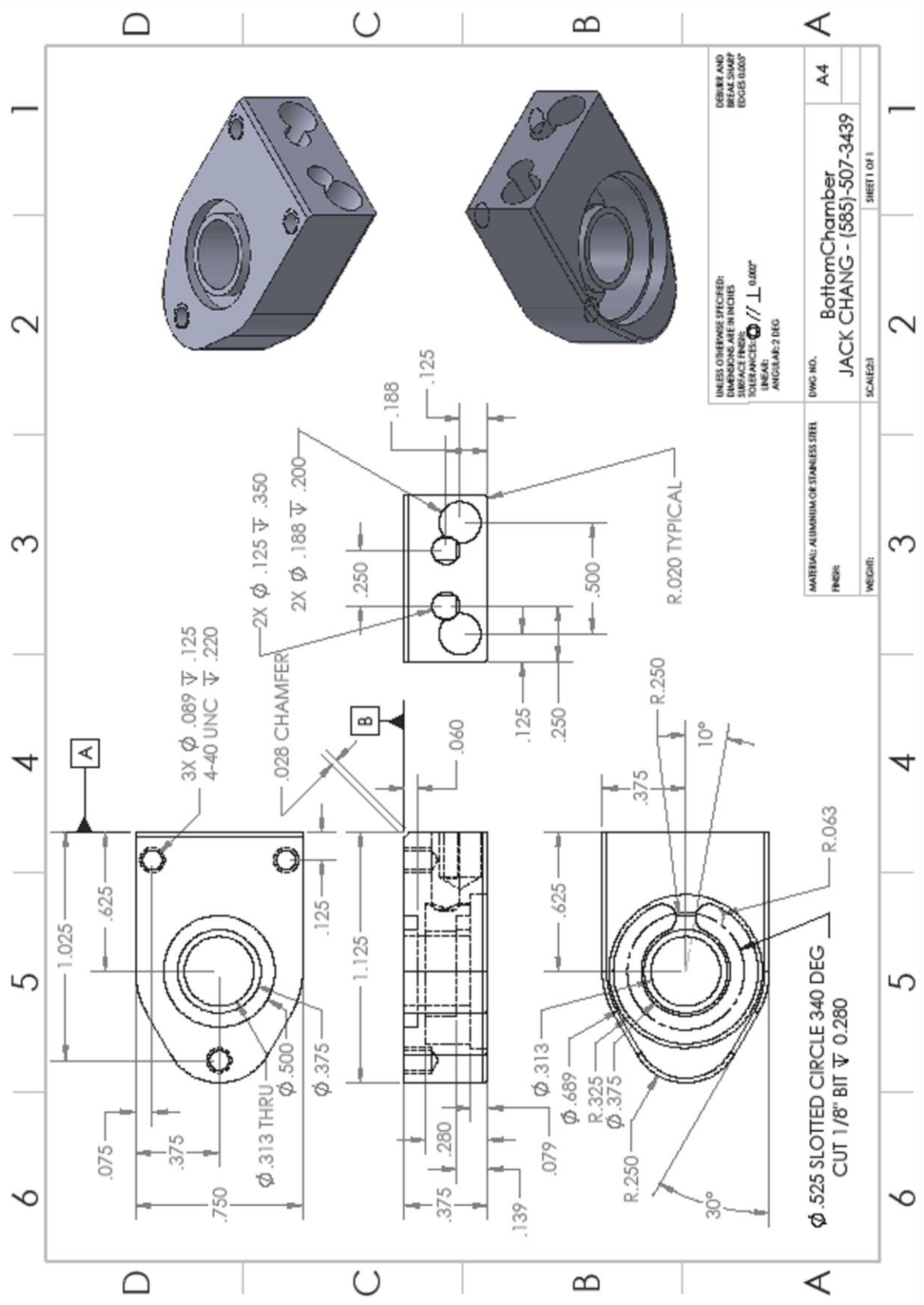
BottomChamber
JACK CHANG - (585)-507-3439
A4
MATERIAL: ALUMINUM OR STAINLESS STEEL
FINISH:
DWG NO.
WEIGHT:
SCALE:2:1
SHEET 1 OF 1
UNLESS OTHERWISE SPECIFIED:
DIMENSIONS ARE IN INCHES
SURFACE FINISH:
TOLERANCES:
LINEAR:
ANGULAR: 2 DEG
DEBURR AND BREAK SHARP EDGES 0.005"
3X Ø .089 ⧩ .125
4-40 UNC ⧩ .220
.028 CHAMFER
2X Ø .125 ⧩ .350
2X Ø .188 ⧩ .200
.188
.125
.250
.500
R.020 TYPICAL
.060
.125
.250
R.250
10°
.375
R.063
1.025
.625
.125
1.125
.075
.375
.750
Ø .313 THRU
Ø .500
Ø .375
.280
.375
.139
.079
Ø .313
Ø .689
R.325
Ø .375
R.250
30°
Ø .525 SLOTTED CIRCLE 340 DEG
CUT 1/8" BIT ⧩ 0.280

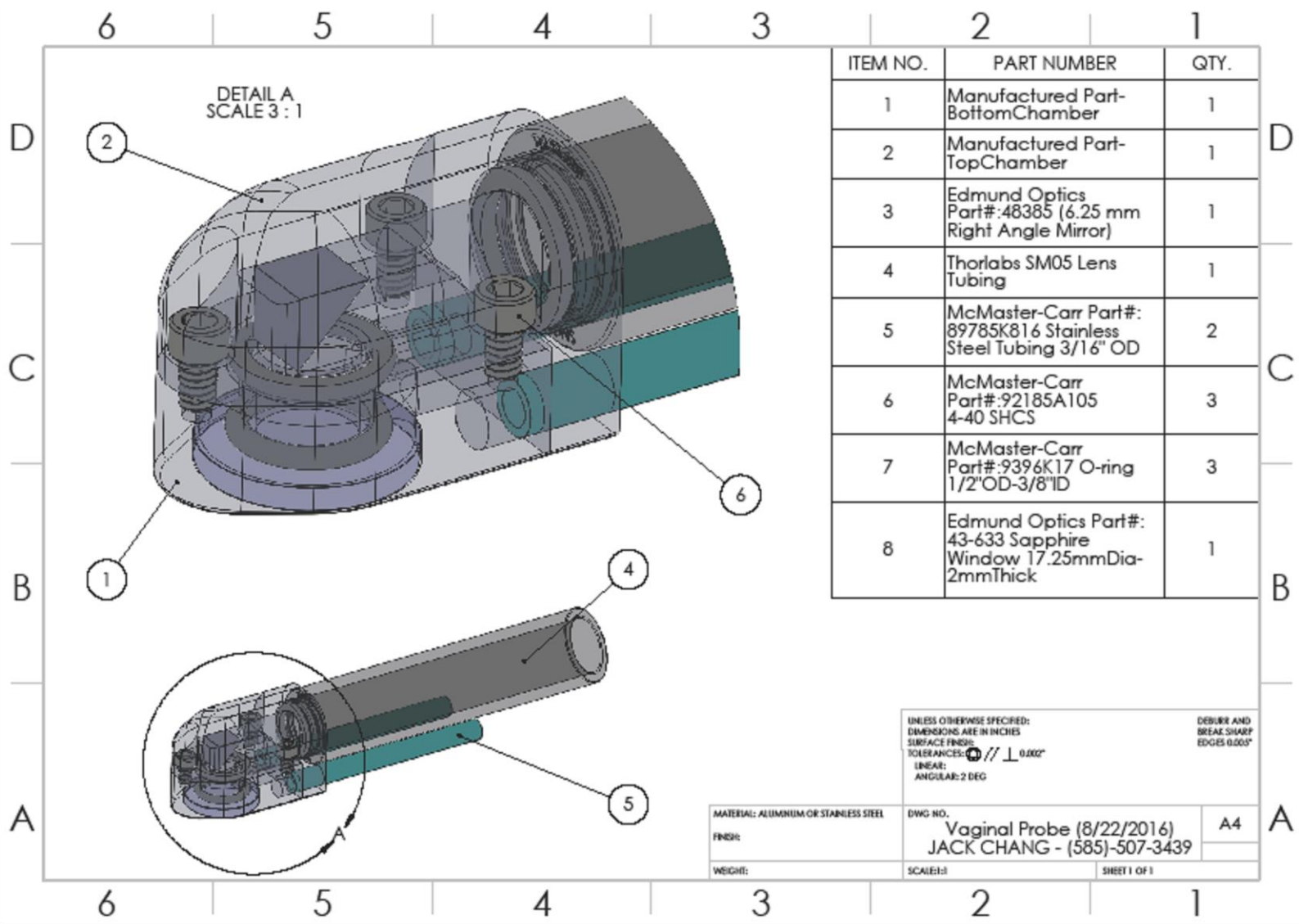

ITEM NO.	PART NUMBER	QTY.
1	Manufactured Part-BottomChamber	1
2	Manufactured Part-TopChamber	1
3	Edmund Optics Part#:48385 (6.25 mm Right Angle Mirror)	1
4	Thorlabs SM05 Lens Tubing	1
5	McMaster-Carr Part#: 89785K816 Stainless Steel Tubing 3/16" OD	2
6	McMaster-Carr Part#:92185A105 4-40 SHCS	3
7	McMaster-Carr Part#:9396K17 O-ring 1/2"OD-3/8"ID	3
8	Edmund Optics Part#: 43-633 Sapphire Window 17.25mmDia-2mmThick	1

UNLESS OTHERWISE SPECIFIED:
DIMENSIONS ARE IN INCHES
SURFACE FINISH:
TOLERANCES: ⌀ // ⊥ 0.002"
LINEAR:
ANGULAR: 2 DEG

DEBURR AND BREAK SHARP EDGES 0.005"

MATERIAL: ALUMINUM OR STAINLESS STEEL
FINISH:

DWG NO. Vaginal Probe (8/22/2016)
JACK CHANG - (585)-507-3439

A4

WEIGHT:
SCALE:1:1
SHEET 1 OF 1

Pressure sensor computer code:

```
/*
 * ForseSensor.c
 *
 * Created: 12/11/2016 11:58:15 AM
 *  Author: jbabaie & jchang
 */


#include <avr/io.h>
#include <avr/interrupt.h> // enable interrupts
#include <math.h> // enable interrupts
#define LED0_off PORTD &= 0b11111110; //PD0 to low
#define LED0_on PORTD |= 0b00000001; //PD0 to high
#define LED1_off PORTD &= 0b11111101; //PD1 to low
#define LED1_on PORTD |= 0b00000010; //PD1 to high
#define LED2_off PORTD &= 0b11111011; //PD2 to low
#define LED2_on PORTD |= 0b00000100; //PD2 to high
#define LED3_off PORTD &= 0b11110111; //PD3 to low
#define LED3_on PORTD |= 0b00001000; //PD3 to high
#define LED4_off PORTD &= 0b11101111; //PD4 to low
#define LED4_on PORTD |= 0b00010000; //PD4 to high
#define LED5_off PORTD &= 0b11011111; //PD5 to low
#define LED5_on PORTD |= 0b00100000; //PD5 to high
#define LED6_off PORTD &= 0b10111111; //PD6 to low
#define LED6_on PORTD |= 0b01000000; //PD6 to high

double voltage_in = 0; //between 0-1
double res_in = 0; //in 1000s(k)
double force_in = 0;


ISR(ADC_vect){
voltage_in = (double) ADCW/1024;
res_in = 10/voltage_in-10;
force_in = pow(res_in/143.94,-1.467);

ADCSRA |= 0b01000000; //start next conversion
}

int main(void)
{
   DDRD |= 0b01111111; //Set pin 0 in D register as output (PD0-6)
DDRC &= 0b11111110; //Set pin 0 in C register as input (PC0)
LED0_off LED1_off LED2_off LED3_off LED4_off LED5_off LED6_off
//ADC Initialization
ADMUX = 0b00000000; //76> set to AREF, 5>right adjusted 3-0> select ADC0 initially
ADCSRA = 0b10001010; //7> enable ADC, 6>do not start conversion, 5>do not trigger, 3>use
interrupt, 2-0> 4 division factor
ADCSRA |= 0b01000000; //start the first conversion
sei(); //enable interrupts
while(1)
   {
      if (force_in > 30) {LED0_on}
      else {LED0_off}
```

```
if (force_in > 60) LED1_on
       else LED1_off
if (force_in > 90) LED2_on
else LED2_off
if (force_in > 120) LED3_on
else LED3_off
if (force_in > 180) LED4_on
else LED4_off
if (force_in > 250) LED5_on
else LED5_off
if (force_in > 300) LED6_on
else LED6_off
   }
}
```

Appendix D: List of Publications

Chang, C.H. Wilson C.R. Fried, N.M. Comparison of four lasers (λ = 650, 808, 980 and 1075nm) for noninvasive creation of deep subsurface lesions in tissue. SPIE Proc. Vol 9542, 95420G (2015).

Chang, C.H, Hardy, L.A. Wilson C.R. Fried, N.M. Diffusing, side-firing, and radial delivery laser balloon catheters for creating subsurface thermal lesions in tissue. SPIE Proc. Vol 9689, 96891S (2016).

Hardy, L.A. Chang, C.H. Fried, N.M. Laser treatment of female stress urinary incontinence: optical, thermal, and tissue damage simulations. SPIE Proc. Vol 9689, 96891R (2016).

Hardy, L.A. Chang, C.H. Fried, N.M. Computer simulations of laser thermal remodeling during minimally invasive transvaginal and transurethral approaches to treatment of female stress urinary incontinence. Lasers Surg. Med 49:198-205 (2017)

Chang, C.H. Hammerland, D. Nau, W.H. Fried, N.M. Rapid and precise dissection of fascia layers, ex vivo, using continuous-wave, 1470nm diode laser and novel laparoscopic probe. SPIE Proc. Vol 10066, 100660V (2017).

Hardy, L.A. Larson E. Hutchens, T.C. Gonzalez D. Chang, C.H. Nau, W.H. Fried, N.M. Laparoscopic prototype for optical sealing of renal blood vessels. Proc. SPIE Vol 100380V-100380V-7 (2017).

Hardy, L.A. Larson E. Hutchens, T.C. Gonzalez D. Chang, C.H. Nau, W.H. Fried, N.M. Rapid sealing of porcine renal blood vessels, *ex vivo*, using a high power, 1470-nm diode laser and laparoscopic prototype. J. Biomed Opt. in press.

Chang, C.H. Myers E.M. Kennelly M.J. Fried, N.M. Optical clearing of vaginal tissues. Proc. SPIE Vol 10038, 100380A-1 (2017).

Chang, C.H. Myers E.M. Kennelly M.J. Fried, N.M. Optical clearing of vaginal tissues, ex vivo, for minimally invasive laser treatment of female stress urinary incontinence. J. Biomed Opt. 22 (1), 018002 (2017).